NASA TECHNICAL MEMORANDUM

NASA TM X-71975

COPY NO.

NASA TM X-71975

AN EXPERIMENTAL STUDY OF JET EXHAUST SIMULATION

BY WILLIAM B. COMPTON III

JUNE 1974

NATIONAL AERONAUTICS AND SPACE ADMINISTRATION

LANGLEY RESEARCH CENTER, HAMPTON, VIRGINIA 23665

1 Report No. NASA TM X-71975	2 Government Accession No	3 Recipient's Catalog No
4 Title and Subtitle An Experimental Study of Jet Exhaust Simulation		5 Report Date June 1974 6 Performing Organization Code
7. Author(s) William B. Compton, III		8. Performing Organization Report No
9 Performing Organization Name and Address NASA Langley Research Center Hampton, Va. 23665		10 Work Unit No 501-24-06-01 11 Contract or Grant No
12 Sponsoring Agency Name and Address National Aeronautics and Space Administration Washington, D.C. 20546		13 Type of Report and Period Covered Technical Memorandum 14 Sponsoring Agency Code

15 Supplementary Notes
Interm technical information release, subject to possible revision and/or later publication

16 Abstract

An investigation was conducted to determine the effect of varying the jet exhaust's ratio of specific heats, gas constants, and temperatures on jet interference on afterbody drag. Jet exhaust simulation parameters were evaluated also. Besides air, three other exhaust gases, each with a different value of each of the gas parameters, were tested.

The ratios of specific heats, gas constants, and total temperatures of the four gases ranged respectively from 1.40 to 1.26, 287 $\frac{\text{joules}}{\text{kg K}}$ to 376 $\frac{\text{joules}}{\text{kg K}}$, and 300 K to 1013 K. Tests were made using a single nacelle model with afterbodies having boattail angles of 10° and 20°, and having sonic and Mach 2 jet exits. The investigation was conducted in the Langley 16-foot transonic wind tunnel through a Mach number range of 0.60 to 1.20 at Reynolds numbers per meter from 10.06×10^6 to 14.05×10^6.

17 Key Words (Suggested by Author(s)) (STAR category underlined)
Fluid Mechanics
Jet Interference
Jet Simulation
Jet Exhaust
Jet Plume
Jet Effects
Entrainment

18 Distribution Statement
Unclassified - Unlimited

19 Security Classif (of this report)	20 Security Classif (of this page)	21 No of Pages	22 Price*
Unclassified	Unclassified	100	$4.00

*Available from { The National Technical Information Service, Springfield, Virginia 22151
STIF/NASA Scientific and Technical Information Facility, P O. Box 33, College Park, MD 20740

AN EXPERIMENTAL STUDY OF JET EXHAUST SIMULATION

By

William B. Compton III

SUMMARY

An investigation was conducted to determine the effect of varying the jet exhaust's ratio of specific heats, gas constants, and temperatures on jet interference on afterbody drag. Jet exhaust simulation parameters were evaluated also. Besides air, three other exhaust gases, each with a different value of each of the gas parameters, were tested. Tests were made using a single nacelle model with afterbodies having boattail angles of 10° and 20°, and having sonic and Mach 2 jet exits. The investigation was conducted in the Langley 16-foot transonic wind tunnel through a Mach number range of 0.60 to 1.20 at Reynolds numbers per meter from 10.06×10^6 to 14.05×10^6.

Differences between the jet interference of the four exhaust gases ranged from 10 to 20 percent of the jet off drag at the low jet pressure ratios, and up to 35 percent of the jet off drag at a jet exit pressure ratio of 3. Air, when used as the jet exhaust, consistently resulted in the highest drag. The actual magnitude of the increments between the jet interference of the various exhaust gases was greatest for the combination of high boattail angles and high subsonic and transonic Mach numbers. For operating conditions typical of high nozzle drag (high boattail angles, and transonic speeds and corresponding pressure ratios) the current data indicate that the use of air to simulate dry-turbojet exhaust can result in an increase of afterbody drag amounting to as much as 20% of the dry-turbojet value.

The differences in jet interference between the various exhaust gases are attributed to different plume shapes and entertainment properties of the gases. Corrections for the plume shape differences can be made by relating the drag to the computed plume angle. Although the entrainment differences are difficult to predict, they seem to be a relatively straight line function of the product of the jet exhaust gas constant and local temperature, and also of the local jet exhaust kinetic energy per unit mass.

INTRODUCTION

Experimence has shown that the complex flow field in the vicinity of an airplane's exhaust nozzles has made prediction of transonic nozzle drag difficult. (ref. 1 and 2). Therefore, experimental methods are usually used to obtain reliable transonic performance data.

Since the jet engine exhaust affects the afterbody drag because of plume blockage and aspiration due to the exhaust mixing with the external flow, propulsion tests are conducted in which the exhaust flow is simulated. Usually, because of technical reasons, costs, or safety considerations the fluid simulating the jet exhaust is not the same as the exhaust gases of the full scale airplane. Thus, the difference in the temperatures, specific heats, and gas constants between the model and airplane exhausts can result in the jet interference of the model and airplane being different.

Other investigations which have been conducted to determine the effect of varying the exhaust gas parameters on jet interference (ref. 3 to 8) generally utilized afterbody configurations which were not

---

*The information presented in this report is based on a thesis submitted in partial fulfillment of the requirements for the degree of Master of Science, George Washington University, Washington, D. C., August 1973.

typical of airplanes today. They also usually lacked information such as jet exit profiles, afterbody skin temperatures, and boundary layer profiles which precluded determining precise differences in drag due solely to the jet interference of the various exhaust gases. However, the investigations did tend to show that with cold air simulating the jet exhaust, base and boattail pressures were generally lower than for the other gases. In reference 9 attention was especially given to the problem of correlating the jet interference for different exhaust gases. In that reference, several jet simulation parameters were proposed which, if matched for different jet exhausts, would hopefully give the same jet interference for each exhaust gas.

The present investigation was conducted to get a clear understanding of the relative magnitude of jet interference for various exhaust gases. It also was conducted to determine at what conditions any differences between the jet interference of the various gases occur, the cause of the differences, and to evaluate the simulation parameters suggested in reference 9. Two afterbodies, one with a boattail angle of 20° and one with an angle of 10°, were investigated. Each was investigated for jet exit Mach numbers of 1 and 2. Air and the decomposition products of three concentrations of hydrogen peroxide were used for the jet exhaust. Afterbody pressures and skin temperatures, jet exit pressure and temperature profiles, and afterbody boundary layer profiles, were measured.

In this particular phase of the investigation, efforts were concentrated on studying the problem of jet interference on surafces forward of the nozzle exit. Therefore, in attempting to correlate the jet interference for the different exhaust gases, only those parameters which were considered most likely to influence the jet interference in this region were evaluated.

SYMBOLS

A	area, meters^2
A_{max}	maximum cross-sectional area of model, meters^2
B	jet total temperature weighting factor
C	entrainment constant
$C_{D,aft}$	afterbody pressure-drag coefficient, $\frac{D_{aft}}{q_\infty A_{max}}$
$C_{D,jet\ on}$	afterbody pressure-drag coefficient at jet on conditions
$C_{D,jet\ off}$	afterbody pressure drag coefficient at jet off conditions
C_p	pressure coefficient, $\frac{p - p_\infty}{q_\infty}$
$D_{,aft}$	afterbody pressure-drag, newtons
d	diameter, meters
d_{max}	maximum diameter of the model, meters
f	distance from nozzle throat to exit (see fig. 4), meters
i	integer
K	Kelvin
ℓ	length of afterbody meters
M	Mach number
MOM	momentum, $\frac{\text{kilograms meters}}{\text{second}}$
m_{ent}	mass of fluid entrained, kilograms
n	integer

p	pressure, $\frac{\text{kilograms}}{\text{meter}^2}$
q_∞	free-stream dynamic pressure, $\frac{\text{kilograms}}{\text{meter}^2}$
R	gas constant, $\frac{\text{joules}}{\text{kilogram K}}$
RN	Reynolds number
r	radial distance from model centerline, meters
r_e	radius of nozzle exit, meters
s	length of convergent portion of nozzle (see fig. 4), meters
T	temperature, Kelvin
T_{DP}	free-stream dew point temperature, Kelvin
$V_{j,\ell}$	local speed of the jet exhaust, $\frac{\text{meters}}{\text{second}}$
V_∞	speed of the free-stream, $\frac{\text{meters}}{\text{second}}$
w	axial distance from nozzle exit, aft positive, meters
x	axial distance from tangent point of afterbody radius and forward section of model, positive aft (see fig. 4) meters
y	radial distance from model surface, meters
z	axial distance from nozzle throat, positive aft (see fig. 4), meters
β	afterbody boattail angle, angle between axis of symmetry and generatrix of model afterbody (see fig. 4), degrees

β_j	$(M_j^2 - 1)^{1/2}$
β_∞	$(M_\infty^2 - 1)^{1/2}$
γ	ratio of specific heats
δ_j	calculated initial inclination angle of the jet exhaust plume, degrees
ζ	$\delta_j + \beta$
θ	angle the boundary layer rake probes make with axis of symmetry of model (see figure 7), degrees
ϕ	angular location measured in a plane perpendicular to axis of symmetry of model, clockwise direction positive when viewed from rear, 0° at top of model degrees
$\Delta\nu$	difference between Prandtl-Meyer turning angles of the jet exhaust just inside the nozzle exit and just downstream of the nozzle exit
ρ	density, $\frac{\text{kilograms}}{\text{meter}^3}$

Subscripts:

aft	afterbody
b	base
bl	boundary layer
DP	dew point
des	design
e	exit
edge	conditions at the outside edge of the boundary layer
ent	entrained
j	jet

ℓ	local conditions just downstream of the jet exit
max	maximum
noz	internal nozzle wall
r	rake
s	static
t	total
te	trailing edge
th	nozzle throat
∞	free-stream

EXPERIMENTAL APPARATUS AND PROCEDURE

Test Matrix and General Procedure

The jet interference on afterbody drag was investigated using four different jet exhaust gases for each of four afterbody configurations. An afterbody with strong adverse pressure gradients with separated flow, and one with more gentle pressure gradients and unseparated flow were tested. Each were tested with a sonic and a Mach 2 jet exit. The investigation was made on single nacelle models in the Langley 16-foot transonic wind tunnel. Tests were conducted at free stream Mach numbers from 0.60 to 1.20, and at an angle of attack of 0°. The gas parameters and test matrix are listed below:

JET EXHAUST GAS PARAMETERS

Gas	Decomposition products of:	γ	R, $\frac{\text{joules}}{\text{kg K}}$	T_t, K
1 (air)	-	1.4	287.04	300
2 (64.6% steam, 35.4% oxygen)	75% H_2O_2	1.301	389.86	646
3 (61.5% steam, 38.5% oxygen)	82% H_2O_2	1.282	383.78	810
4 (57.5% steam, 42.3% oxygen)	90% H_2O_2	1.265	376.19	1013

TEST MATRIX

CONFIGURATION				JET EXHAUST GASES	FREE STREAM MACH NUMBER RANGE
NUMBER	β, deg	ℓ/d_{max}	EXIT MACH NUMBER		
1	20°	1.0	1	1,2,3,&4	0.6 → 1.2
2	10°	1.5	1	1,2,3,&4	0.6 → 1.2
3a & 3b	20°	1.0	2	1,2,3,&4	0.6 → 1.2
4a & 4b	10°	1.5	2	1,2,3,&4	0.6 → 1.2
5 (forward boundary layer)	20°	1.0	1	2,3,&4	0.6 → 1.2
6 (rear boundary layer)	20°	1.0	1	2,3,&4	0.6 → 1.2

Standard procedures at the Langley 16-foot transonic tunnel were used in obtaining the basic quantities such as pressures. During a tunnel run, the tunnel Mach number was set and held constant while a sweep of the jet pressure ratio was made with data being taken at discrete values of pressure ratio. All conditions were held essentially constant while data were being recorded.

Data were taken at the highest Mach numbers first, and then at progressively lower Mach numbers to keep the variation in the tunnel total temperature small. To account for small cyclic variations in the desired test conditions, five frames of data for each data point were recorded within one second, and the average of these was used to compute the data. The data reduction procedures are given in Appendix A.

Model

General - To investigate the jet interference of the four different jet exhaust gases, both an air model and a hydrogen perioxide model were used because of the manner in which hydrogen peroxide must be decomposed to produce the gaseous jet exhaust. Both models had exactly the same external contours; and were cylindrical nacelles with semi-ogive noses. The various afterbodies were attached to the basic models.

The models were supported from the nose by a sting-strut arrangement which positioned the centerline of the models on the centerline of the tunnel. A photograph of the model installed in the tunnel is shown in figure 1. Figure 2 shows the general arrangement of the model.

Air model - The arrangement of the air model is shown in figure 2(a). In this sketch, the path of the air is indicated by arrows. The air is introduced perpendicular to the model axis through eight

sonic nozzles equally spaced radially around a central core. There are two flow smoothing plates, each having a lattice work of sharp edged holes drilled in an equilateral triangular pattern. The jet total temperature and pressure were obtained from a rake as illustrated. Details of the rake are shown in figure 3.

Hydrogen peroxide model - The general arrangement of the hydrogen peroxide model is shown in figure 2(b). The hydrogen peroxide is decomposed by a silver screen catalyst bed in the decomposition chamber which produces a gas composed of a mixture of steam and oxygen. The mass ratio of the steam and oxygen, and hence the specific heat, gas constant, and total temperature of the mixture are determined by the concentration of the hydrogen peroxide.

The internal section of the hydrogen peroxide model from immediately forward of the flow smoothing plates, see figure 2b, to the nozzle contour had the same dimensions as the air model.

Insulation was installed between the inner and outer shells of the afterbody to minimize heat transfer and maintain the same external skin temperatures of the air and hydrogen peroxide models.

Afterbodies - Figure 4 gives the dimensions of the four afterbodies tested. Basically, they consisted of two external contours each with a sonic and supersonic jet exit. The external contours of all the afterbodies began at model station 144.78, and the base diameters of all the afterbodies were equal. The rim at the base was kept as small as practical.

One external contour, which had a boattail angle at the exit of 20° and a length to maximum diameter ratio of 1.0, had strong adverse pressure gradients and separated flow at some conditions. The other, which had a boattail angle of 10° and a ℓ/d_m of 1.5, had more gentle pressure gradients, and generally had unseparated flow.

The two jet exit conditions chosen were a sonic exit and a Mach 2 exit. For the nozzles with the Mach 2 exits, the divergent part of the supersonic contours was designed by an irrotational method of characteristics with a stream function method of determining the inviscid isentropic contour. The method is described in reference 10. Two supersonic contours were designed, one for the air nozzles, and one for the hydrogen peroxide nozzles.

Pressure orifices on both the external and internal contours were placed as close to the exit as physically practical. Tables 1 and 2 give the orifice locations.

Cross sectional area distributions of the model with the short afterbody and of the support system are given in figure 5. Examples of theoretical pressure distributions calculated by an axisymmetric curved boattail method of characteristics (reference 11), and by an axisymmetric potential flow method in which the body is represented by sources and sinks distributed along its surface (reference 12) in figure 6.

Boundary layer rakes - The boundary layer was measured on the model surface at the beginning and near the trailing edge of the afterbody with the steep boattail angle. Sketches of the rakes used and their locations are presented in figure 7. The local flow angle at the rear rake was predicted from potential flow calculations described in reference 12. The design of the probe tips (see figure 7) was such that accurate total pressure readings could be obtained for misalignments of the probe with the local flow up to angles of 10°.

Wind Tunnel

This investigation was conducted in the Langley 16-foot transonic wind tunnel which is a single return, continuous, atmospheric wind

tunnel with an octagonal, slotted, test section. The Mach number is continuously variable from 0.2 to 1.3. Further details of the wind tunnel are given in reference 13.

Measurements and Instrumentation

Model - Static pressures were measured on the model afterbodies and in the boundary layer, on the nozzle internal surface, and in the jet exhaust at the nozzle exit plane. Total pressure measurements were made in the jet exhaust flow and in the model boundary layer. The pressures were measured with individual strain gage pressure transducers calibrated to an accuracy of ± 0.5 percent of the capacity of the gage.

Temperatures were measured on the surface of the model afterbody, on the internal nozzle surface, in the jet exhaust flow, and in the model boundary layer with swaged wire thermocouples. Iron-constantan swaged wire with an accuracy of ± 0.6K was used for the air model, while the higher temperature capacity chromel-alumel swaged wire with an accuracy of ± 2.2K was used for the hydrogen peroxide model and the boundary layer measurements.

ANALYSIS OF EXPERIMENTAL RESULTS

Factors Influencing Jet Interference

As the jet exhausts from the nozzle exit, it influences the afterbody pressures in two ways: by presenting a body which the external flow must negotiate, plume blockage, and by entraining fluid from the vicinity of the afterbody. These two effects oppose each other, with the plume blockage tending to raise the afterbody pressures, and the entrainment tending to lower them. Both of these effects are strong functions of the gas properties of the jet exhaust.

The manner in which the exhaust gas physical properties affect the jet plume shape and entrainment, and hence influence the jet interference on afterbody drag is the subject of this investigation. Figure 8 illustrates plume blockage and entrainment, and includes other flow parameters (free stream conditions, jet exhaust profiles, and afterbody boundary layers) which can influence the magnitude of the jet interference on the afterbody pressures.

During the investigation, the jet exhaust profiles and afterbody boundary layers were monitored for each exhaust gas to insure that these flow conditions were constant. The variation in the free stream parameters between tunnel runs was small, and the jet exhaust profiles for each exhaust gas were relatively flat and uniform. Also, the variation in the model external skin temperatures between the exhaust gases was generally small except very near the nozzle exit. The small skin temperature variations had no effect on the forward boundary layer, and only a slight, if any, effect on the one at the model trailing edge. Therefore, any differences in jet interference between the four exhaust gases should be due mainly to the effect of the properties of the exhaust gases on plume blockage and entrainment. A more thorough discussion of the additional parameters is given in Appendix B.

Jet Interference Correlation Parameters

Plume blockage parameters - Since the jet exhaust influences the afterbody pressures by plume blockage effects and by entraining fluid from the vicinity of the afterbody, the jet interference correlation parameters would be those parameters on which these two effects depend. Of the many parameters suggested in reference 9, only those which were considered most likely to correlate these two effects were evaluated.

The plume blockage interference would obviously be a function of the shape of the jet exhaust boundary. As discussed in reference 14, the most important factor determining the shape of the jet boundary is it's initial inclination angle. That matching this

angle does match the initial jet plume shape well in a quiescent atmosphere was verified for several exhaust gases in reference 15.

In reference 9, the first term of a series expansion of the ratio of p_ℓ/p_e gives:

$$p_\ell/p_e = 1 - \frac{\gamma_j M_e^2}{\beta_j} (\Delta\nu) + \ldots \qquad (1)$$

where the subscript ℓ denotes the conditions to which the jet is expanding, $\beta_j = (M_e^2 - 1)^{1/2}$, and $\Delta\nu$ is the difference in the Prandtl-Meyer turning angles for the jet exhaust in expanding from M_e to M_ℓ. The following similarity parameters were then suggested for the jet boundary.

Jet boundary in a quiescent medium	$(1 - \frac{p_\infty}{p_e})\ (\frac{\beta_j}{\gamma_j M_e^2})$
Jet boundary in a moving stream	$\frac{(p_e - p_\ell)\ p_\infty\ \beta_j\ \gamma_\infty\ M_\infty^2}{(p_\ell - p_\infty)\ p_e\ \beta_\infty\ \gamma_j\ M_e^2}$

In addition to these parameters from reference 9, the initial inclination angle of the jet exhaust, δ_j, was itself calculated to be used as a jet boundary simulation parameter (see sketch (a)). To calculate δ_j, it was assumed that the measured afterbody trailing edge pressure, $p_{aft,\ te}$, was

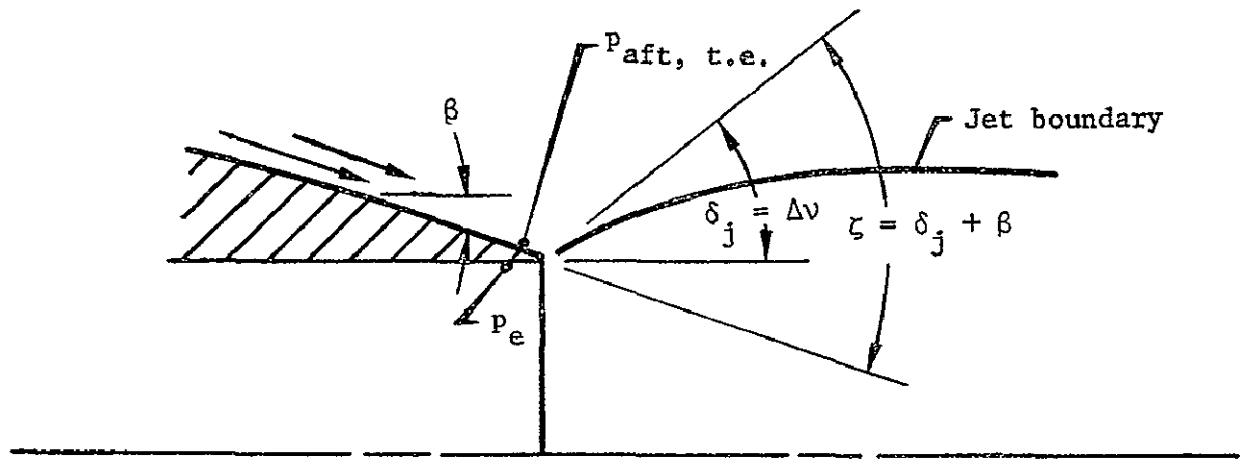

Sketch (a)

the pressure to which the jet exhaust was expanding upon leaving the nozzle. Then, using $p_{aft,te}$, the measured jet exit pressure, p_e, and the jet total pressure, δ_j was calculated from the Prandtl-Meyer relations.

If the external flow on the afterbody were not separated, it would have to turn through an angle of

$$\zeta = \delta_j + \beta \qquad (2)$$

at the afterbody trailing edge. This angle was used in an attempt to correlate the interference due to plume blockage for afterbodies with different boattail angles.

Jet entrainment parameters - The entrainment of fluid from the vicinity of the afterbody by the jet exhaust depends on, among other things, the momentums of the jet exhaust and local afterbody flow, and the velocities, energies, and mixing

characteristics of the two flows. Considering this, the following simulation parameters suggested in reference 9 were considered the ones most likely to correlate the jet interference due to entrainment.

$$(\text{Mass flow})^2 \qquad \frac{p_e^2 \gamma_j M_e^2 R_\infty T_\infty A_e^2}{p_\infty^2 \gamma_\infty M_\infty^2 R_j T_j A_\infty^2}$$

$$\text{Momentum} \qquad \frac{p_e \gamma_j M_e^2 A_e}{p_\infty \gamma_\infty M_\infty^2 A_\infty}$$

$$\text{Kinetic energy per unit mass} \qquad \frac{\gamma_j M_e^2 R_j T_e}{\gamma_\infty M_\infty^2 R_\infty T_\infty}$$

$$\text{Internal energy per unit mass} \qquad \frac{(\gamma_\infty - 1) R_j T_e}{(\gamma_j - 1) R_\infty T_\infty}$$

The maximum cross sectional area of the model, A_{max}, was substituted for A_∞ in these equations.

Assuming the entrainment was more likely dependent on the jet exhaust conditions just downstream of the exit instead of those just inside the exit, the parameters above were computed for the local conditions just downstream of the exit as well as for the jet exit conditions. The static pressure in this region was assumed to be $p_{aft,te}$. The velocity ratio:

$$\frac{V_{j,\ell}}{V_\infty}$$

was also used to correlate the entrainment.

Correlation of Experimental Data

Magnitude of differences in jet interference - Figure 9 shows an example of the interference of the jet exhaust on the afterbody pressure coefficients. The data is presented for one exhaust gas at several values of jet pressure ratio. It can be seen that the jet exhaust generally tends to increase the pressures on the afterbody above their jet off level. Pressure coefficients such as these were integrated to obtain afterbody drag coefficients.

Examples of the drag coefficients plotted as a function of jet total pressure ratio are presented in figure 10 for all the exhaust gases tested. It can be seen from the jet off data, $p_{t,j}/p_\infty = 1.0$, that there were slight differences in the jet off drag coefficients as each jet exhaust gas was tested. In order to present the differences in the interference of the various exhaust gases accurately, the data is presented in the form of jet interference on afterbody drag normalized by the jet off drag coefficient, or as:

$$\frac{C_{D,\ \text{jet on}} - C_{D,\ \text{jet off}}}{C_{D,\ \text{jet off}}}$$

A negative value would indicate favorable jet interference. Figures 11 through 14 present, in this form, all the data as a function of jet total pressure ratio, jet static pressure ratio, and initial jet inclination angle. The averages of the jet off drags for each configuration and condition are included to help assess the absolute magnitudes of the differences between the jet interference of each exhaust gas.

Figures 11 through 14 show that there are substantial differences between the jet interferences of the four jet exhaust gases. Depending on the configuration and freestream Mach number, the differences between the jet interference of the various exhaust gases generally ranged from 10 to 20 percent of the jet off drag at the low jet pressure ratios, and up to 35 percent of the jet off drag when compared at a jet exit pressure ratio of 3. Air, when used as the jet exhaust, consistently results in the least favorable jet interference and therefore the highest drag. The exhaust gases having ratios of specific heats and total temperatures of 1.30 and 646K, 1.28 and 810K, and 1.26 and 1013K result in increasingly more favorable jet interference and less drag. The only two exceptions to this pattern are for the combination of the long afterbody with a sonic exit, the jet exhaust gas having a γ of 1.30 (gas 2), and $M_\infty = 0.60$ or 0.80 (figures 12 (a) and 12 (b)). For these combinations, gas 2 gives the most favorable jet interference. However, these deviations from the pattern are misleading. For these conditions, the actual magnitudes of the jet interference of all the exhaust gases are very nearly equal, and the jet off drag is quite low. Therefore, dividing by the low jet off drag magnifies any irregularities in the measurements.

Based on percentage of jet off drag, there are large differences between the jet interference of the various exhaust gases at all subsonic Mach numbers. However, the greatest differences between the actual magnitude of the interference of the gases is at the high subsonic and transonic Mach numbers, $M_\infty = 0.90$ and 0.95. At these Mach numbers, the steep adverse pressure gradients are probably easily influenced by plume blockage, and the large nonjet-induced separated regions (fig. 9) could be easily influenced by entrainment. At the low subsonic Mach numbers, the magnitude of the difference between the jet interference of the various exhaust gases was not very large even though differences based on the jet off drag were on the order of 30 to

35 percent. This is particularly true for the afterbody with a boattail angle of 10° which had values of jet off drag coefficients of .031 and .035 at free-stream Mach numbers of 0.60 and 0.80. At a Mach number of 1.20, the increments between the jet interference for the various gases are small when based on the percentage of jet off drag. Also, the differences in magnitude between the jet interference of the various gases were greater for the afterbody with a boattail angle of 20° than for the one with an angle of 10°. This effect is also probably due to the more adverse pressure gradients and greater regions of non jet-induced separation for the steep afterbody. Figure 15 illustrates these two points.

For the configuration with a jet exit Mach number of 2, the jet exit static pressure ratios were not high enough for the jet exhaust to expand very much. The differences in jet interference between the various exhaust gases for these configurations are similar to the differences for the configurations with Mach 1 exits at the lower jet pressure ratios (figures 11 through 14).

For operating conditions typical of high nozzle drag (high boattail angles, and transonic speeds and corresponding jet pressure ratios) the current data indicate that the use of air to simulate a dry-turbojet exhaust can result in an increase of afterbody drag amounting to as much as 20 percent of the dry turbojet value (fig. 15).

Correlation of exhaust plume blockage.- To correlate the jet interference of several exhaust gases, both the plume shape effects and entrainment effects of the jet exhausts on the afterbody drag must be accounted for. If this were done, the jet interference of all the exhaust gases as a function of the correlating parameter would fall on a single curve. This section deals with an attempt to account for only the differences in interference due to plume shape effects of the various gases.

Figures 11 and 12 present the jet interference of the four exhaust gases for the configurations with the sonic jet exits. These figures show that there is a discrepancy between the jet interference of the four exhaust gases at all values of jet pressure ratio. As a function of jet total pressure ratio, the discrepancy diverges as pressure ratio is increased. Comparing the interference as a function of the jet exit static pressure ratio, this discrepancy increases at a slightly lower rate.

A comparison of the interferences as a function of the intial inclination angle of the jet exhaust, δ_j, also shows differences between the jet interferences of the four exhaust gases. However, at the high pressure ratios and hence high plume angles, the discrepancy is reduced even more than for the comparison using exit static pressure ratio. For each freestream Mach number and configuration, the differences between the jet interference of the four jet exhaust gases seem to be relatively constant with δ_j. The initial plume angle probably gives a good representation of the initial shape of the jet plume in a moving stream as it does in a quiescent atmosphere (reference 15). Therefore, the discrepancies between the jet interference of the four jet exhaust gases at a constant value of δ_j should be mainly due to entrainment.

Figures 13 and 14 present the data for the configurations with the Mach 2 jet exits. Since the initial inclination angle of the jet plume was computed using the Prandtl-Meyer relations, the magnitudes of the negative angles presented in these figures are slightly in error.

The maximum values of exit pressure ratio or initial plume angle for the configurations with Mach 2 jet exits were not large enough to determine if the trends just mentioned were valid for these configurations. However, for these configurations, δ_j seems to be at least as good a parameter as jet pressure ratio with which to compare the jet interference of the various exhaust gases. Therefore, the data seems to indicate that δ_j is a more relevant parameter for comparing the

jet interference of underexpanded jets than either $p_{t,j}/p_\infty$ or p_e/p_∞. The use of δ_j instead of p_e/p_∞ or $p_{t,j}/p_\infty$ would be more helpful when high jet exhaust plume angles are expected.

For the afterbody with a boattail angle of 20° at a free-stream Mach number of 0.95, the jet interference was relatively insensitive to plume angle up to a value of $\delta_j \geq 18°$ (figure 11 (d)). This effect can possibly be expalined by considering figures 9 and 16. At a Mach number of 0.95, there is a large separated region on the afterbody. From figure 9, configuration 1, after the jet is initially turned on, increases in jet pressure ratio at first tend to aspirate the separated region and lower the afterbody pressures. Further increases in jet pressure ratio only tend to raise the pressures slightly. This occurs until very large values of pressure ratio are reached. At these large values of pressure ratio, the ratio of the jet plume diameter to that of the separated region is probably large enough for the plume blockage effects to again predominate. This is also illustrated by figure 16 (a) and (b) which show the afterbody pressure distributions for each exhaust gas. The pressure distributions are interpolated for constant values of p_e/p_∞ and $p_{t,j}/p_\infty$. The interference of the jet exhaust on the distributions is mainly limited to the separated region of the afterbody until large values of jet plume angle are attained.

Figure 17 presents the jet interference as a function of the initial inclination angle of the jet plume and of the plume boundary correlation parameters suggested in reference 9. These parameters are intended for plume boundary correlation in a quiescent atmosphere and a moving stream. The comparison is shown for the afterbody with a boattail angle of 20°. An exit Mach number of 2 was used because the parameters are zero for an exit Mach number of 1. For the range of plume angles attained, all the parameters seem to give equal results. However, due to the β_j and β_∞ terms, at free stream and jet exit

Mach numbers near 1, the two parameters suggested by reference 9 can either diverge or approach zero. Therefore δ_j seems to be the best of the three with which to correlate jet interference.

A comparison of the jet interference versus δ_j for a sonic jet exit and a Mach 2 jet exit is shown in figure 18. The initial inclination angle of the jet plume does not correlate the jet interference for the two jet exit Mach numbers. At a jet plume angle of 0°, the Mach 2 exit gave less favorable jet interference which probably indicates more entrainment. This effect was also observed in reference 16. The jet interference of the Mach 2 exit tends to become more favorable than that of the sonic exit as the plume angle is increased.

By adding the afterbody boattail angle to the initial inclination angle of the jet plume, a hypothetical trailing edge flow turning angle, ζ, was obtained. This angle was used in an attempt to correlate the change in afterbody drag coefficient due to plume blockage for different afterbody boattail angles. Figure 19 presents the jet interference of the afterbodies with boattail angles of 20° and 10° as a function of ζ. The angle, ζ, may have some use as a correlating factor between afterbodies of different shapes when the freestream Mach number is low and there is no separation. However, ζ fails to correlate the jet interference of afterbodies with different amounts of non jet-induced separation, therefore the use of this parameter is not recommended.

Correlation of entrainment - In addition to plume blockage, the jet exhaust influences the afterbody pressures by entraining fluid from the vicinity of the afterbody. The amount of fluid entrained is partially governed by the momentums of the jet exhaust and local afterbody flow, and the velocities, energies, and mixing characteristics of the two flows.

Figure 20 presents a summary of the jet interference of the various exhaust gases as a function of several parameters from

reference 9, and of R_j T_e and γ_j. The parameters presented are the ones considered most likely to correlate the entrainment. The values of each parameter are computed for the jet exit conditions. The afterbody with a boattail angle of 20° was chosen for this comparison because of it's greater jet interference.

The four points on each curve represent the four jet exhaust gases tested. The values for each point were obtained from crossplots at a constant initial jet plume angle. Since each plot is for a constant initial plume angle, it is assumed that any differences between the jet interferences are mainly due to differences in entrainment. Entrainment tends to make the jet interference more positive, so increasing entrainment would be in an upward direction on the figure.

Figure 20 shows that the entrainment is not a simple function of any of the parameters presented. For example, the Mach 2 exit, with its greater exit momentum and mass flow, has approximately the same jet interference as the sonic exit. Since the initial plume angles are the same, equal jet interference would mean equal entrainment. If the entrainment were just a function of exit momentum, the points for each nozzle would lie on the same curve. The same reasoning can be applied to show that entrainment is not a simple function of the other parameters.

The interaction of the jet exhaust with the external flow takes place downstream of the nozzle exit. Thus, entrainment would seem to be more dependent on the jet conditions downstream of the nozzle than the conditions inside the exit. With this in mind, the correlating parameters were recomputed for the conditions just downstream of the nozzle exit. For these calculations, the local jet static pressure was assumed to be equal to the afterbody trailing edge pressure.

The momemtum of the entraining fluid is generally considered a major factor determining the quantity of fluid entrained. In

reference 17, the following equation is given for the mass of fluid entrained by a jet in a quiescent atmosphere.

$$\frac{1}{MOM_{j,\ell}^{1/2}\ \rho_\infty^{1/2}} \frac{dm_{ent.}}{d_w} = C$$

or

$$\frac{dm_{ent}}{d_w} = C\ (MOM_{j,\ell})^{1/2}\ \rho_\infty^{1/2} \qquad (3)$$

In this equation, m_{ent} is the mass of the surrounding fluid entrained, $MOM_{j,\ell}$ is the momentum flux of the jet exhaust, ρ_∞ is the density of the surrounding fluid, w is the axial distance downstream of the nozzle exit, and C is a constant. Thus the equation predicts that the entrainment varies as the square root of the exhaust momentum. This parameter, computed for the local jet exhaust conditions, is presented in figure 21. As mentioned previously, entrainment tends to lower the afterbody pressures, so as entrainment increases, the jet interference becomes less negative.

Figure 21 shows that even compared on the basis of the square root of the local momentum of the jet flow, the entrainment of the sonic exit and Mach 2 exit do not correlate. The jet exhaust Reynolds numbers based on the exit diameters of the nozzles ranged from 3.71×10^5 to 20.9×10^5 for the sonic nozzle, and from 5.60×10^5 to 25.7×10^5 for the Mach 2 nozzle. Reference 17 reports that for values greater than 6×10^4, the entrainment coefficient, C, is independent of exhaust Reynolds number. Then jet exhaust Reynolds number should not account for the fact that the entrainment

of the two exits do not correlate. This may indicate that entrainment is dependent on the jet exhaust Mach number and factors other than the momentum of the jet exhaust.

The parameters $V_{j,\ell}/V_\infty$, γ_j, $R_jT_{j,\ell}/R_\infty T_\infty$, and local kinetic energy per unit mass, figures 22 through 24, also fail to correlate the entrainment of the two nozzle exits. However, for each exit and for each plume angle, the effects of entrainment of the various gases is close to a straight line function of these parameters. The local kinetic energy parameters seems to be the best in this respect.

Reference 18 indicates the independence of the jet mixing on the ratio $R_jT_{t,j}/R_\infty T_{t,\infty}$ if smooth, uniform jet flow is assumed. The velocity and kinetic energy parameters are themselves functions of this ratio. At a constant jet exhaust plume angle, the measured values of jet interferences decrease as this ratio increases.

Reference 18 also indicates that the mixing process alters the effective jet boundary shape so that the external inviscid flow is affected. This could explain why the jet interference became more favorable as the ratio $R_jT_{j,\ell}/R_\infty T$ increased. An increase in the jet exhaust diameter would increase the afterbody pressures and result in a more favorable jet interference. However, consider figure 11 (d). For this particular set of conditions the jet interference is only slightly affected by the initial jet plume angle between values of δ_j from 1° to 12°. Yet, there are considerable differences between the jet interference of the four exhaust gases in this range of plume angles. The differences in interference in this case seem to be more likely due to entrainment of fluid from the vicinity of the afterbody.

Regardless of the physical explanation, the relatively straight lines of the RT and kinetic energy parameters, figures 23 and 24, suggest that they may be used to adjust for entrainment of various gases. Using either parameter, two points on the curve would have to be experimentally established at the proper plume angle for a

particular configuration. Then a straight line interpolation to the value of the parameter for the real jet exhaust gas may give an extimate to the correct jet interference. However, the entrainment seem to depend on the jet exhaust Mach number and the external flow conditions. Thus, the effects of entrainment for one configuration and set of conditions should not be used to predict that of another configuration or set of conditions.

APPLICATION OF JET SIMULATION PARAMETERS

The preceding discussion has established the importance of simulating the jet plume blockage and entrainment effects. It has been demonstrated that the jet plume blockage effects can be duplicated for various exhaust gases by matching the initial inclination angle of the jet exhaust plume. Corrections to wind-tunnel values for entrainment, however, must be evaluated from results for at least two exhaust simulation gases.

An example of the procedure for adjusting the experimental value of jet interference to full-scale conditions is shown in figure 25. First, experimentally determine the variation of afterbody drag with jet pressure ratio for at least two jet exhaust gases. The, correct for plume shape differences by realting the drag to the initial plume angle of the jet exhaust, and obtain a value of drag at the operating plume angle of the aircraft. Final adjustments to the jet interference for any discrepancies in entrainment could then be made by interpolating with the kinetic energy parameter or the RT ratio as is illustrated in figure 25.

CONCLUDING REMARKS

Based on the range of the jet exhaust gas parameters tested and other variables of the investigation, the folliwng results are indicated.

Substantial differences were obtained between the jet interference on afterbody drag for the four jet exhaust gases tested. Depending on

the configuration and freestream Mach number, the differences generally ranged from 10 to 20 percent of the jet off drag at the low jet pressure ratios, and up to 35 percent of the jet off drag at a jet exit static pressure ratio of 3. Air, when used as the jet exhaust, consistently gave the least favorable jet interference and therefore the highest drag. The exhaust gases having ratios of specific heats, gas constants, and total temperatures of: 1.30, 390 joules/kg K, and 646K; 1.28, 384 joules/kg K, and 810K; and 1.26, 376 joules/kg K, and 1013K, resulted in increasingly more favorable jet interference and less drag.

Although, based on percentage of jet off drag, there were large increments between the jet interference of the various gases at all subsonic Mach numbers, the actual magnitude of the increments was greatest for the combination of high boattail angles and high subsonic and transonic Mach numbers. For operating conditions typical of high nozzle drag (high boattail angles, and transonic speeds and corresponding pressure ratios) the current data indicate that the use of air to simulate dry-turbojet exhaust can result in an increase of afterbody drag amounting to as much as 20% of the dry-turbojet value.

The differences in jet interference between the various exhaust gases are attributed to different plume shapes and entrainment properties of the gases. Corrections for the plume shape differences can be made by relating the drag to the computed plume angle. Although the entrainment differences are difficult to predict, they seem to be a relatively straight line function of the product of the jet exhaust gas constant and local temperature, and also of the local jet exhaust kinetic energy per unit mass.

REFERENCES

1. Runckel, Jack F.: Interference Between Exhaust System and Afterbody of Twin-Engine Fuselage Configurations. NASA TN D-7525, 1974.

2. Lee, Edwin E., Jr.; and Runckel, Jack F.: Performance of Closely Spaced Twin-Jet Afterbodies with Different Inboard-Outboard Fairings and Nozzle Shapes. NASA TM X-2329, 1971.

3. Cortright, Edgar M., Jr.; and Kochendorfer, Fred D.: Jet Effects on Flow Over Afterbodies in Supersonic Stream. NACA RM E53H25, 1953.

4. Hearth, Donald P.; and Wilcox, Fred A.: Thrust and Drag Characteristics of a Convergent-Divergent Nozzle With Various Exhaust Jet Temperatures. NACA RM E53L23b, 1954.

5. Henry, Beverly Z., Jr.; and Cahn, Maurice S.: Preliminary Results of an Investigation at Transonic Speeds to Determine the Effects of a Heated Propulsive Jet on the Drag Characteristics of a Related Series of Afterbodies. NACA RM L55A24a, 1955.

6. Baughman, L. Eugene; and Kochendorfer, Fred D.: Jet Effects on Base Pressures of Conical Afterbodies at Mach 1.91 and 3.12. NACA RM E57E06, 1957.

7. Beke, Andrew; and Simon, Paul C.: Thrust and Drag Characteristics of Simulated Variable-Shroud Nozzles With Hot and Cold Primary Flows at Subsonic and Supersonic Speeds. NACA RM E54J26, 1955.

8. Lee, George: An Investigation of Transonic Flow Fields Surrounding Hot and Cold Sonic Jets. NASA TN D-853, 1961.

9. Pindzola, M.: Jet Simulation in Ground Test Facilities. AGARD-ograph 79, 1963.

10. Johnson, Charles B.; Boney, Lillian R.; Ellison, James C.; and Erickson, Wayne D.: Real-Gas Effects on Hypersonic Nozzle Contours with a Method

of Calculation. NASA TN D-1622, 1963.

11. Wilmoth, Richard G.: Unpublished Fortran Program for Calculating the Pressure Distributions on Axisymmetric Afterbodies by the Method of Characteristics. 16-Foot Transonic Tunnel Branch, Langley Research Center, 1968.

12. Hess, J. L.; and Smith, A. M. O.: Calculation of Potential Flow About Arbitrary Bodies. Volume 8 of Progress in Aeronautical Sciences, D. Kucheman et, at eds. Pergamon Press, 1967, pages 1-138.

13. Corson, Blake W., Jr.; Runckel , Jack F.; and Igoe, William B.: Calibration of the Langley 16-Foot Transonic Tunnel with Test Section Air Removal. NASA TR R-423, 1974.

14. Love, Eugene S.; Grigsby, Carl E.; Lee, Louise P.; and Woodling, Mildred J.: Experimental and Theoretical Studies of Axisymmetric Free Jets. NASA TR R-6, 1959.

15. Herron, R. D.: An Investigation of Jet Boundary Simulation Parameters for Underexpanded Jets in a Quiescent Atmosphere. AIAA Third Aerodynamic Testing Conference, AIAA Paper 68-397, 1968.

16. Berrier, Bobby Lee; and Wood, Frederick G., Jr.: Effect of Jet Velocity and Axial Location of Nozzle Exit on the Performance of a Twin-Jet Afterbody Model at Mach Numbers up to 2.2 NASA TN D-5393, 1969.

17. Hill, B. J.: Measurement of Local Entrainment Rate in the Initial Region of Axisymmetric Turbulent Air Jets. Journal of Fluid Mechanics, 1972, vol. 51, part 4, pp. 773-779.

18. Jaarsma, F.: Engine Airplane Interference in Transonic Tests. AGARD Advisory Report No. 36, part II, pp. II-65.

19. Salters, Leland B. Jr.; and Chamales, Nicholas C.: Studies of Flow Distortion in the Tailpipes of Hydrogen Peroxide Gas Generators Used for Jet-Engine Simulation. NASA TM X-1671, 1968.

APPENDIX A

Data Reduction

This appendix describes the procedures used to reduce the measured quantities to coefficient form. To account for small cyclic variations in the desired test conditions, five frames of data for each data point were recorded within one second, and the average of these was used to compute the data.

Jet exhaust conditions - The stagnation conditions of the jet were obtained from the rake located just behind the flow smoothing plates, see figure 2. Incremental areas were assigned to the probes and the total pressure and temperature were obtained from the equations:

$$p_{t,j} = \sum_{i=1}^{10} A_{t,j_i} \, p_{t,j_i} \tag{A1}$$

and

$$T_{t,j} = \sum_{i=1}^{3} B_{t,j_i} \, T_{t,j_i} \tag{A2}$$

where $\sum_{i=1}^{10} A_{t,j_i} = 1$ and $\sum_{i=1}^{3} B_{t,j_i} = 1$. In these equations, j indicates conditions of the jet and i is an integer.

The static pressure at the nozzle exit was assumed to be the average of measurements made with the two static pressure taps nearest the nozzle exit. See table 2 for their exact locations. This assumption was a valid one as was pointed out in the discussion in

Appendix B. These values of static pressure were used for the jet exhaust exit condition when computing the various jet simulation parameters. The afterbody with the boundary layer rakes had no static orifices, so p_e, for conditions at which the nozzle was assumed choked, ie: when

$$p_{t,j}\left(\frac{2}{\gamma_{j+1}}\right)^{\frac{\gamma_j}{\gamma_j-1}} > p_\infty \tag{A3}$$

was calculated using the equation

$$p_e = p_{t,j}\left(\frac{2}{\gamma_j+1}\right)^{\frac{\gamma_j}{\gamma_j-1}} . \tag{A4}$$

External conditions - The afterbody drag coefficient was computed by assigning incremental areas to each pressure on the top row (at $\phi = 0°$) and using the equation

$$C_{D,aft} = \frac{-1}{A_{max}} \sum_{i=1}^{n} (C_{p,aft_i})(A_{aft_i}) \tag{A5}$$

where n is the number of orifices in the top row, and

$$\sum_{i=1}^{n} A_{aft_i} = A_{max} - A_e. \tag{A6}$$

It was assumed that the top row of orifice would be the row most nearly free of strut interference.

The boundary layer profiles were computed by substituting the pressures sensed by the rakes into either the equation:

$$M_{bl_i} = \left\{ 5\left[\left(\frac{p_{t,r_i}}{p_{s,r}}\right)^{\frac{\gamma_\infty - 1}{\gamma_\infty}} - 1\right]\right\}^{\frac{1}{2}} \qquad \text{(A7)}$$

if

$$\frac{p_{s,r}}{p_{t,r_i}} > \left(\frac{2}{\gamma_\infty + 1}\right)^{\frac{\gamma_\infty}{\gamma_\infty - 1}}$$

or the equation:

$$M_{bl_i} = \left(\frac{p_{s,r}}{p_{t,r_i}}\right)\left(\frac{\gamma_\infty + 1}{2}\right)^{\frac{\gamma_\infty}{\gamma_\infty - 1}}\left(M_{bl_i}\right)^{\frac{3\gamma_\infty - 1}{\gamma_\infty - 1}}\left[\frac{\gamma_\infty + 1}{2\gamma_\infty (M_{bl_i})^2 - (\gamma_\infty - 1}\right]^{\frac{1}{\gamma_\infty - 1}} \qquad \text{(A8)}$$

if

$$\frac{p_{s,r}}{p_{t,r_i}} \leq \left(\frac{2}{\gamma_\infty+1}\right)^{\frac{\gamma_\infty}{\gamma_\infty-1}} .$$

The integer, i, indicates the particular rake total pressure measurement in question. The second equation for M_{bl_i} was iterated until the residual was ≤ 0.0001 of the computed value of M_{bl_i}. The velocity profiles were computed using the free stream stagnation temperature as the stagnation temperature in the boundary layer. To check the validity of this assumption, boundary layer temperatures were measured with another set of rakes. The ratio of the actual velocity in the boundary layer to the velocity computed assuming free stream temperature would then be:

$$\frac{V_{actual}}{V_{computed}} = \frac{M_{bl_i}\, a_{bl_i\ actual}}{M_{bl_i}\, a_{bl_i\ computed}} = \left(\frac{T_{bl_i}}{T_\infty}\right)^{\frac{1}{2}} = \left(\frac{T_{t,bl_i}}{T_{t,\infty}}\right)^{\frac{1}{2}} \qquad (A9)$$

APPENDIX B

Factors Influencing Jet Interference

As the jet exhausts from the nozzle exit, it influences the afterbody pressures by presenting a body which the external flow must negotiate and by entraining fluid from the vicinity of the afterbody. The magnitude of these two effects are influenced by the free-stream conditions, jet exhaust profiles, and the condition of the flow on the afterbodies. The influence of these parameters on the jet interference of the various gases is discussed in the next three sections.

Free stream conditions - As in all aerodynamic phenomena, the Mach number and other conditions of the free stream are very important in determining the jet interference. Since the Langley 16-foot transonic wind tunnel is an atmospheric wind tunnel, the free stream conditions varied slightly during the investigation. Figure 26 shows the band versus Mach number of the free stream parameters encountered during the test. The variation in Reynolds number at a particular Mach number is primarily due to the variation in free stream total temperature. The break in the bands between Mach numbers 0.95 and 1.20 indicates that no data was taken in this Mach number range. The band width of the free stream parameters is small enough so that it doesn't substantially affect the jet interference.

Jet exhaust profiles - In considering the jet interference on afterbodies ahead of the jet exit, the conditions at the initial part of the jet plume are of more importance than those further downstream. Important factors determining the initial shape of the jet boundary and the entrainment of the external flow by the jet exhaust are the jet exit Mach number, pressure, and the shape of the exit profiles. Therefore, even though care was taken in the design of the model to insure profiles of a flat and uniform nature for each exhaust

gas, the actual exit profiles were verified statically with rakes. As can be seen by a study of reference 19, this was especially important for the hydrogen peroxide nozzles because flat exit profiles are difficult to obtain with these gas generators.

The pressure distributions on the nozzle walls were also measured and are shown in figure 27 as a function of jet pressure ratio.

Figure 28 presents profiles of the total pressure, static pressure, and total temperature ratios for two values of jet pressure ratio. The pressure ratios for the supersonic nozzles were the two highest which could be obtained statically with the jet mass flow available. The nozzle wall exit static pressures were obtained with the static pressure rake removed to avoid interference of the rake probes with the wall measurements. The exit profiles of the basic measured quantities were relatively flat and uniform for all the gases.

The exit velocity profiles were computed from the basic measurements and are presented in figure 29. These and the internal pressure distributions (figure 27) indicate that the jet total pressure ratio for the supersonic nozzles must generally be greater than 0.6 of its design value to insure a nominal exit Mach number of 2. Figures 28 and 29 show that the exit profiles for the various gases are relatively flat and uniform. This indicates that nonuniformity of the exit profiles was not a major factor in the differences in jet interference between the various exhaust gases.

Afterbody flow parameters - The entrainment of the fluid from the region of the afterbody, and the effect of the jet plume boundary on the afterbody pressures depends to a large extent on the nature of the flow on the afterbody. Figure 30 shows the jet off pressure distributions and boundary layer profiles for the afterbody with a boattail angle of 20°.

The Mach numbers in the boundary layer were computed using the static pressures measured at the tips of the boundary layer rakes (see figure 7). A comparison of the coefficients of the pressures

measured at the tips of the rakes with those measured on the model surface in the plane of the rake with the rake removed, figure 31, shows that the static pressures used to compute the boundary layer Mach numbers were in error. The profiles do serve the purpose, however, of giving an indication of the boundary layer shapes and the extent of the separated region on the afterbody.

The velocities in the boundary layer were computed assuming that the total temperature in the boundary layer was the same as the total temperature of the free stream. The square roots of the ratio of the total temperature in the boundary layer to that of the free stream show that this assumption gave very little error in that portion of the boundary layer which was not separated. The boundary layer temperature measurements at a Mach number of 1.2 were unreliable due to a thermocouple malfunction and are not presented.

Figure 30 shows that the afterbody skin temperatures had no effect on the forward boundary layer profiles. The rear profiles indicate that there is a very slight tendency for the boundary layer at the trailing edge to separate earlier ($M_\infty = 0.90$) for the hotter skin temperatures. Figure 32, which presents the trailing edge boundary layer profiles immediately before and after a jet pressure ratio sweep, shows the opposite trend. Which ever of these indicated trends is correct, the effect appears to be slight and the jet interference should not be appreciably affected.

The boundary layer profiles show that, for the Mach numbers tested, the greatest amount of separated flow on the afterbody with $\ell/d_m = 1.0$ occurs at a free stream Mach number of 0.95 and a smaller amount at Mach numbers of 1.20 and 0.90. At Mach numbers of 0.80 and 0.60 there appears to be no separation.

The data for the afterbody pressure distributions presented in figure 30 was taken just before and after each jet pressure ratio sweep to assess any effect of afterbody skin heating. The skin temperatures immediately after the jet was turned off were essentially the same as the hottest skin temperatures when the jet was

operating (see figure 33). At first, a comparison of the minimum values of the pressure coefficients in figure 30 for the air model with those for the hydrogen peroxide model seems to indicate that colder skin temperatures result in lower afterbody pressures. However, the pressure distributions for the hydrogen peroxide model seem to be consistent regardless of skin temperature, and some of those temperatures are at the same level as the temperatures for the air model. A check of the coordinates for the two afterbodies revealed a difference in model radius of up to 0.025 cm. Potential flow theory, reference 12, only accounts for about one third of the pressure coefficient difference between the two models, but it does substantiate the variations obtained in the pressure coefficient distributions.

It has been shown that, during the investigation, the width of the band of the various free stream parameters was small. Also, the jet exit profiles were shown to be relatively flat and uniform regardless of the jet exhaust gas, and the flow field in the vicinity of the afterbody was only very slightly, if at all, affected by the model skin temperatures. Hence, any difference in jet interference between the four exhaust gases should be mainly due to the differences in the properties of the exhaust gases themselves.

TABLE 1.- EXTERNAL INSTRUMENTATION LOCATIONS

Static Pressure Orifices

ϕ, deg	x/d_{max} for boattails: $\frac{l}{d_{max}} = 1.0$	$\frac{l}{d_{max}} = 1.5$	ϕ, deg	x/d_{max} for boattails: $\frac{l}{d_{max}} = 1.0$	$\frac{l}{d_{max}} = 1.5$
0	-0.833	-0.833	90	-0.500	-0.500
	-0.500	-0.500		0	0
	-0.167	-0.167		.200	.167
	0	0		.250	.220
	.125	.167		.300	.267
	.200	.200		.417	.417
	.250	.267		.567	.750
	.300	.417		.633	1.067
	.417	.583		.767	1.267
	.500	.750		.833	1.417
	.567	.917		.917	
	.633	1.000		.950	
	.700	1.067			
	.767	1.133	180	-0.833	-0.833
	.833	1.200		-0.500	-0.500
	.883	1.267		-0.167	-0.167
	.917	1.333		0	0
	.950	1.383		.125	.167
		1.417		.200	.220
				.250	.267
50	-0.500	-0.500		.300	.417
	0	0		.417	.750
	.125	.167		.567	1.000
	.200	.220		.633	1.133
	.250	.267		.767	1.267
	.300	.417		.833	1.383
	.417	.750		.917	1.417
	.567	1.067		.950	
	.633	1.267			
	.767	1.333			
	.833	1.417			
	.917				
	.950				

Surface Temperatures
($\phi = 0^{\circ}$ and 180°)

x/d_{max} = 1.0 for boattails	
l/d_{max} = 1.0	l/d_{max} = 1.5
-0.833	-0.833
0	0
.500	750
.833	1.200
.933	1.417

TABLE 2.- INTERNAL INSTRUMENTATION LOCATIONS

Static Pressure Orifices
Boattails with l/d_{max} = 1.0

ϕ, deg	z/d_{th}: Sonic nozzle	Supersonic nozzles γ=1.4	Supersonic nozzles γ=1.283
-5	-1.667	-2.164	-2.230
	-0.333	-0.433	-0.446
	0	0	0
	.333	.433	.446
	1.267*	1.299	1.784
		2.164	3.123
		3.030	4.015
		4.805*	5.498*
30	1.267*	4.805*	5.498*

* For configurations with l/d_{max} = 1.5, substitute the following values

Sonic nozzle	Supersonic nozzles γ=1.4	Supersonic nozzles γ=1.283
1.033	4.528	5.186

Surface Temperatures
($\phi = 15^{\circ}$)
Boattails with l/d_{max} = 1.0

z/d_{th}: Sonic nozzle	Supersonic nozzles γ=1.4	Supersonic nozzles γ=1.283
-1.667	-2.164	-2.230
0	0	0
1.267*	2.164	3.123
	4.805*	5.365*

* For configuration with l/d_{max} = 1.5, substitute the following values

Sonic nozzle	Supersonic nozzles γ=1.4	Supersonic nozzles γ=1.283
1.033	4.528	4.740

NOTE ϕ is measured clockwise when model is viewed from the rear. 0° is at the top of the model.

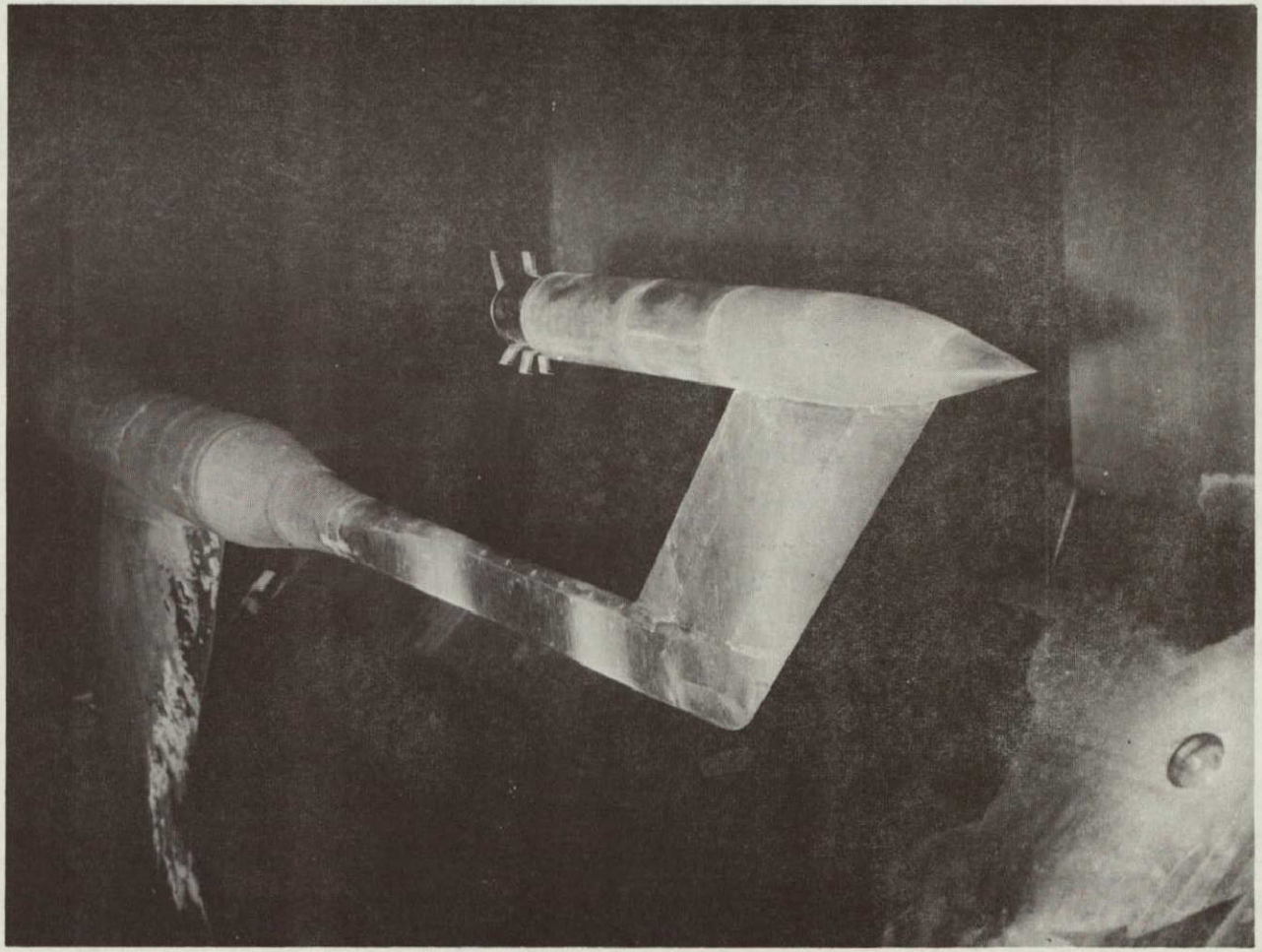

Figure 1.- Photograph of model installed in the tunnel. (Boundary layer rakes installed, forward rake configuration).

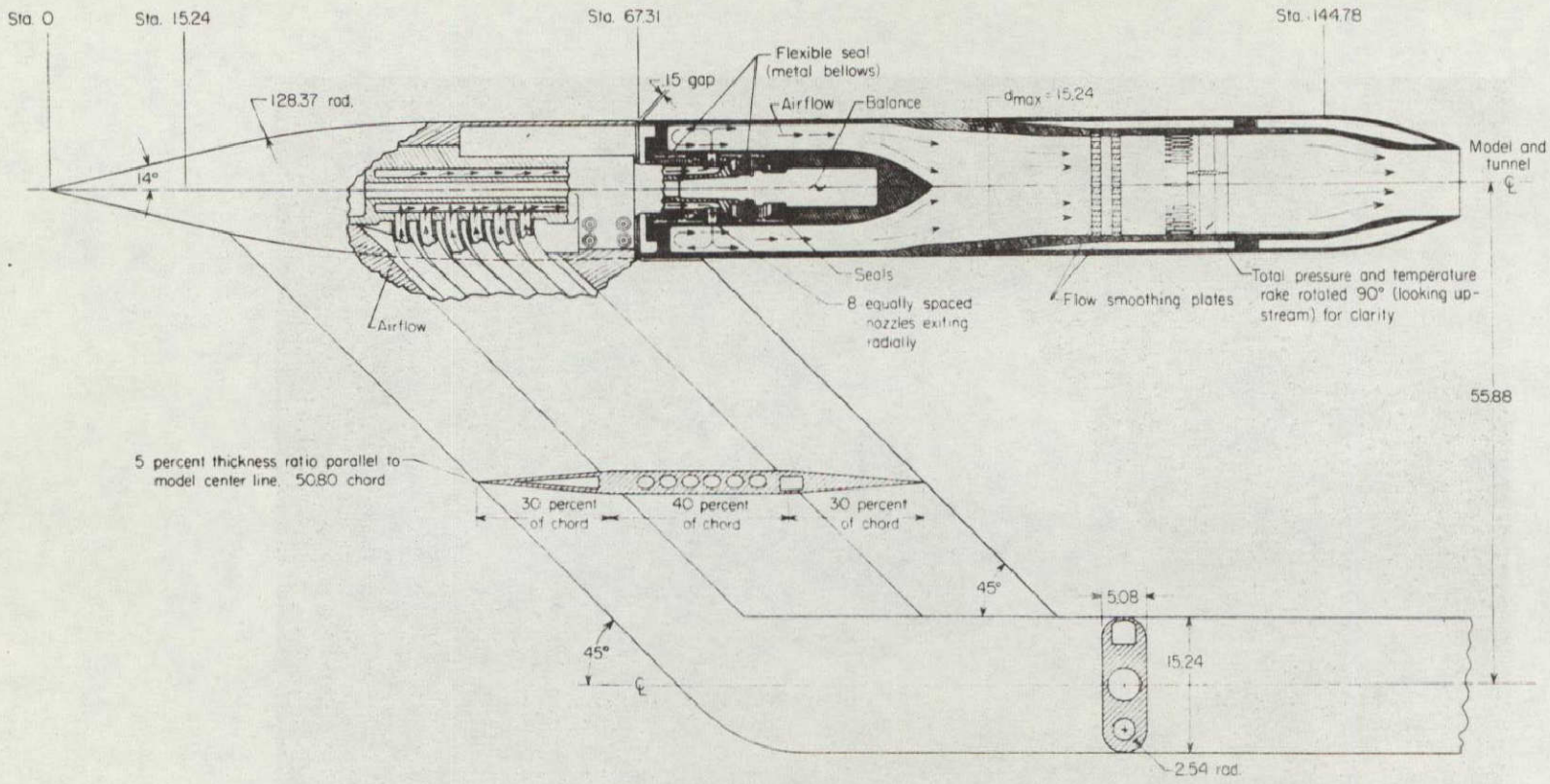

(a) Air Model

Figure 2.- Sketch showing general arrangement of the model. (All dimensions are in centimeters unless otherwise noted).

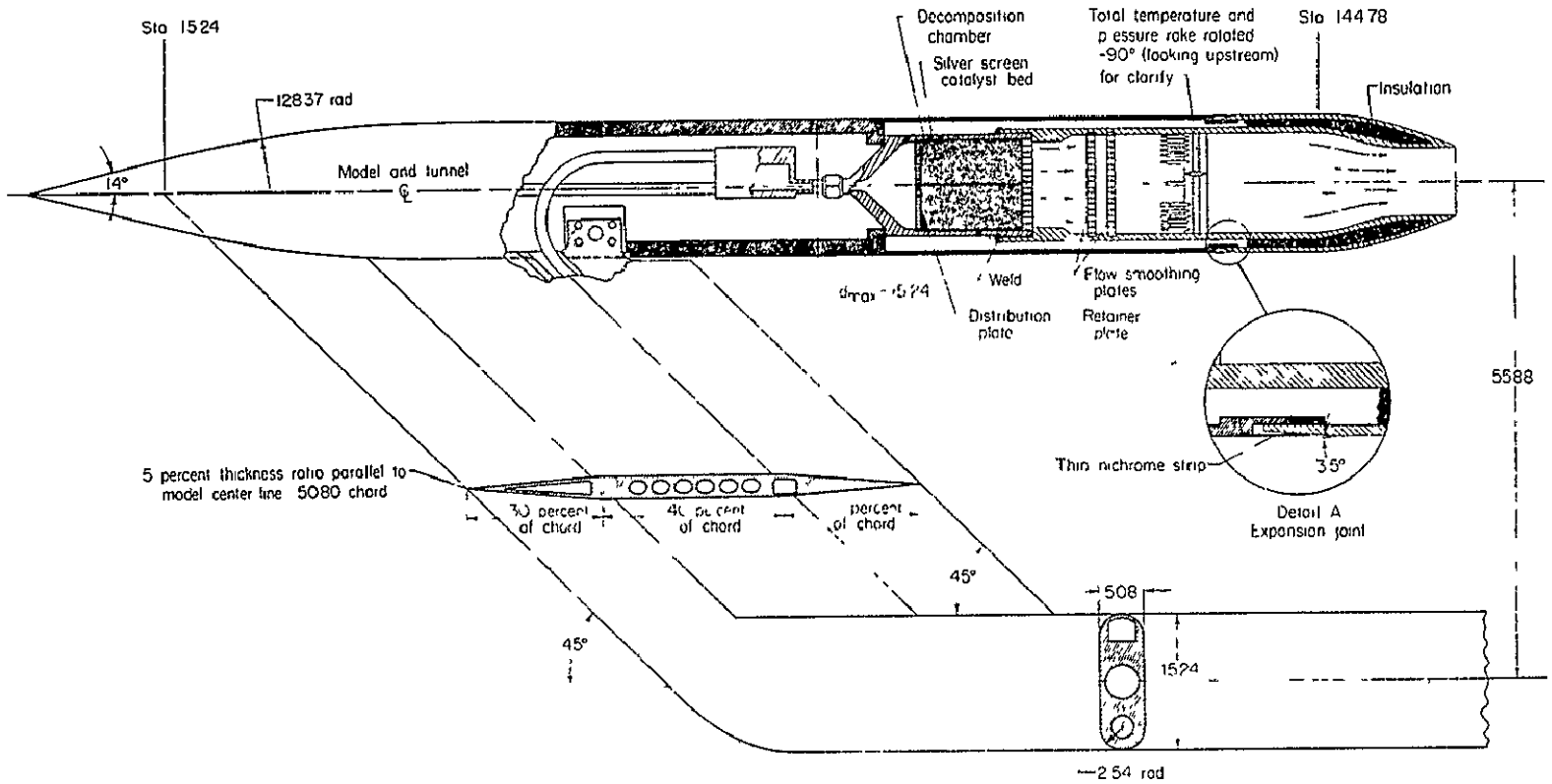

(b) Hydrogen peroxide model.

Figure 2.- Concluded.

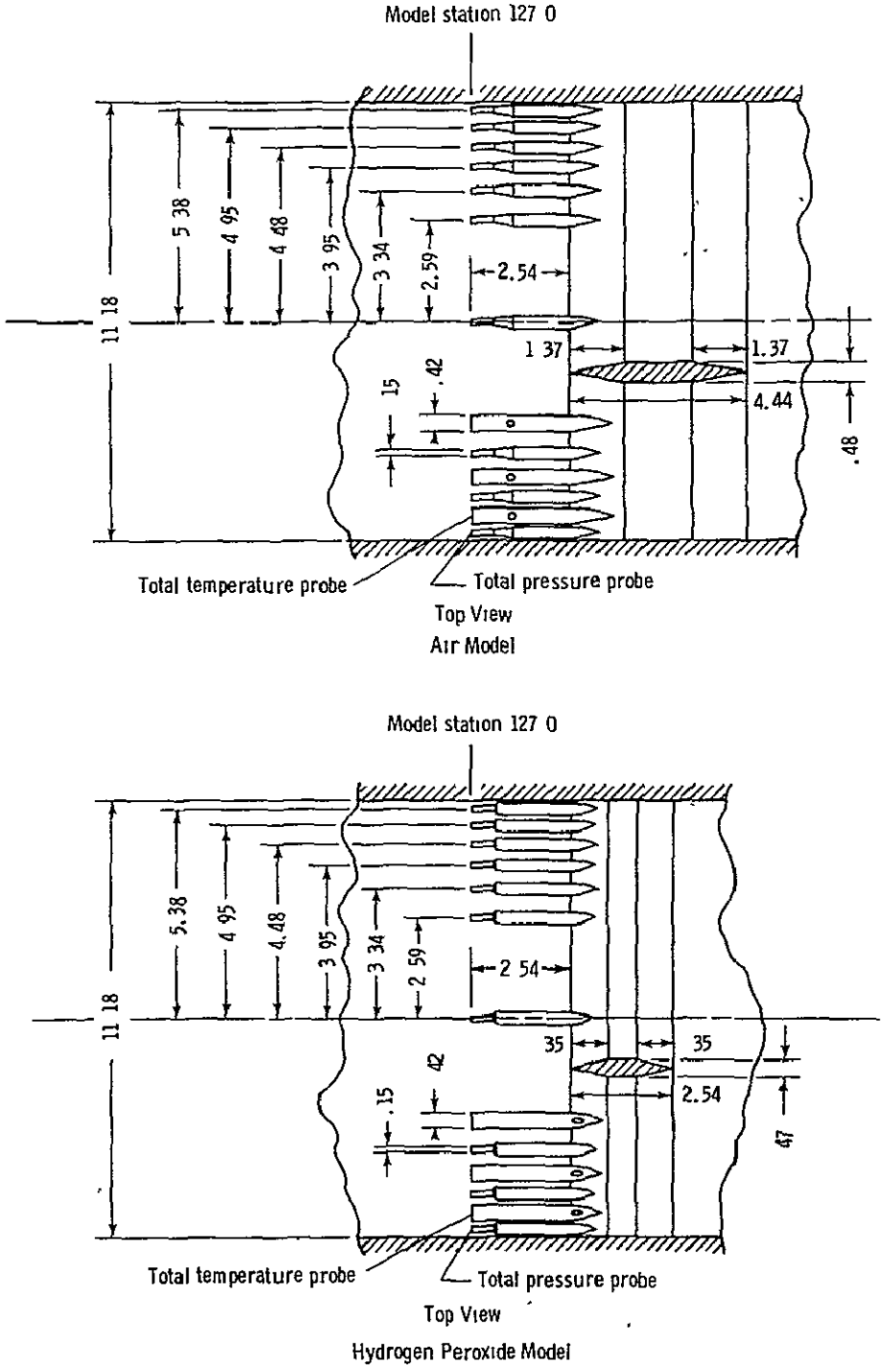

Figure 3.- Details of internal flow rakes. (All dimensions are in centimeters unless otherwise noted).

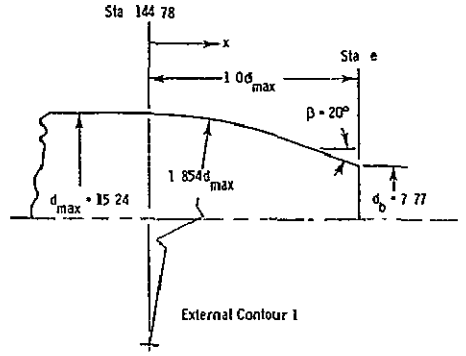

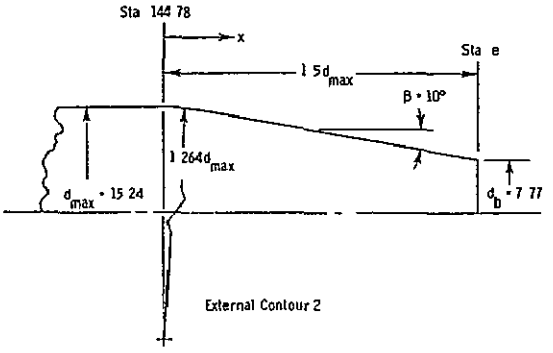

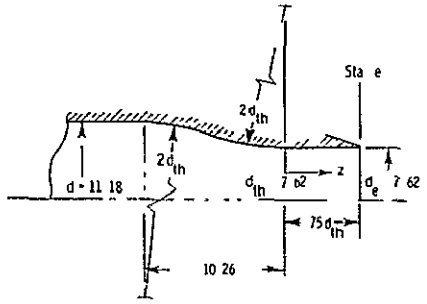

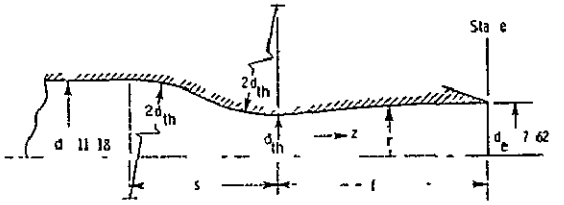

Internal Contour 2
tone for γ = 1 4 and one for γ 1 283)

Configuration	Design Parameters						
	External contour	Internal contour	β	M_e	d_{th}	s	f
1	1	1	20°	SONIC		-	
2	2	1	10°	SONIC		-	
3a	1	2a(γ = 1 4)	20°	2	5 87	10 84	15 06
3b	1	2b(γ = 1 283)	20°	2	5 70	10.83	16.54
4a	2	2a(γ = 1 4)	10°	2	5 87	10 84	15 06
4b	2	2b(γ = 1 283)	10°	2	5 70	10.83	16 54

Coordinates for Supersonic Nozzles							
Nozzle a(γ = 1 4)		Nozzle b(γ 1 283)		Nozzle a(γ 1 4)		Nozzle b(γ = 1 283)	
z	r	z	r	z	r	z	r
0	2.934	0	2 847	7 699	3 602	7 584	3 439
0 455	2 957	0.307	2 850	8.148	3 630	8 110	3 485
0 566	2.964	0 493	2 850	8 626	3 655	8 677	3 531
1 034	3 000	0.998	2 855	9 124	3.680	9 154	3 564
1 544	3 043	1 516	2.873	9 652	3.706	9 662	3.599
2.037	3 089	2.009	2 901	10.201	3 729	10.193	3 632
2 550	3 139	2.588	2.946	10 630	3.744	10.612	3 655
3 071	3.193	3.033	2.884	11 229	3.762	11 194	3.686
3 561	3 244	3 574	3 035	11 692	3 774	11 646	3 708
4 087	3 299	4 054	3 081	12.154	3 785	12.121	3 726
4 567	3 348	4 580	3 137	12.865	3 797	12.774	3 752
5 052	3 393	5 103	3 193	13 604	3 805	13 627	3 774
5 591	3 442	5 568	3 241	14 348	3.810	14 364	3 790
6 104	3.485	6 144	3 302	15 062	3 810	15 110	3 802
6 563	3 520	6 639	3 350			15 839	3.807
7 160	3 563	7 097	3 396			16 543	3.810

Figure 4.- Geometry and dimensions of the various configurations. (All dimensions are in centimeters unless otherwise noted).

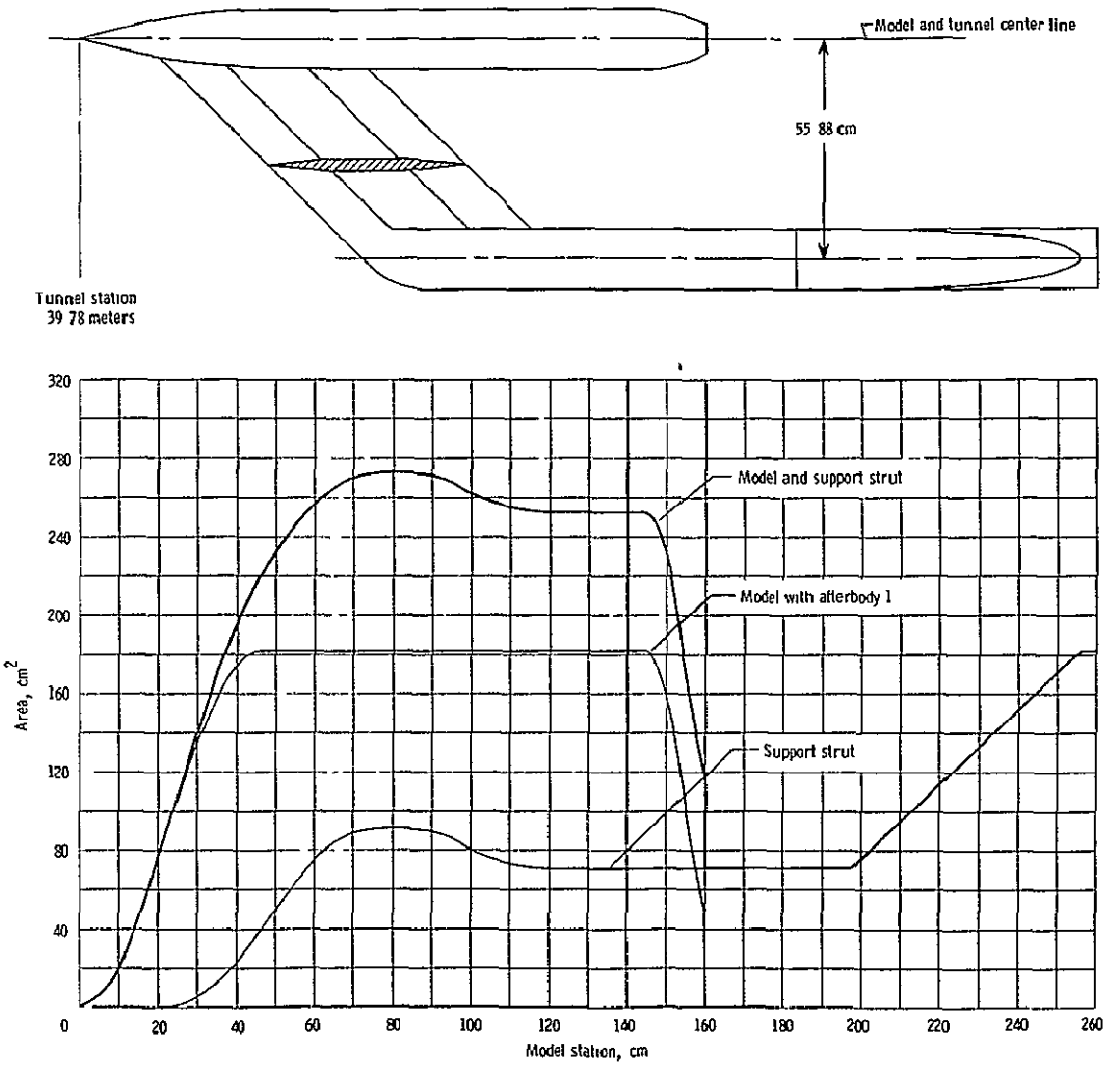

Figure 5.- Cross-sectional area distributions of the model and support system.

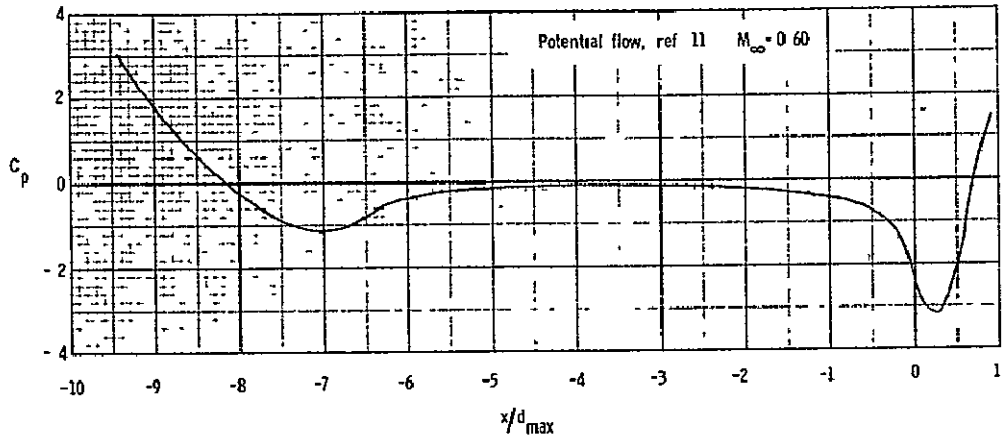

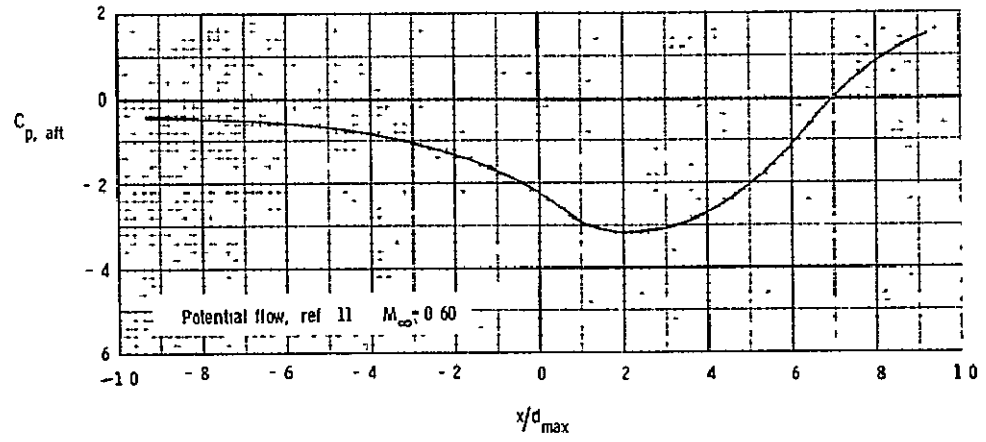

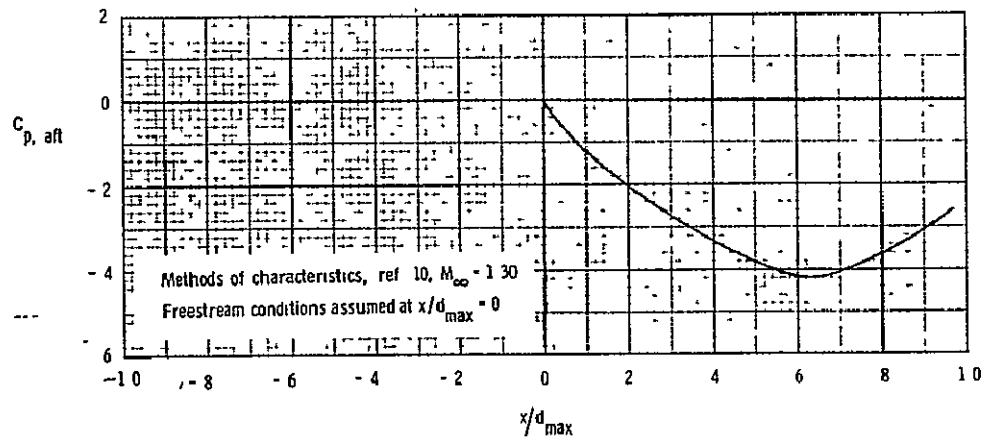

Figure 6.- Examples of theoretical pressure coefficient distributions on the model. ($\beta = 20^\circ$, $\ell/d_{max} = 1.0$).

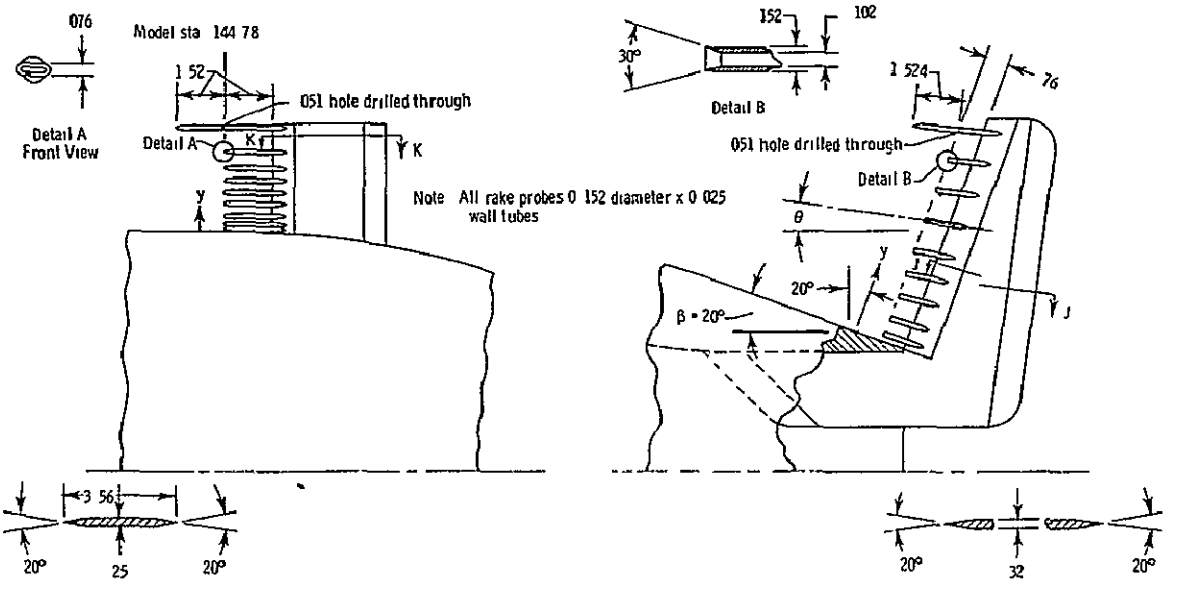

Note Φ measured clockwise when the model is viewed from the rear 0° is at the top of the model

* Boundary layer temperatures were measured at these values of y for the rakes located at angles Φ = 0° and 180°

Forward Rakes	
Rake probe locations	
Probe	y
1	0 08
2	25*
3	51*
4	89*
5	1 27*
6	1 65
7	2.03*
8	2.54
9 (Static probe)	3.30*

NOTE Forward rakes located at angles of Φ = 0° 135° 157 5°, AND 180°

Trailing Edge Rakes		
Rake probe locations		
Probe	y	θ deg
1	0.25	19 3
2	76	16 8*
3	1 52	14 0*
4	2.29	11 8*
5	3 05	10.1*
6	4 06	8 3*
7	5 08	7 0
8	6.10	5 9*
9 (Static Probe)	7 11	5 1

Note- Rear rake located at $\phi = 0^{\circ}$

Figure 7.- Sketch of the boundary layer rakes. (All dimensions are in centimeters unless otherwise noted).

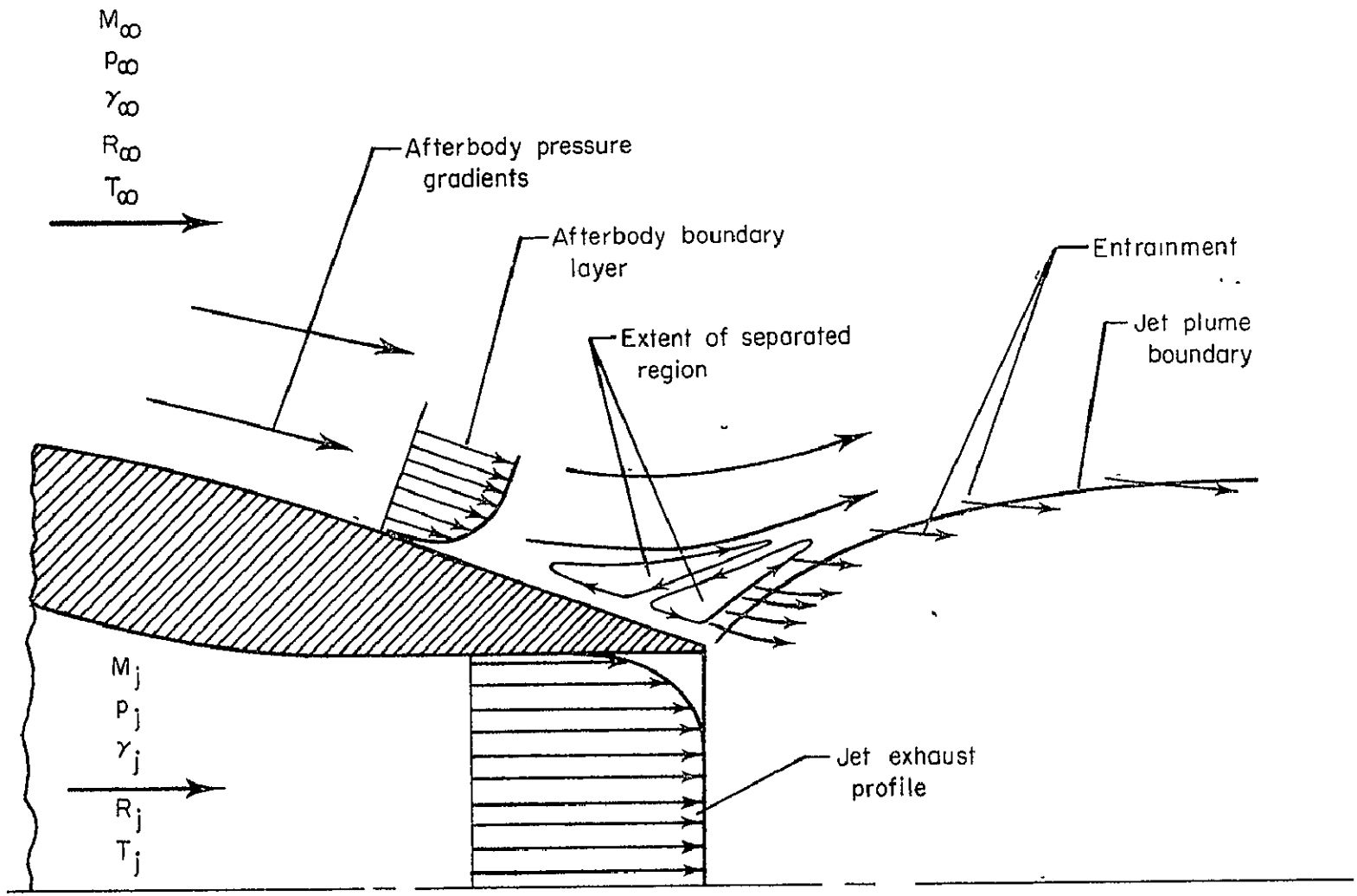

Figure 8.- Illustration of factors influencing jet interference.

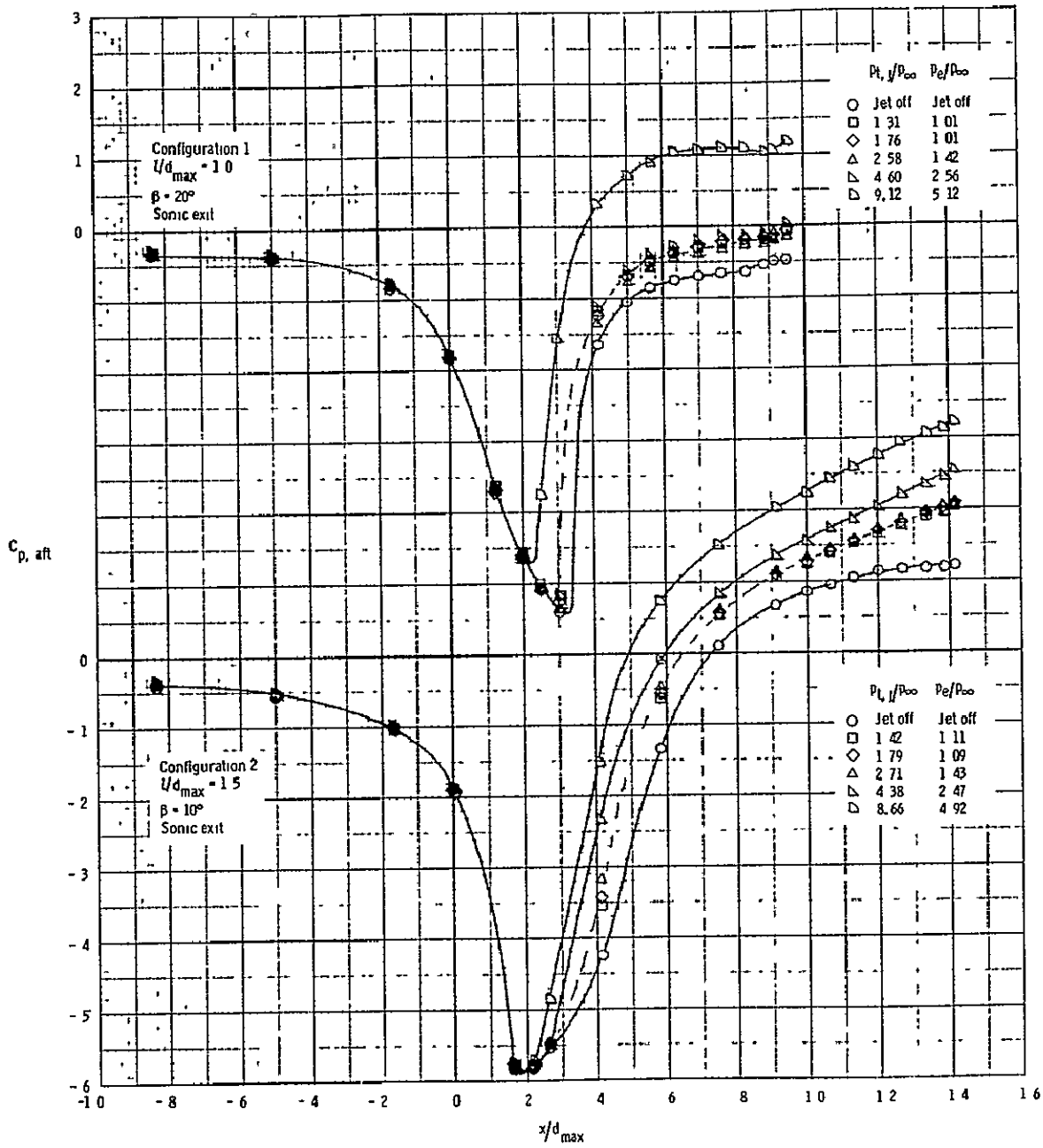

Figure 9.- Examples of jet interference on the afterbody pressure coefficients ($\beta = 20^\circ$, $l/d_{max} = 1.0$, sonic exit, $\gamma_j = 1.28$, $R_j = 384$ joules/kg K. $T_{t,j} = 810$K, $M_\infty = 0.95$).

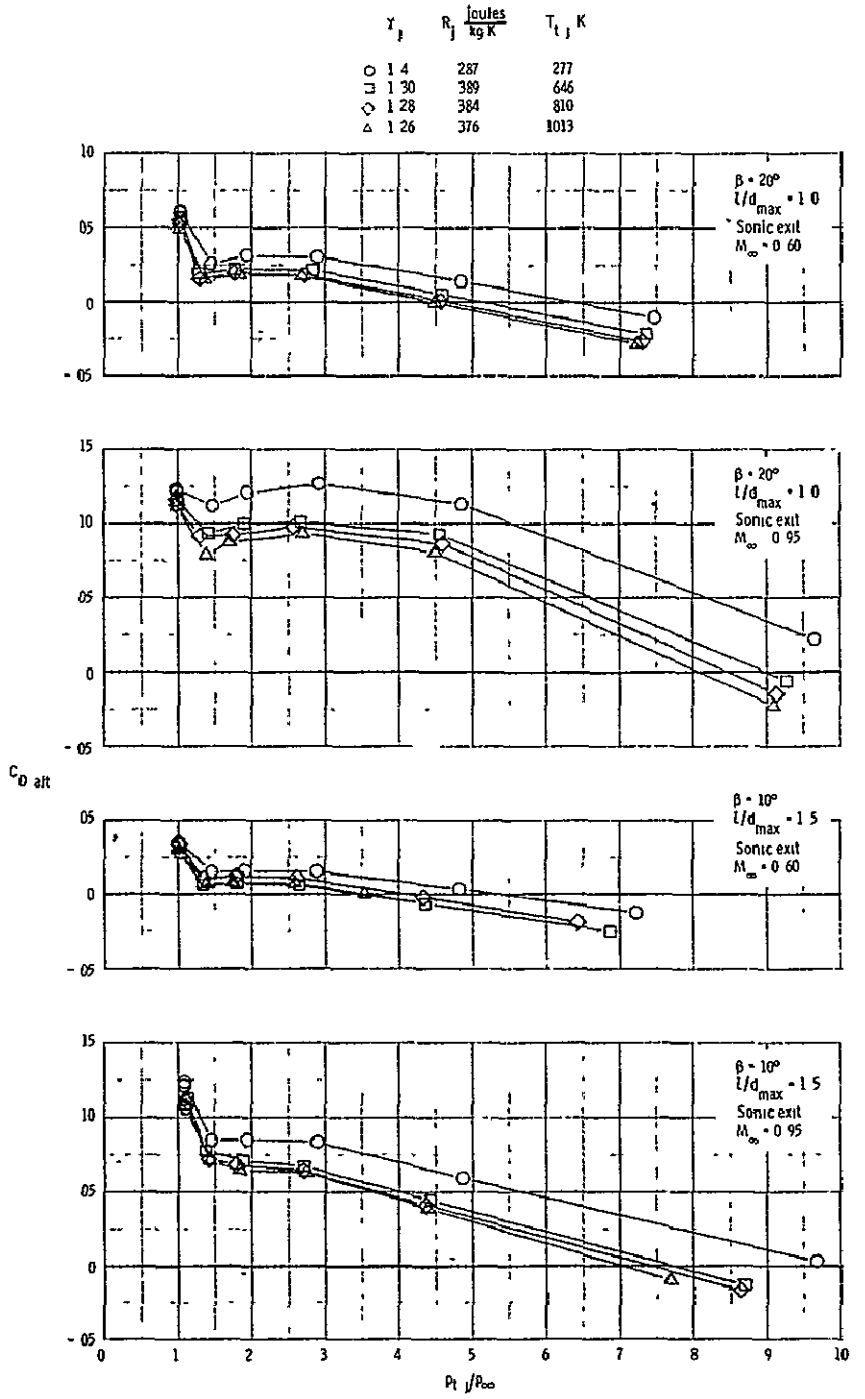

Figure 10.- Examples of afterbody drag coefficient as a function of jet total pressure ratio for the various jet exhaust gases.

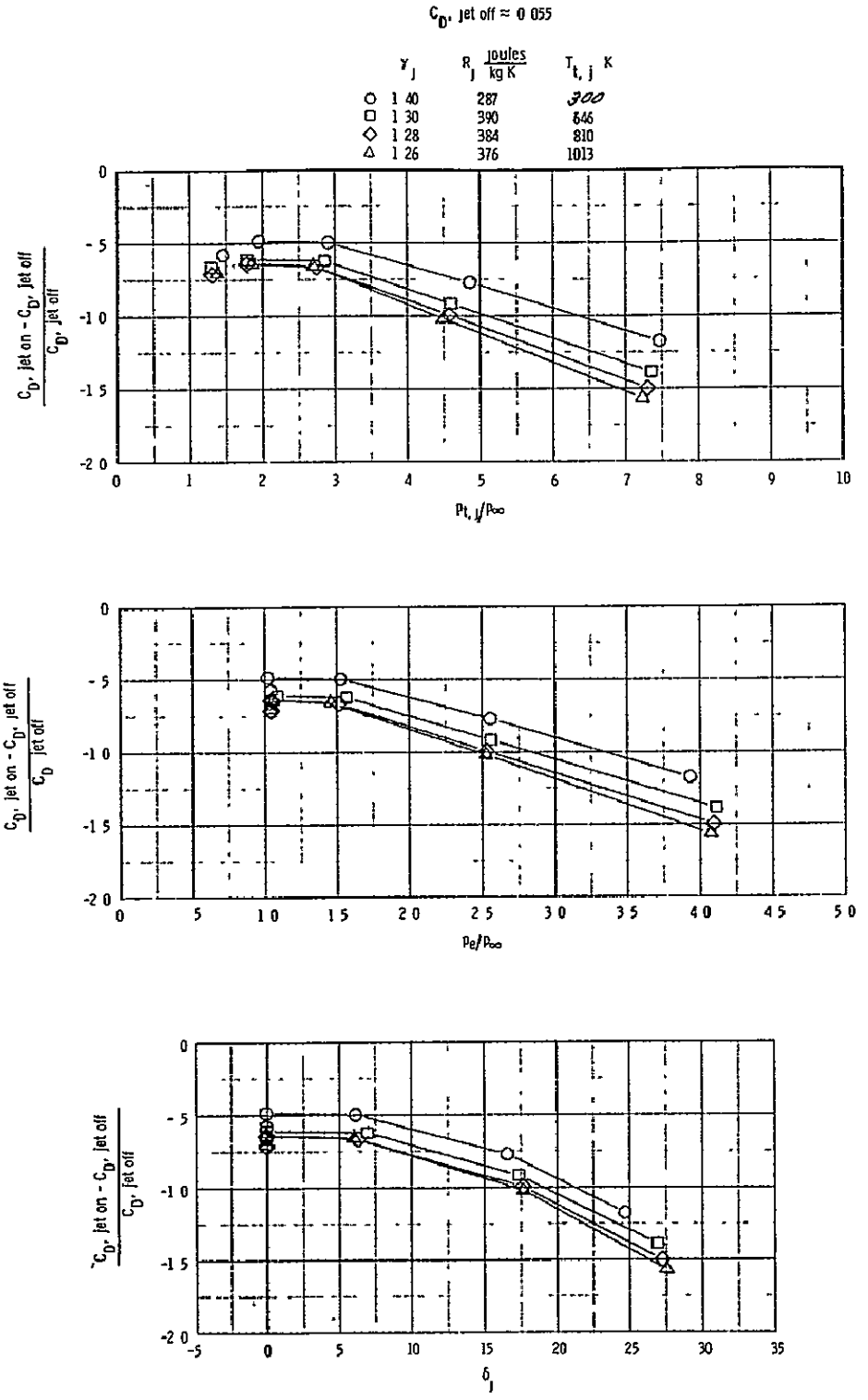

(a) $M_\infty = 0.60$.

Figure 11.- Incremental afterbody drag coefficient as a function of $P_{t,j}/p_\infty$, p_e/p_∞ and δ_j. ($\beta = 20^o$, $\ell/d_{max} = 1.0$, sonic exit).

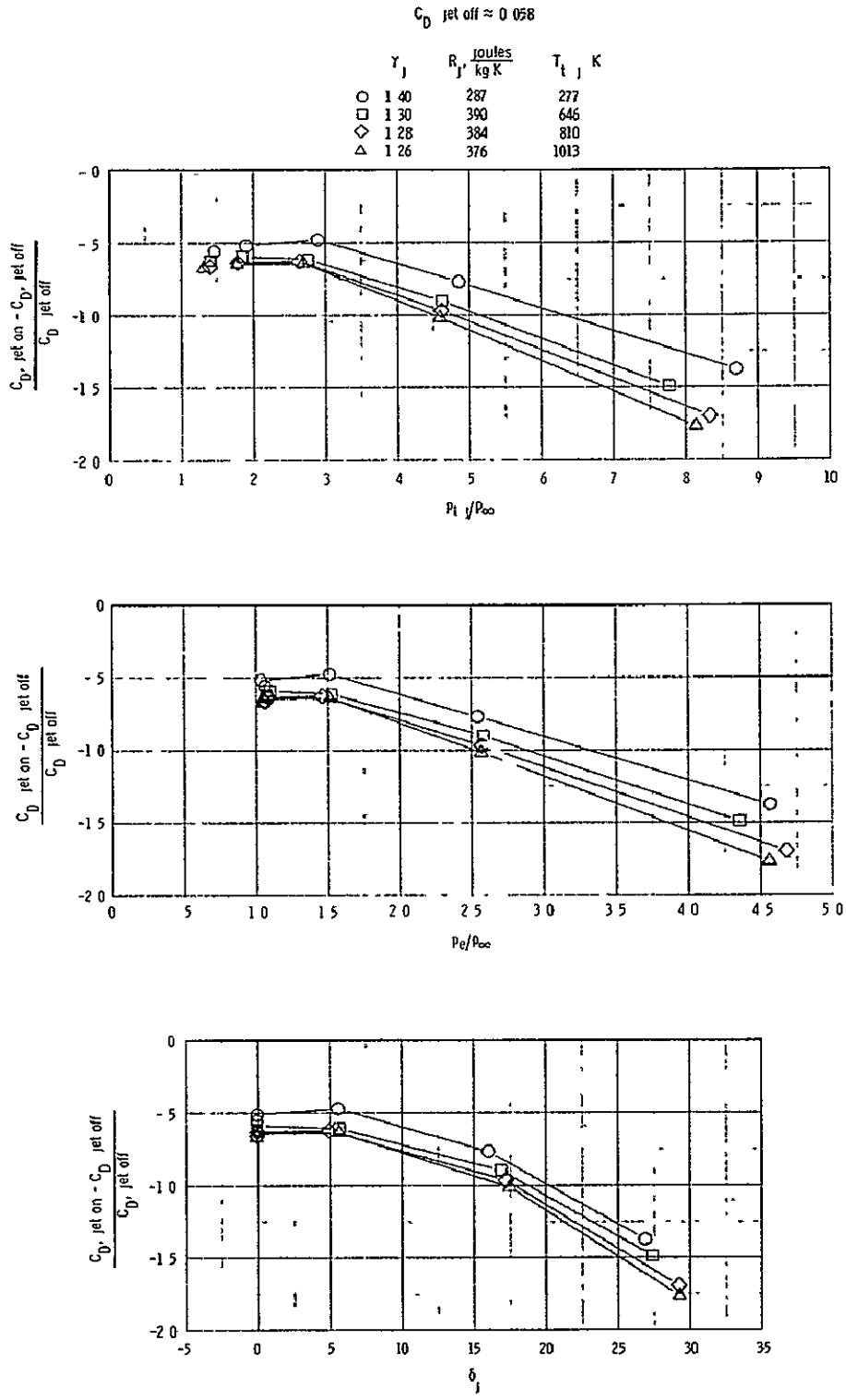

(b) $M_\infty = 0.80$.

Figure 11.- Continued.

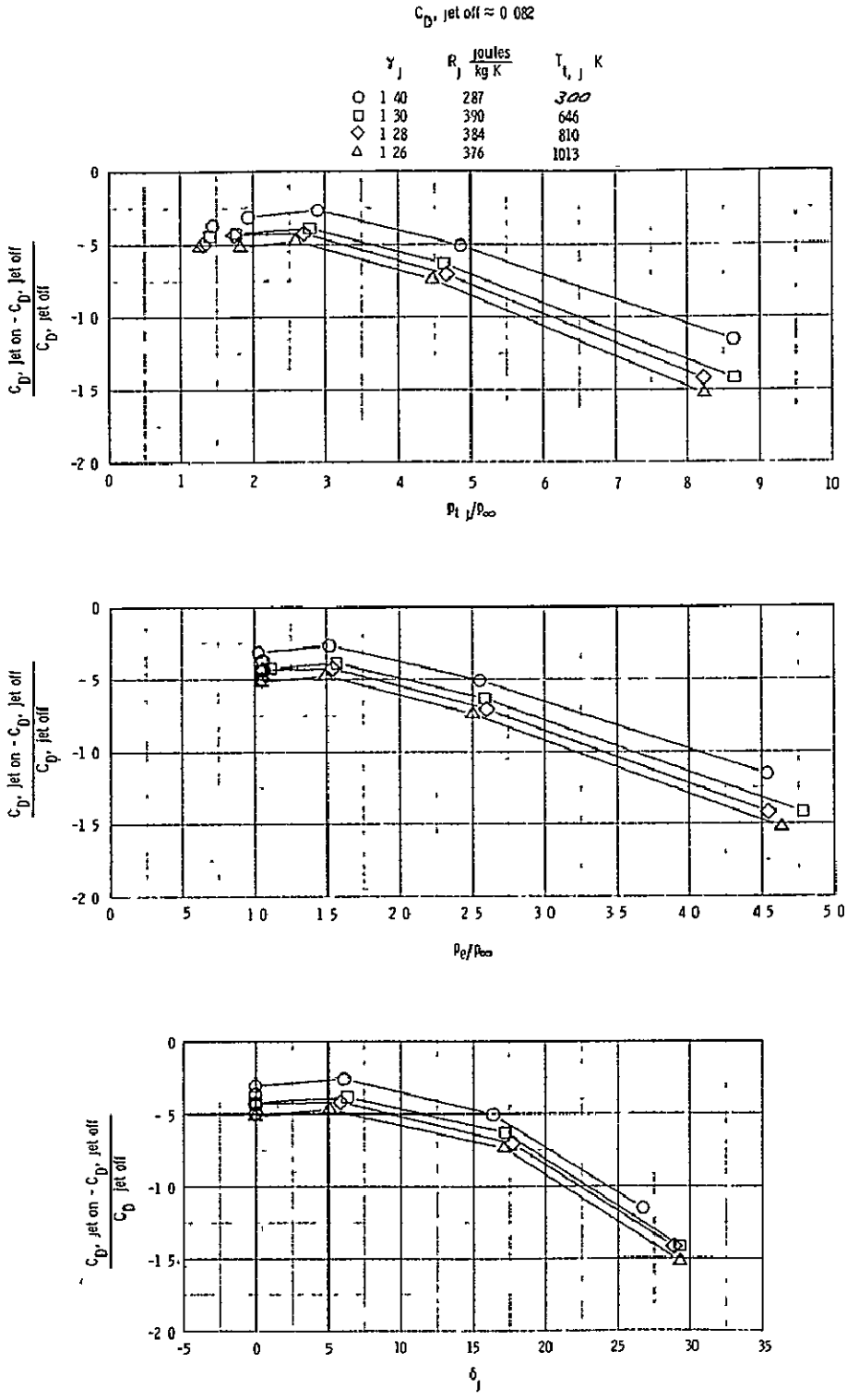

(c) $M_\infty = 0.90$.

Figure 11.- Continued.

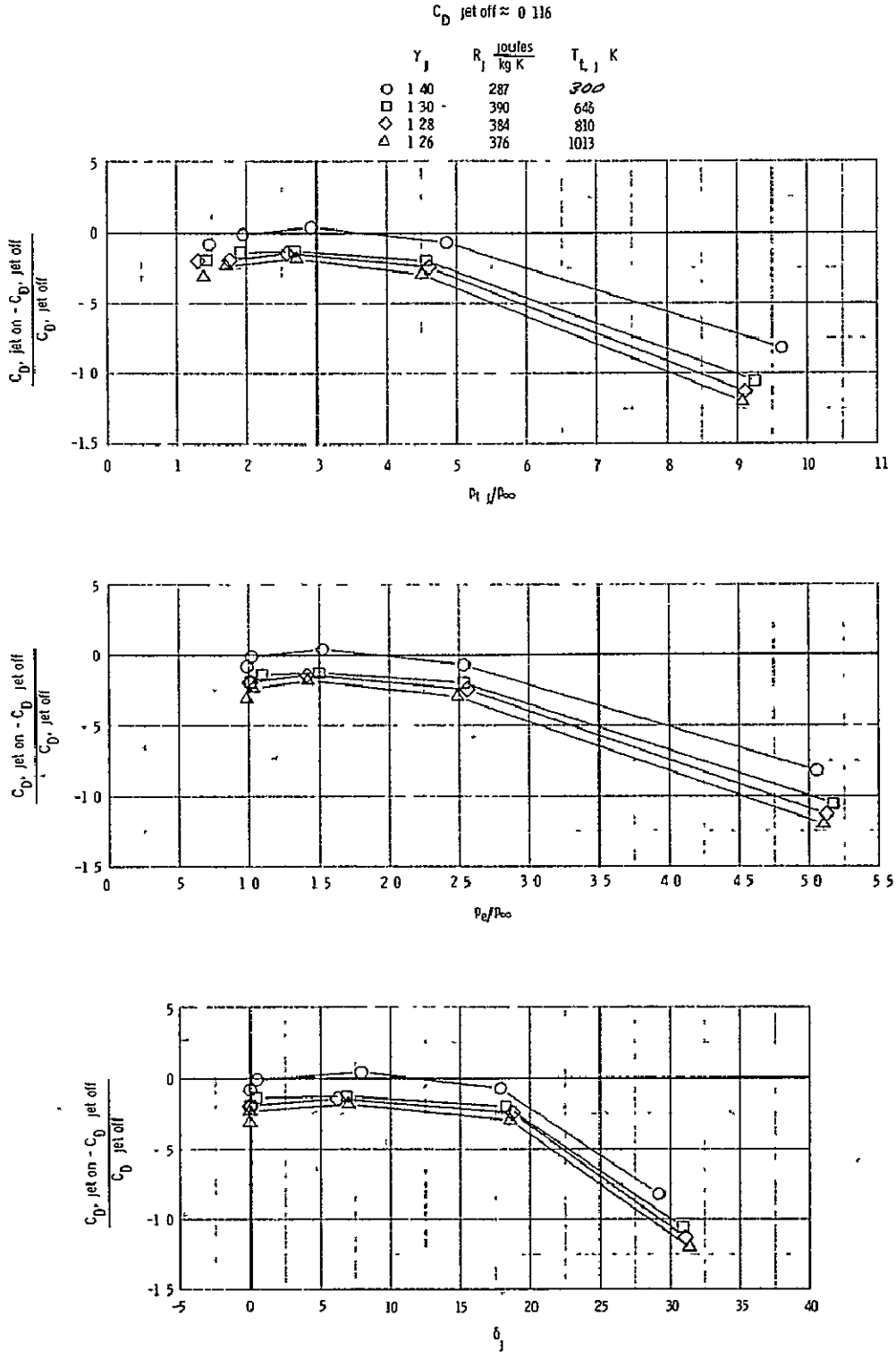

(d) $M_\infty = 0.95$.

Figure 11.- Continued.

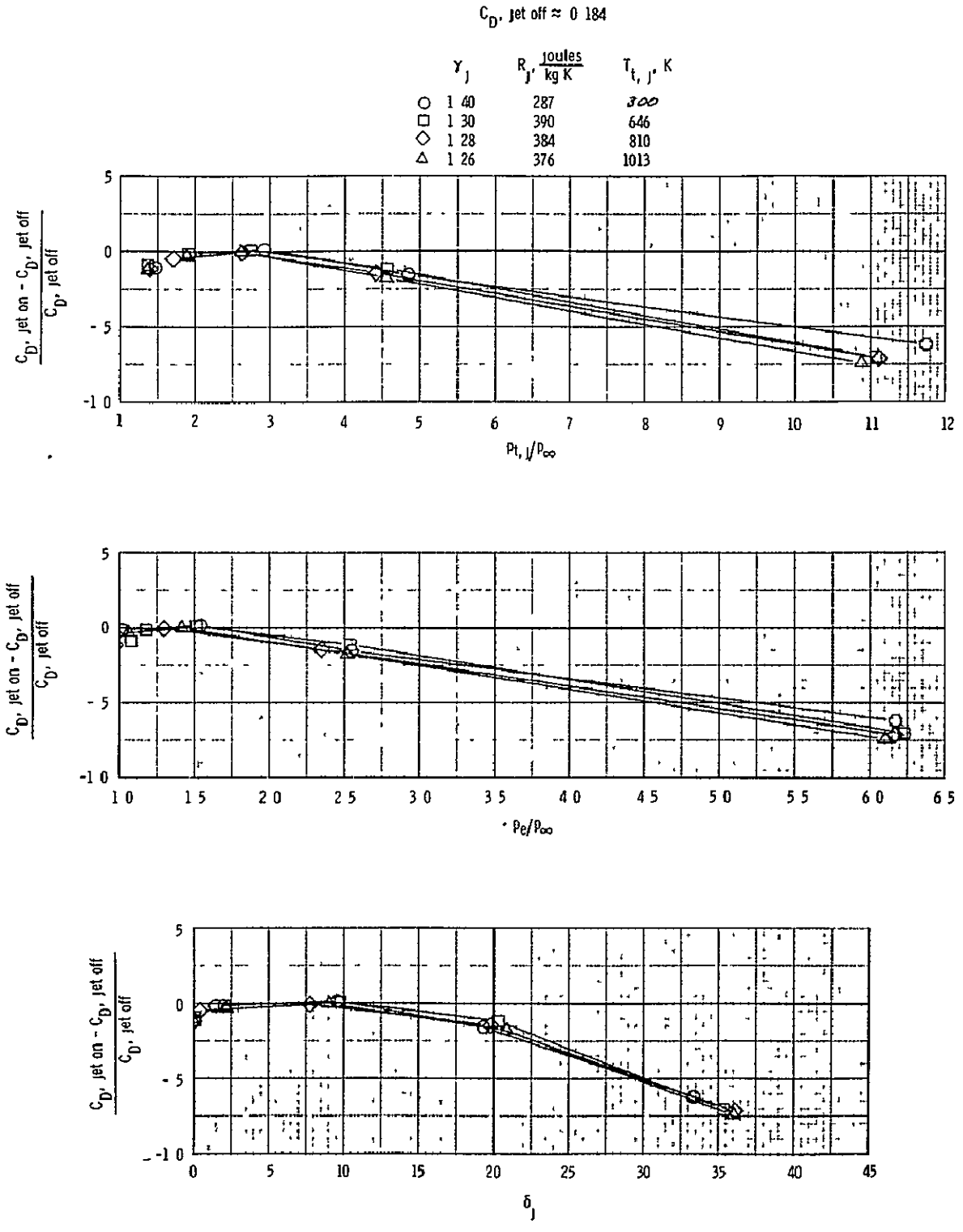

(e) $M_\infty = 1.20$.

Figure 11.- Concluded.

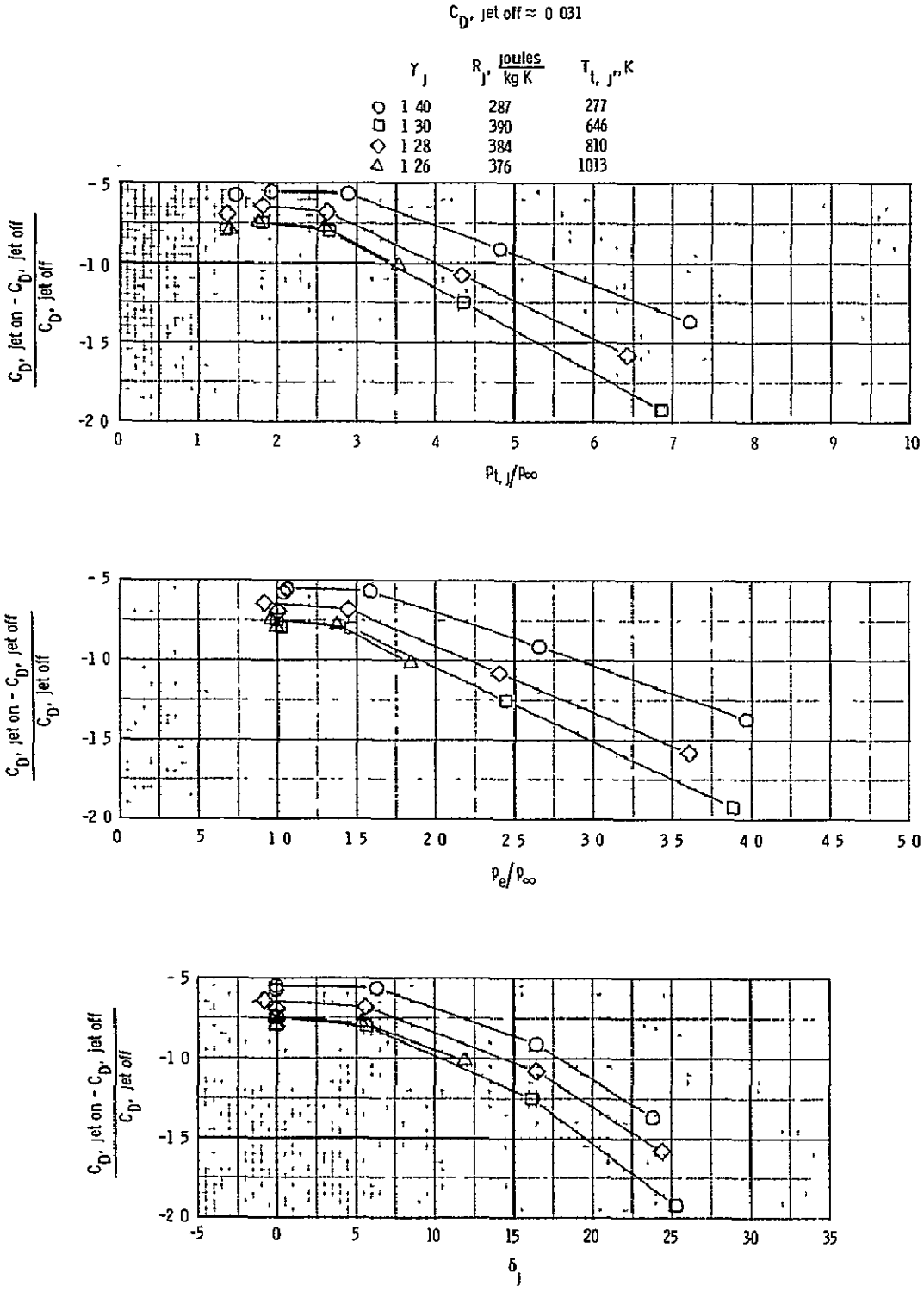

(a) $M_\infty = 0.60$.

Figure 12.- Incremental afterbody drag coefficient as a function of $p_{t,j}/p_\infty$, p_e/p_∞, and δ_j. ($\beta = 10^\circ$, $\ell/d_{max} = 1.5$, sonic exit).

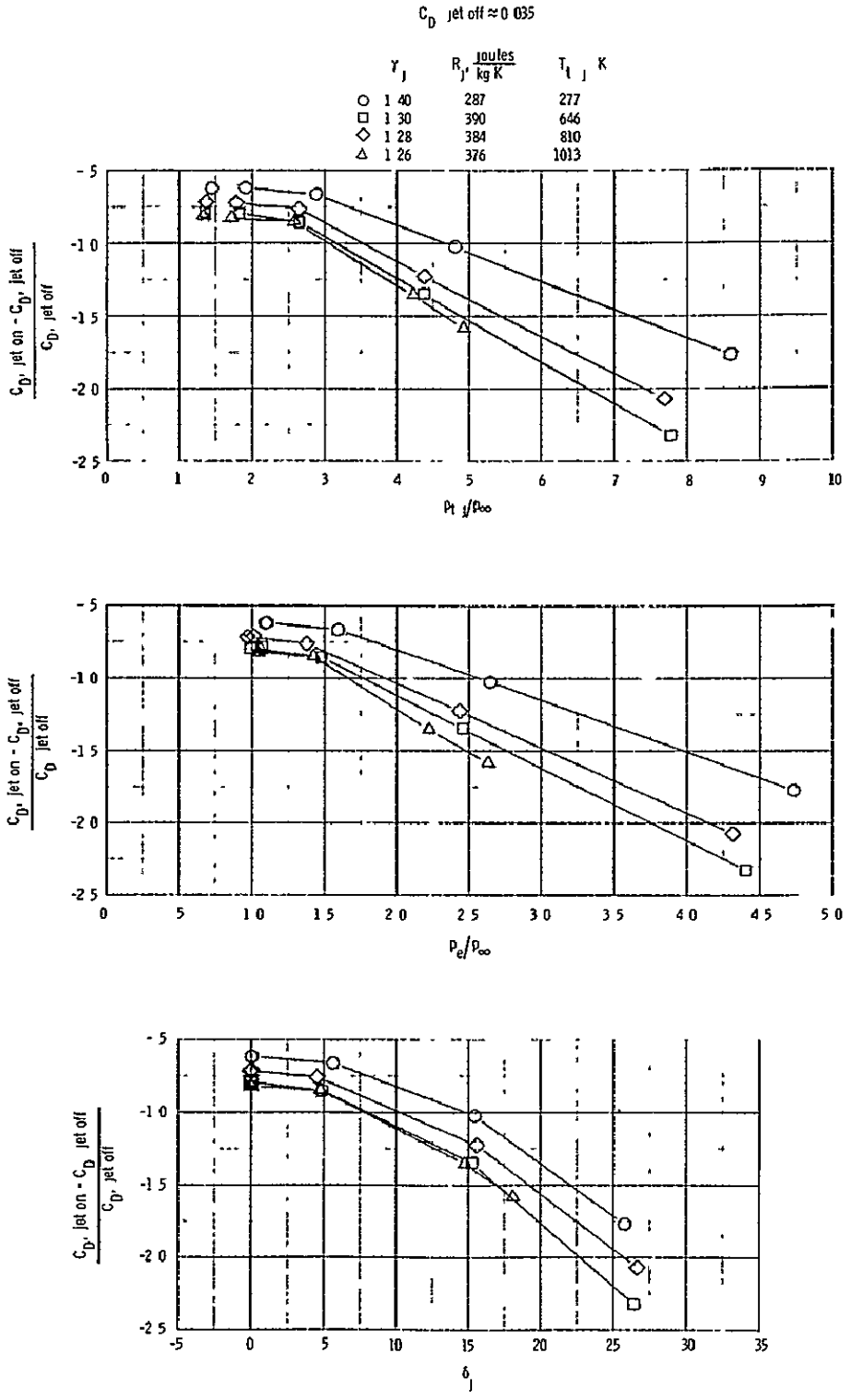

(b) $M_\infty = 0.80$.

Figure 12.- Continued.

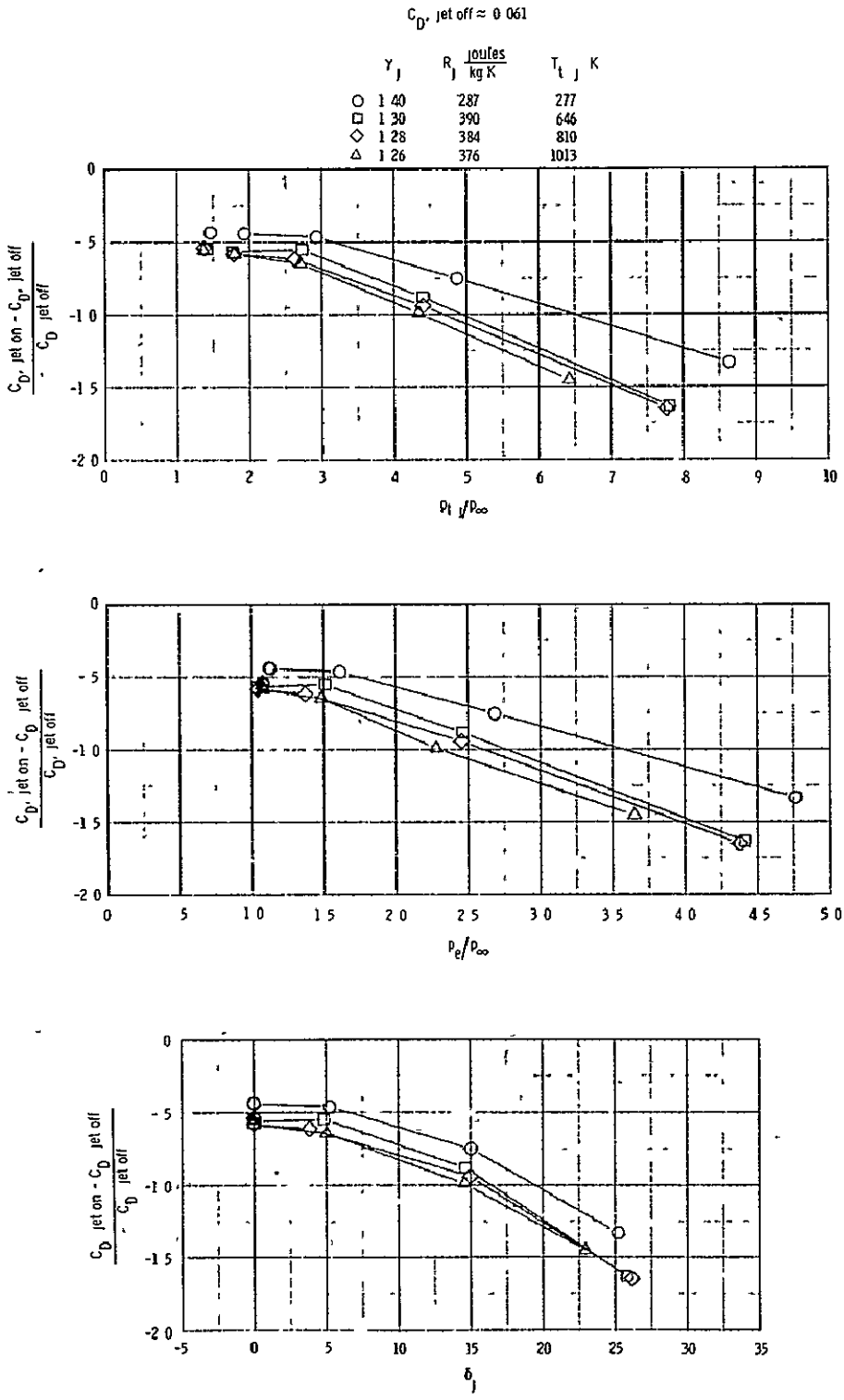

(c) $M_\infty = 0.90$.

Figure 12.- Continued.

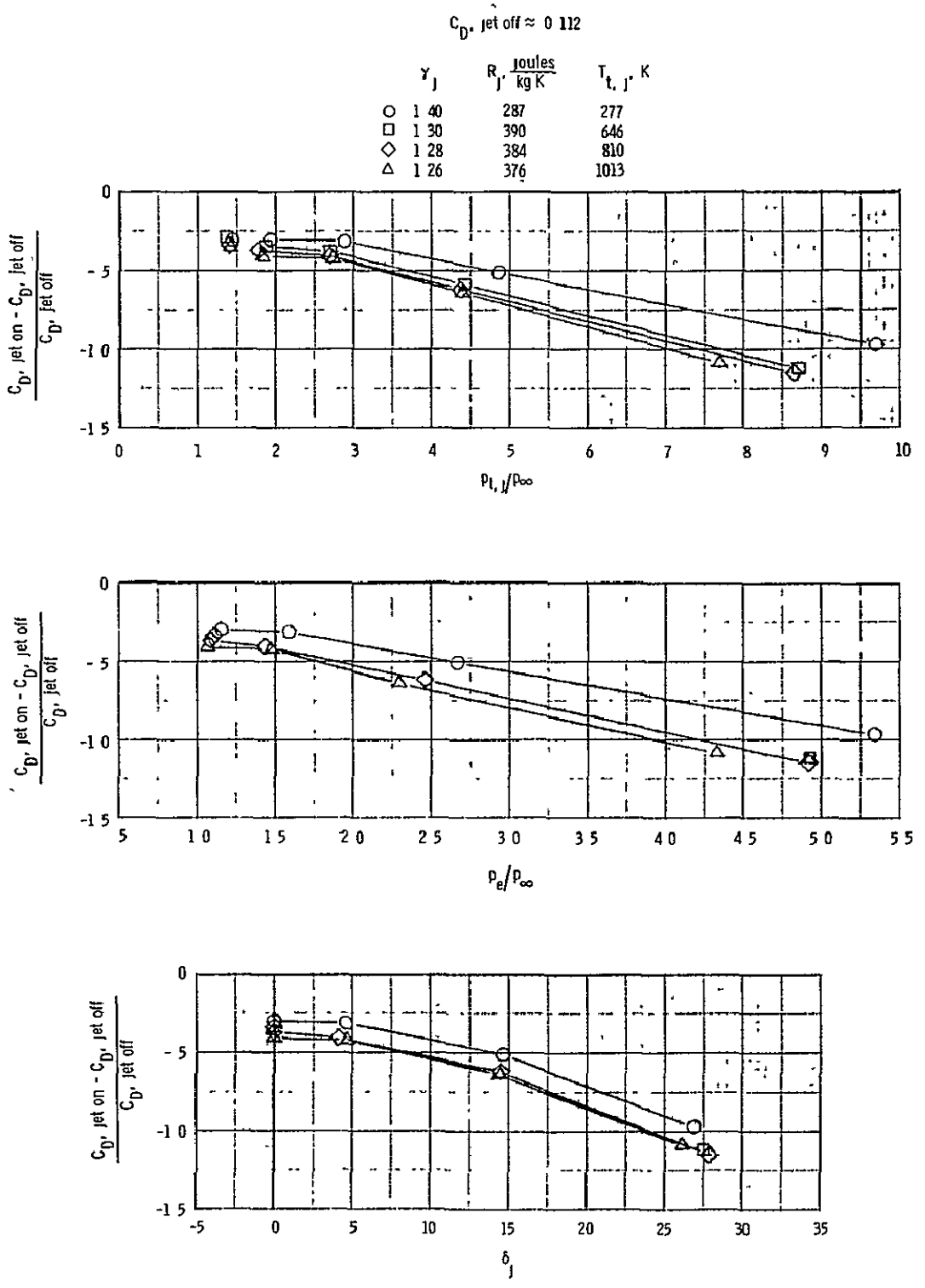

(d) $M_\infty = 0.95$.

Figure 12.- Continued.

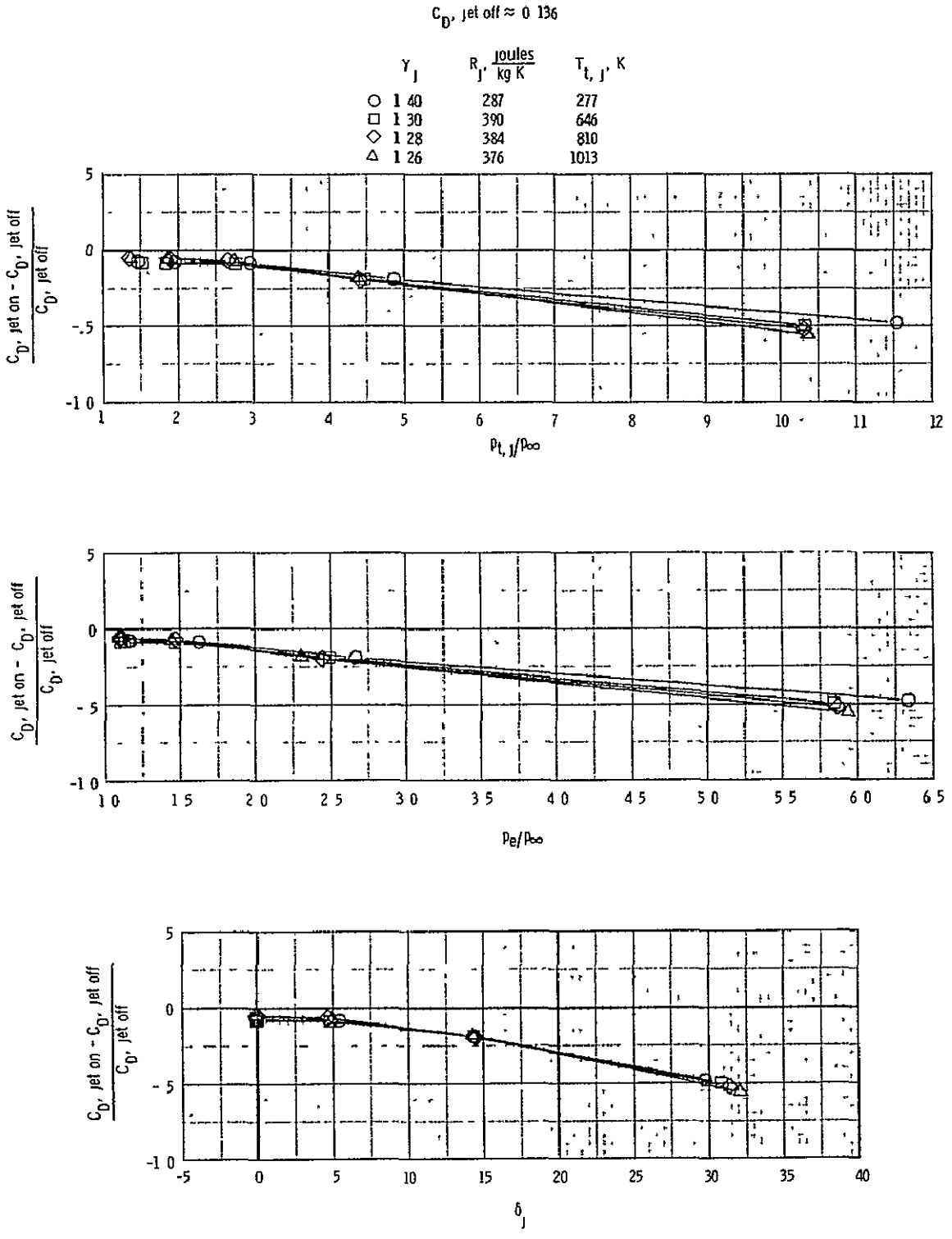

(e) $M_\infty = 1.20$.

Figure 12.- Concluded.

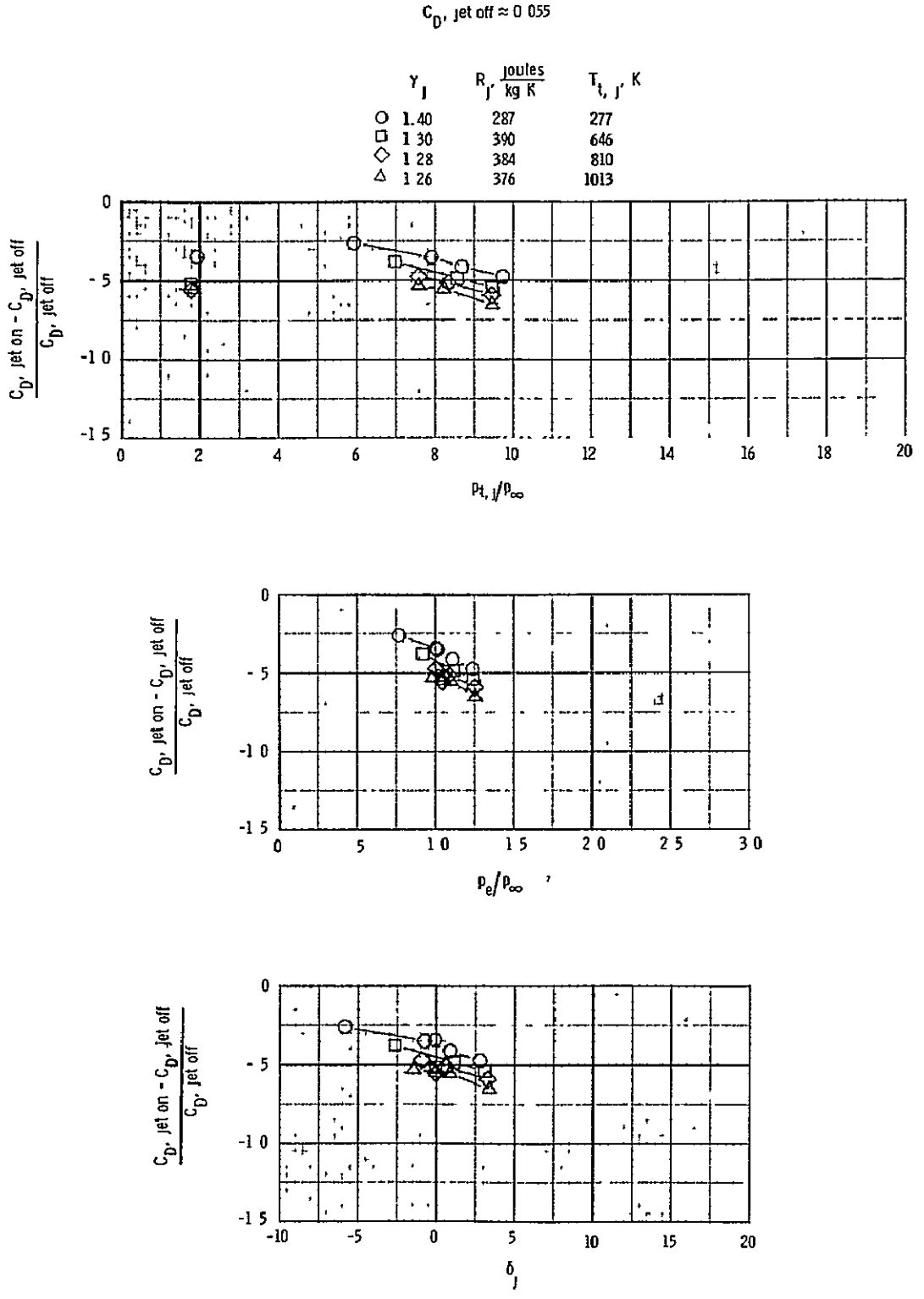

(a) $M_\infty = 0.60$.

Figure 13.- Incremental afterbody drag coefficient as a function of $p_{t,j}/p_\infty$, p_e/p_∞, and δ_j. ($\beta = 20^o$, $\ell/d_{max} = 1.0$, $M_e = 2$).

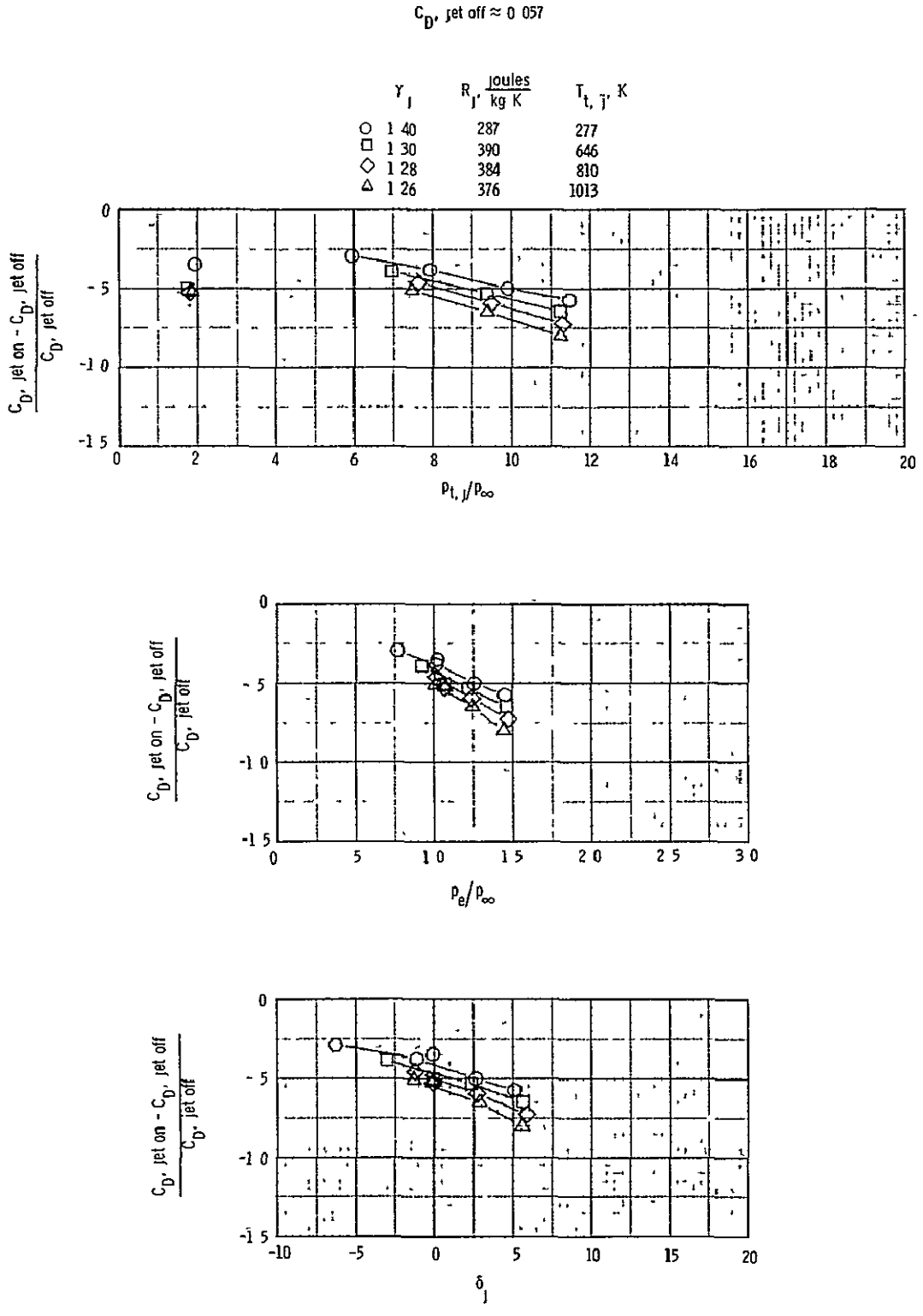

(b) $M_\infty = 0.80$.

Figure 13.- Continued.

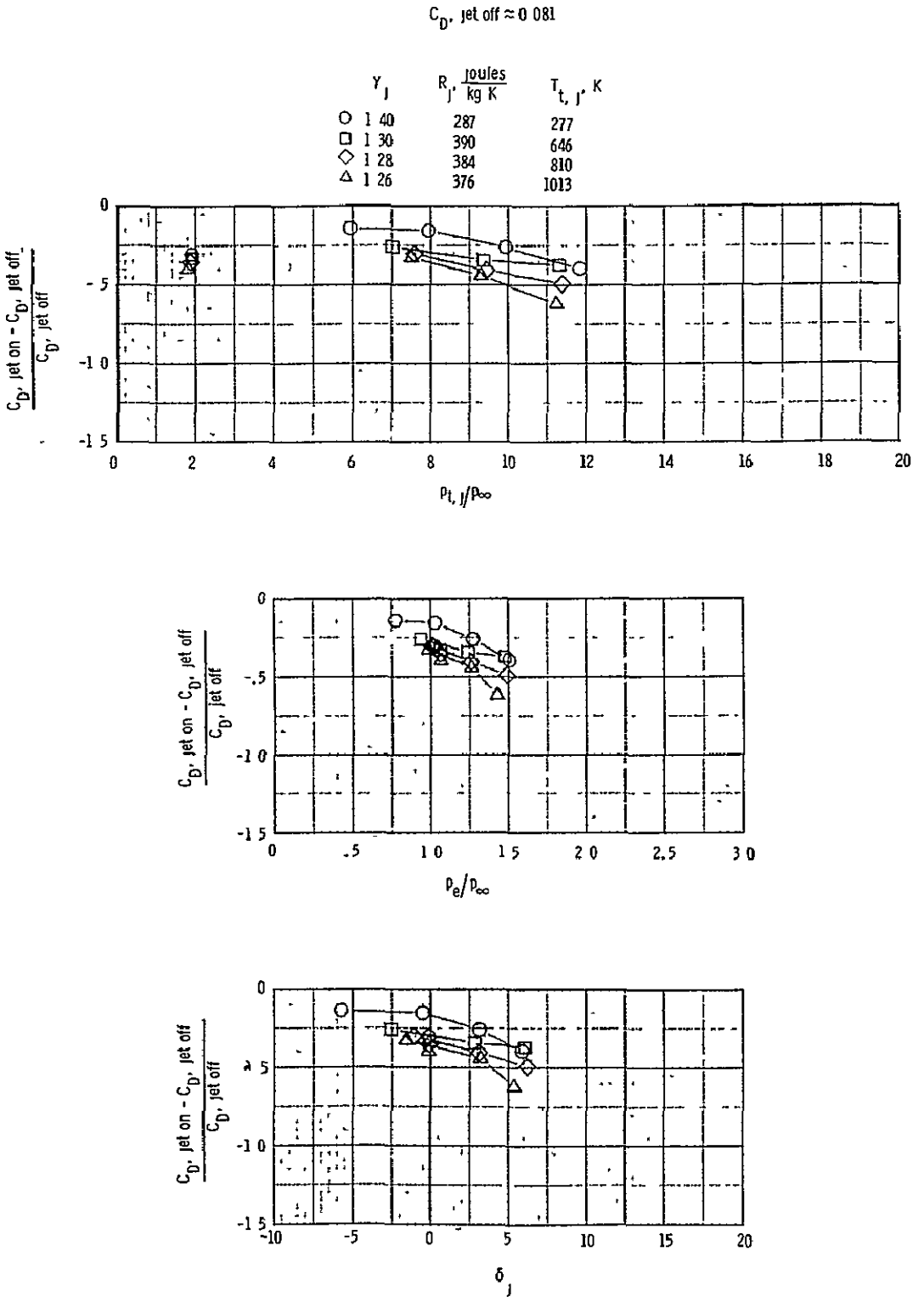

(c) $M_\infty = 0.90$.

Figure 13.– Continued.

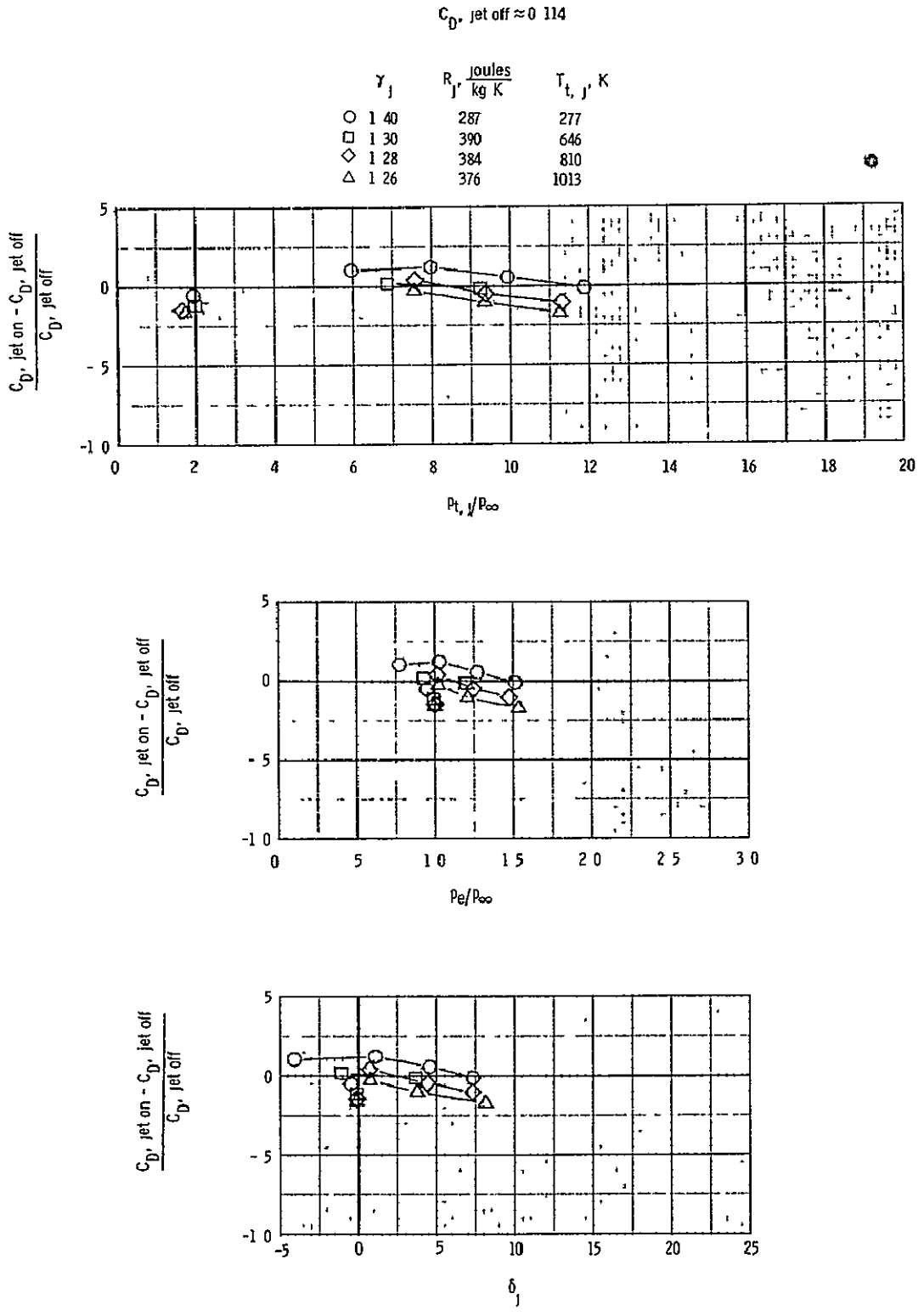

(d) $M_\infty = 0.95$.

Figure 13.- Continued.

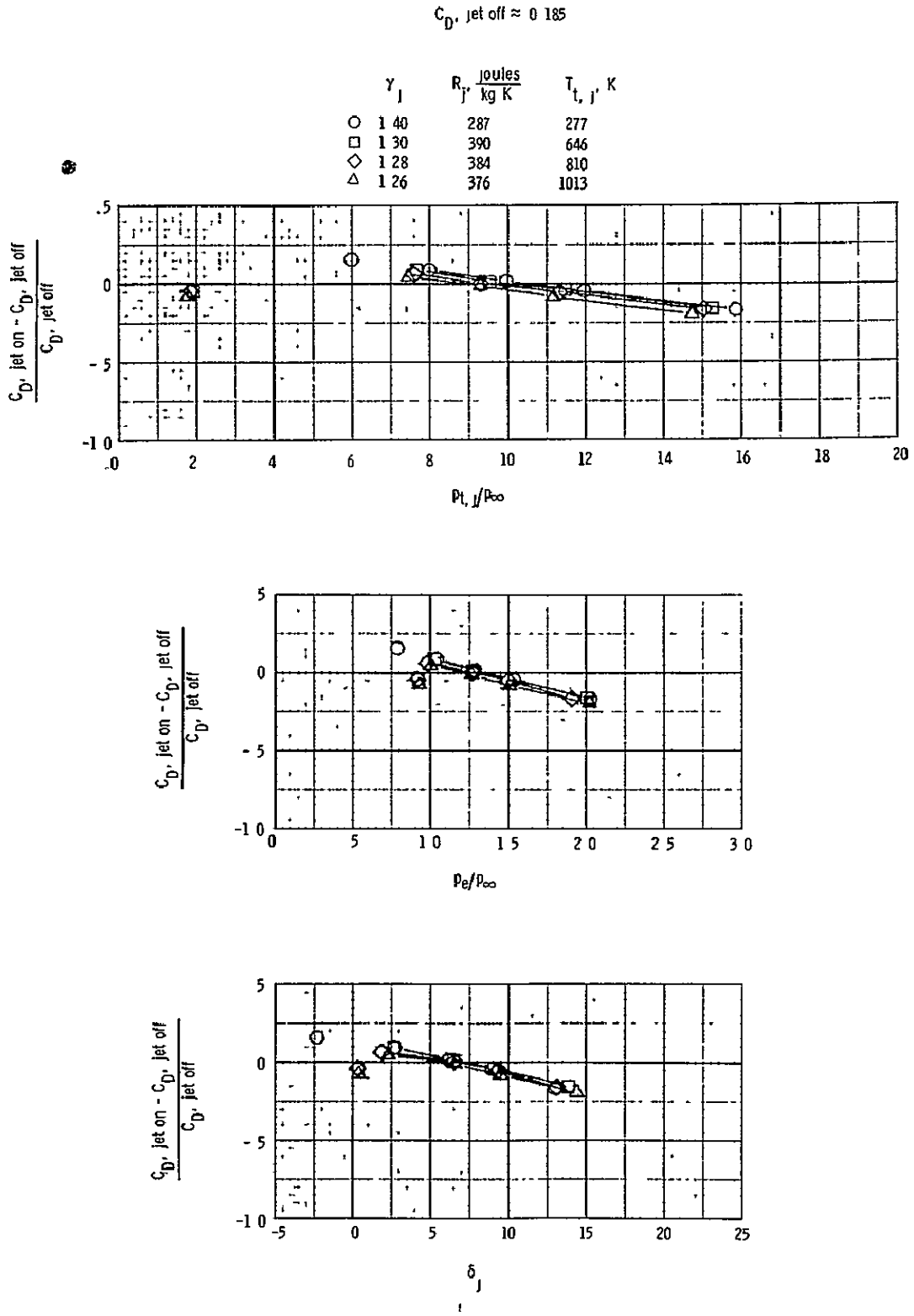

(e) M_∞ = 1.20.

Figure 13.– Concluded.

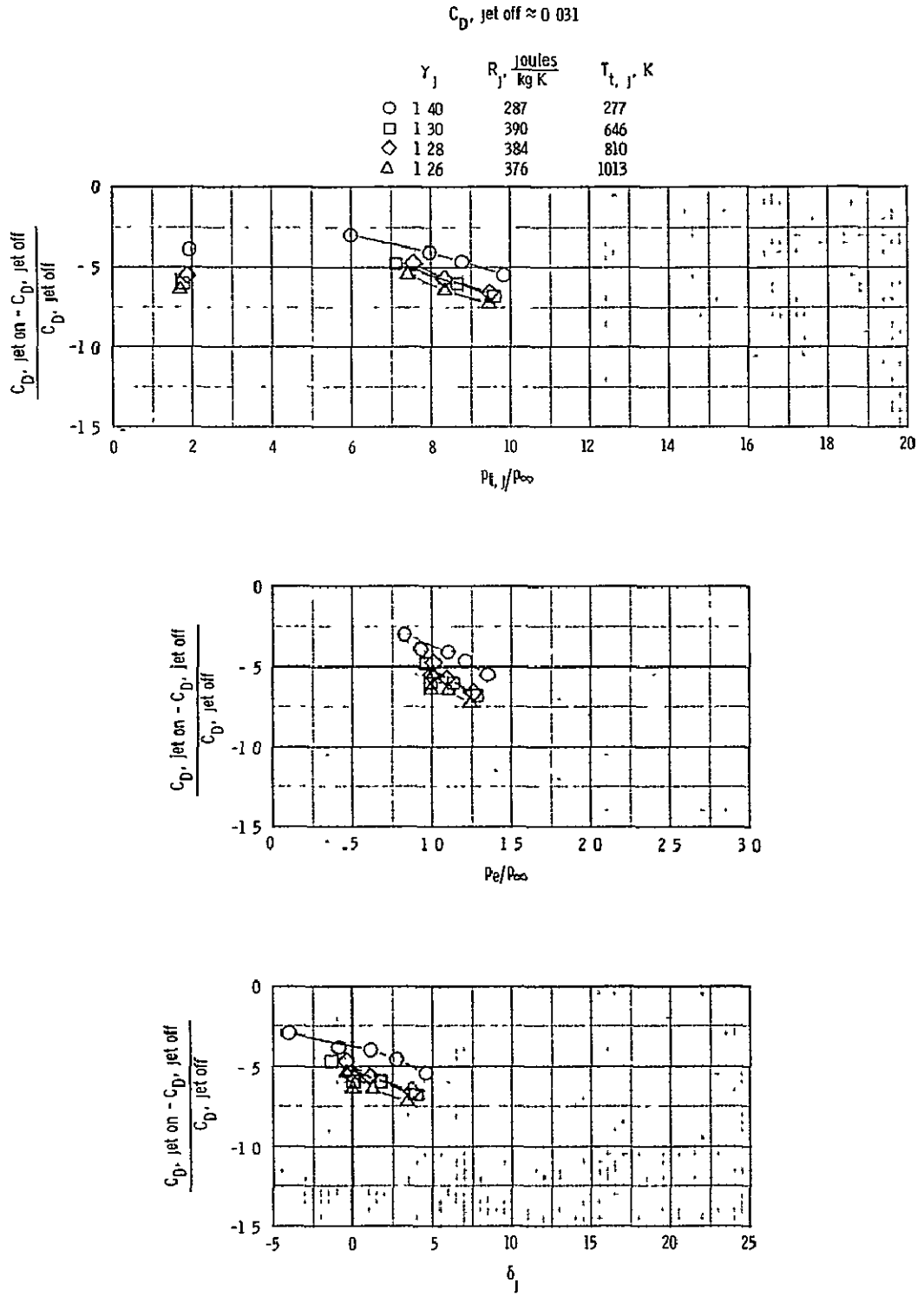

(a) $M_\infty = 0.60$.

Figure 14.- Incremental afterbody drag coefficient as a function of $P_{t,j}/P_\infty$, P_e/P_∞, and δ_j. ($\beta = 10^\circ$, $\ell/d_{max} = 1.5$, $M_e = 2$).

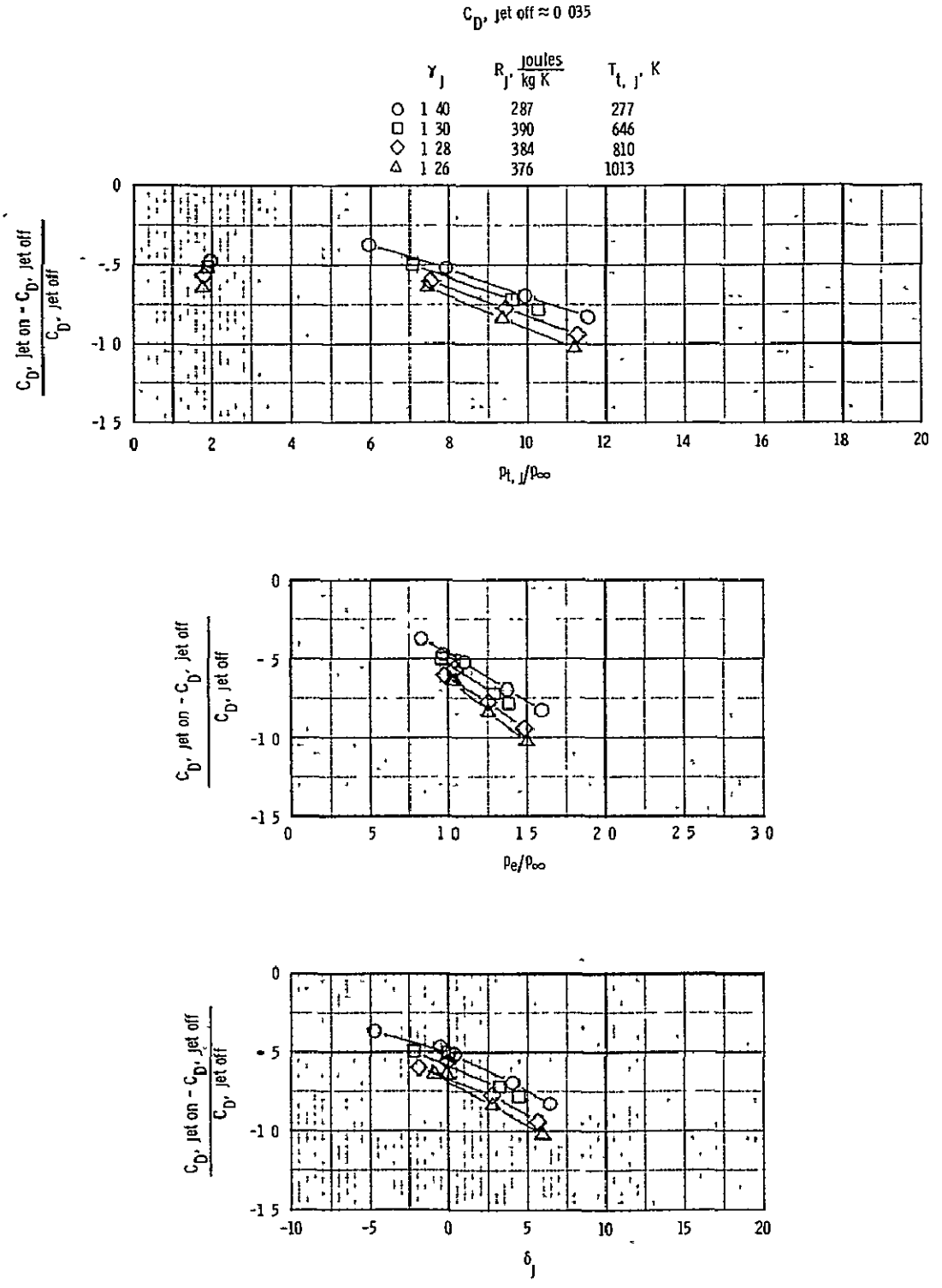

(b) $M_\infty = 0.80$.

Figure 14. – Continued.

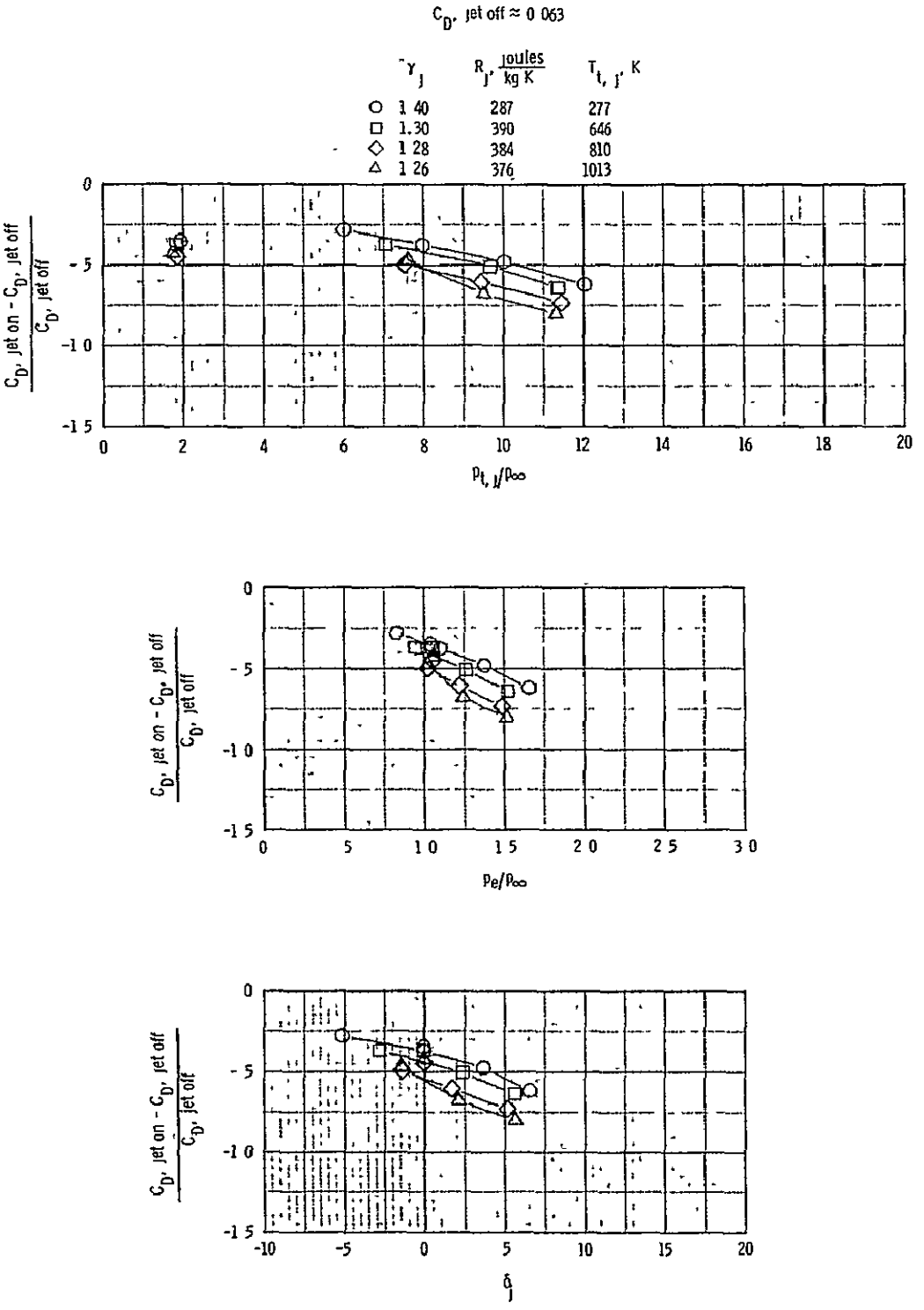

(c) $M_\infty = 0.90$.

Figure 14. – Continued.

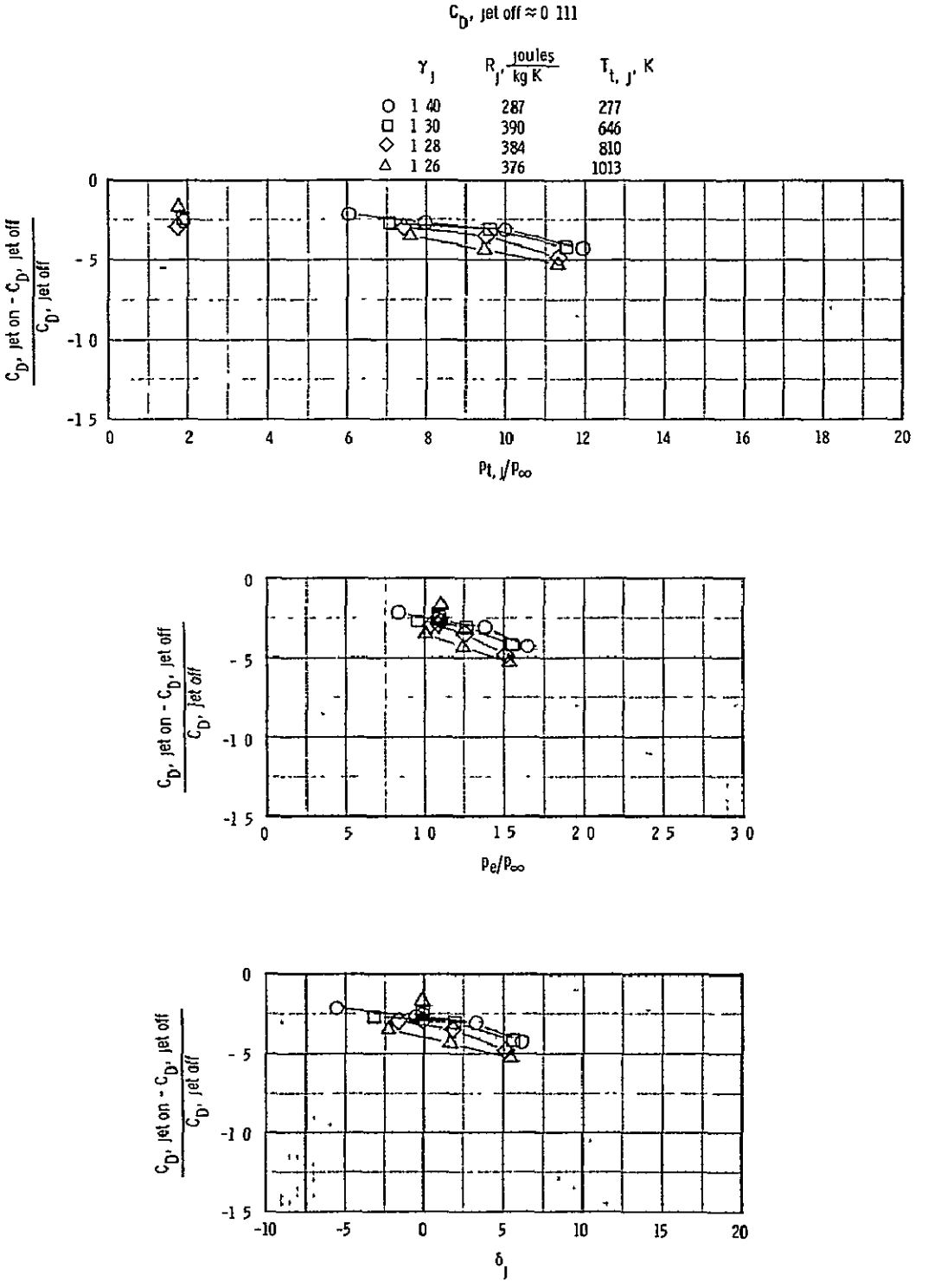

(d) $M_\infty = 0.95$.

Figure 14. - Continued.

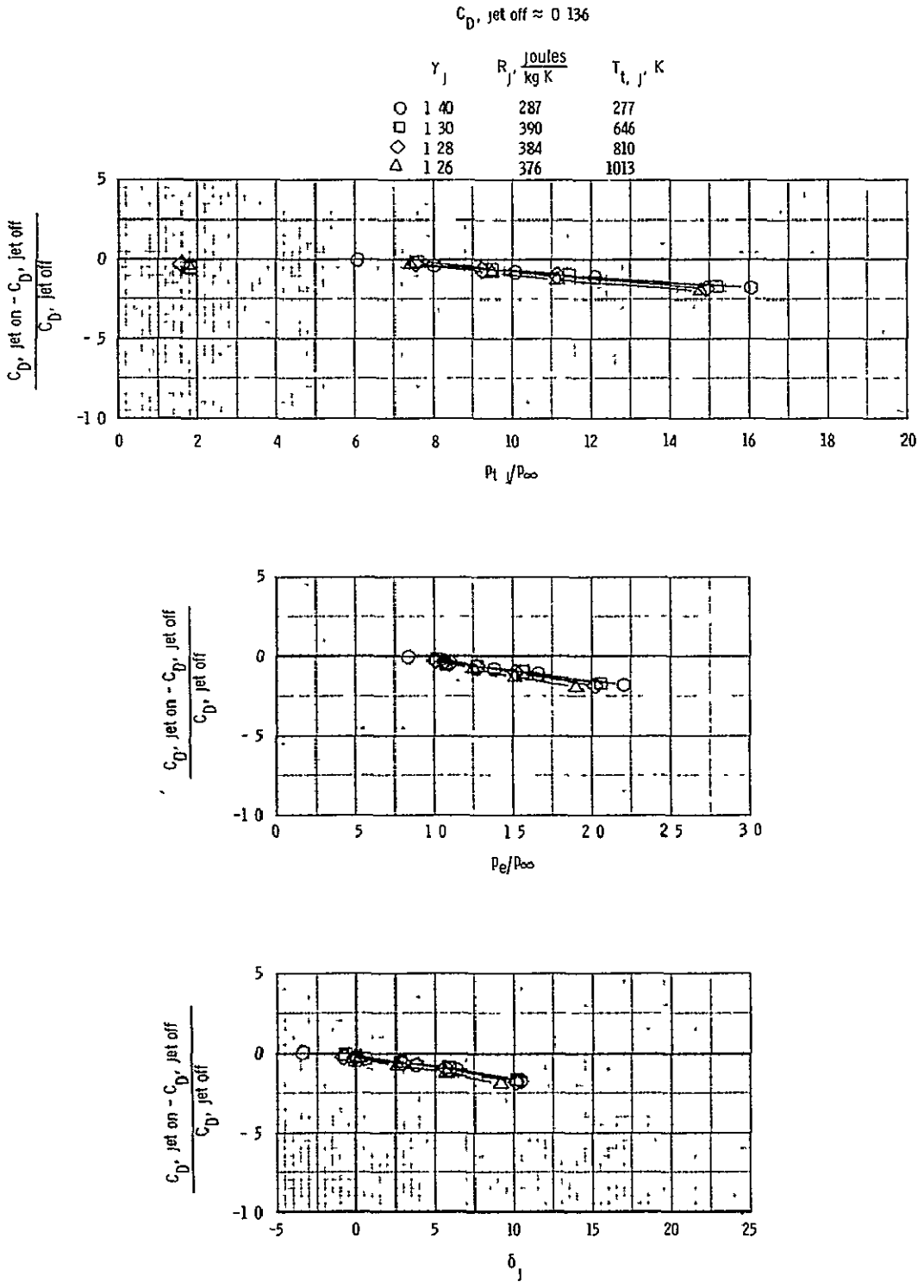

(e) $M_\infty = 1.20$.

Figure 14 – Concluded.

	γ_j	R_j, $\frac{\text{joules}}{\text{kg K}}$	$T_{t,j}$, K
○	1.40	287	300
□	1.30	390	646
◇	1.28	384	810
△	1.26	376	1013

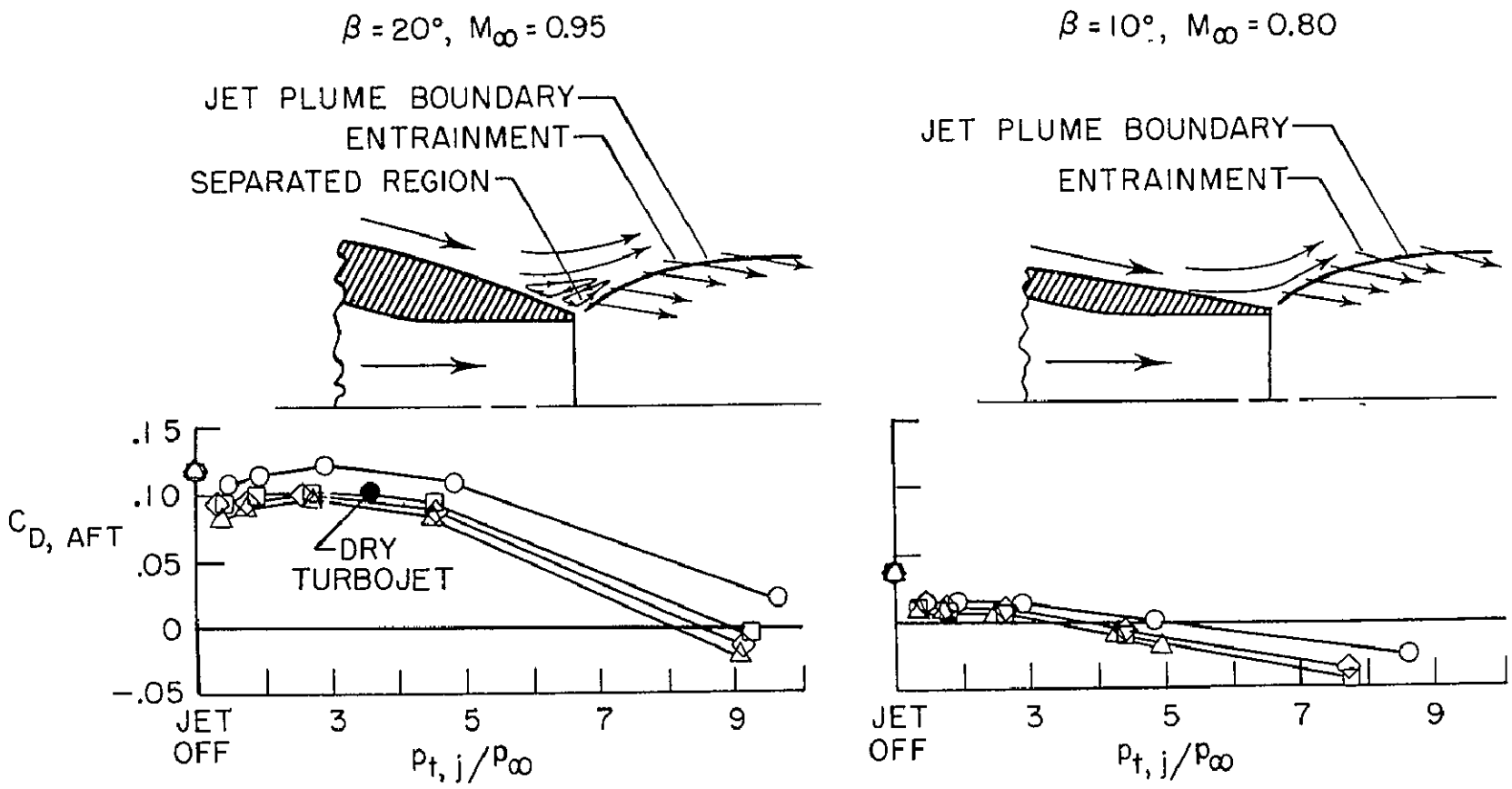

Figure 15.- Effect of jet exhaust gas parameters on jet interference.

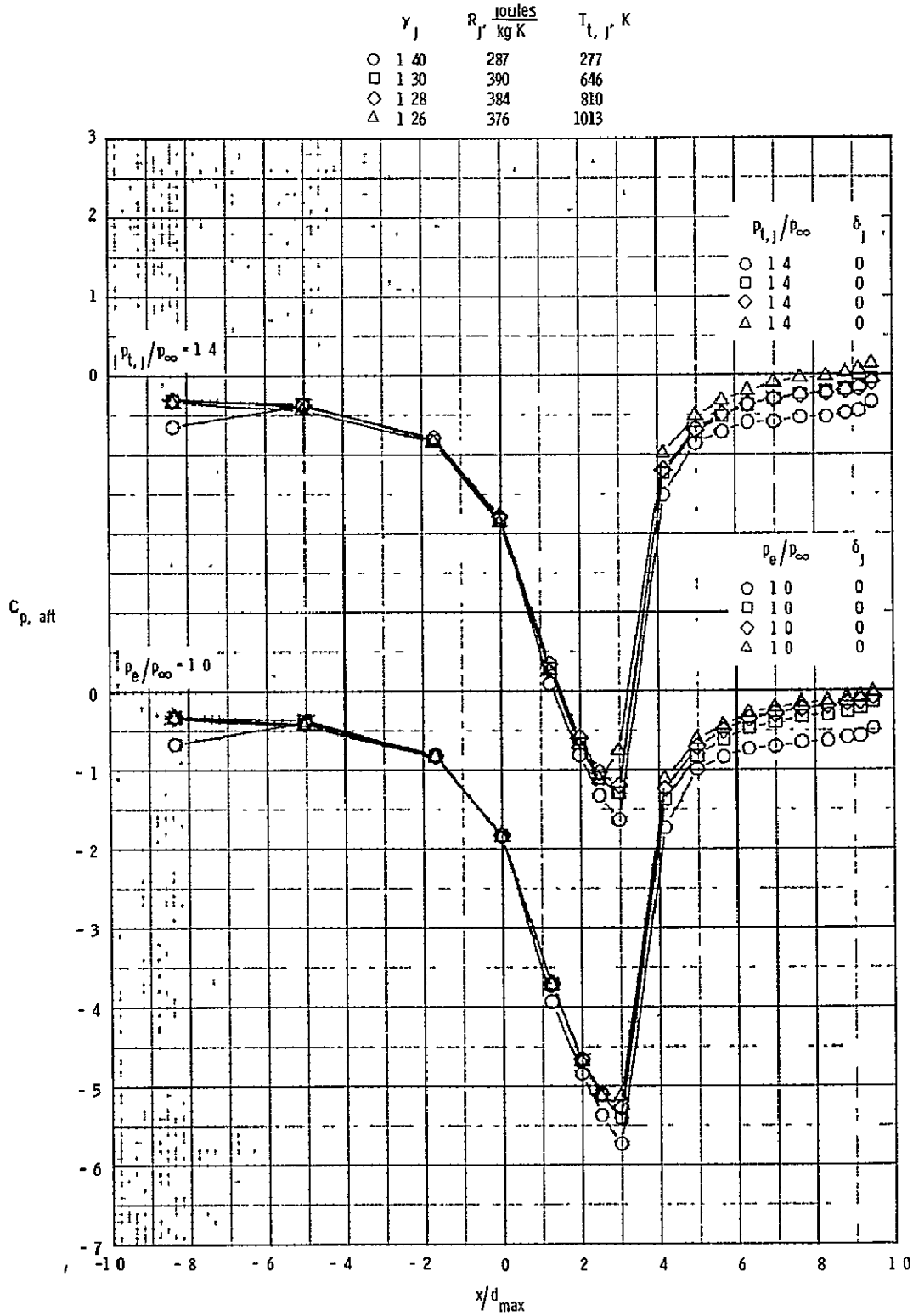

(a) $\beta = 20^\circ$, $\ell/d_{max} = 1.0$, $p_{t,j}/p_\infty = 1.4$ and $p_e/p_\infty = 1.0$.

Figure 16. - Comparison of jet interference on the afterbody pressures for the various exhaust gases at equal values of jet exit pressure ratio ($M_\infty = 0.95$, sonic exit).

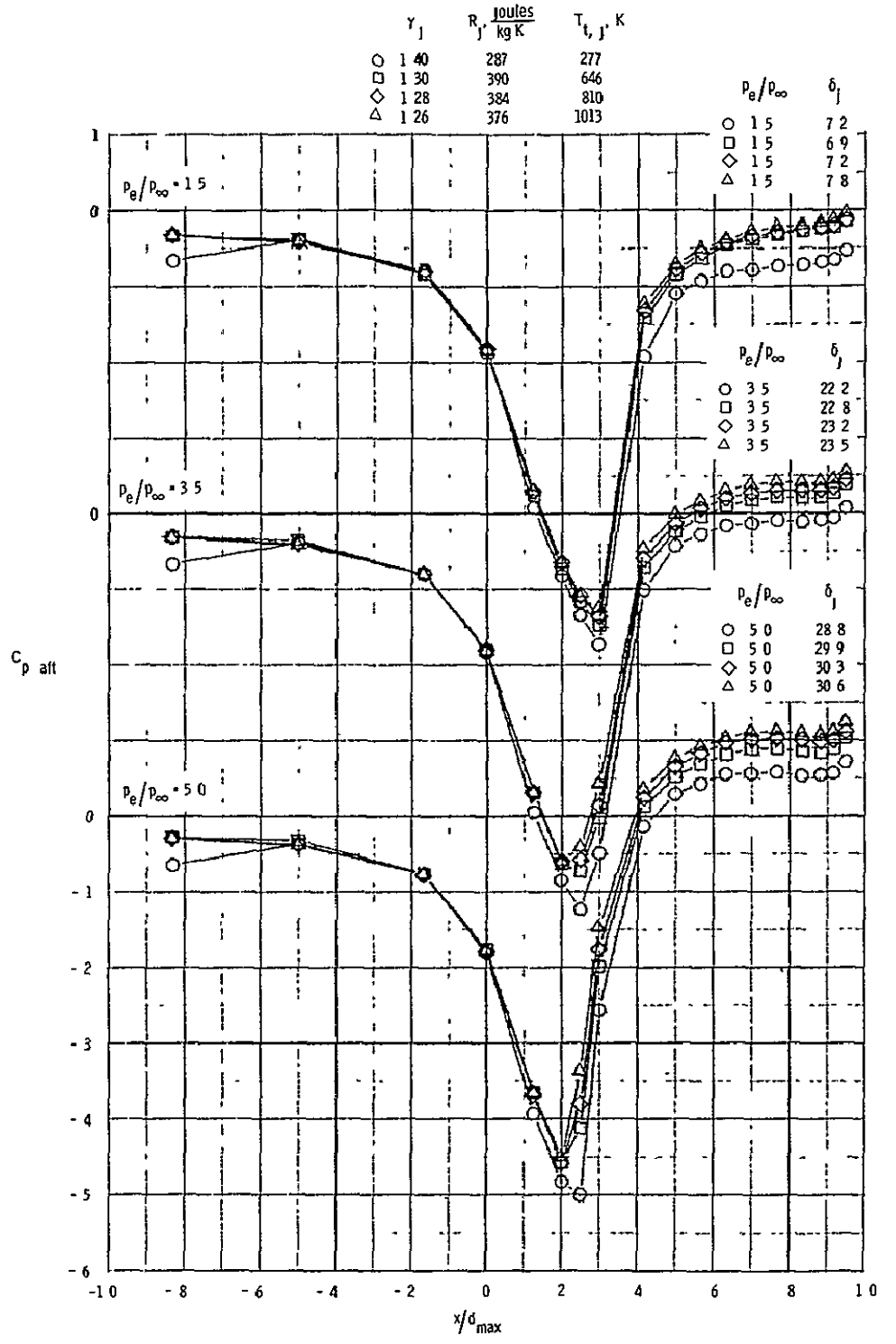

(b) $\beta = 20^\circ$, $\ell/d_{max} = 1.0$, $p_e/p_\infty = 1.5$ through 5.0.

Figure 16. - Continued.

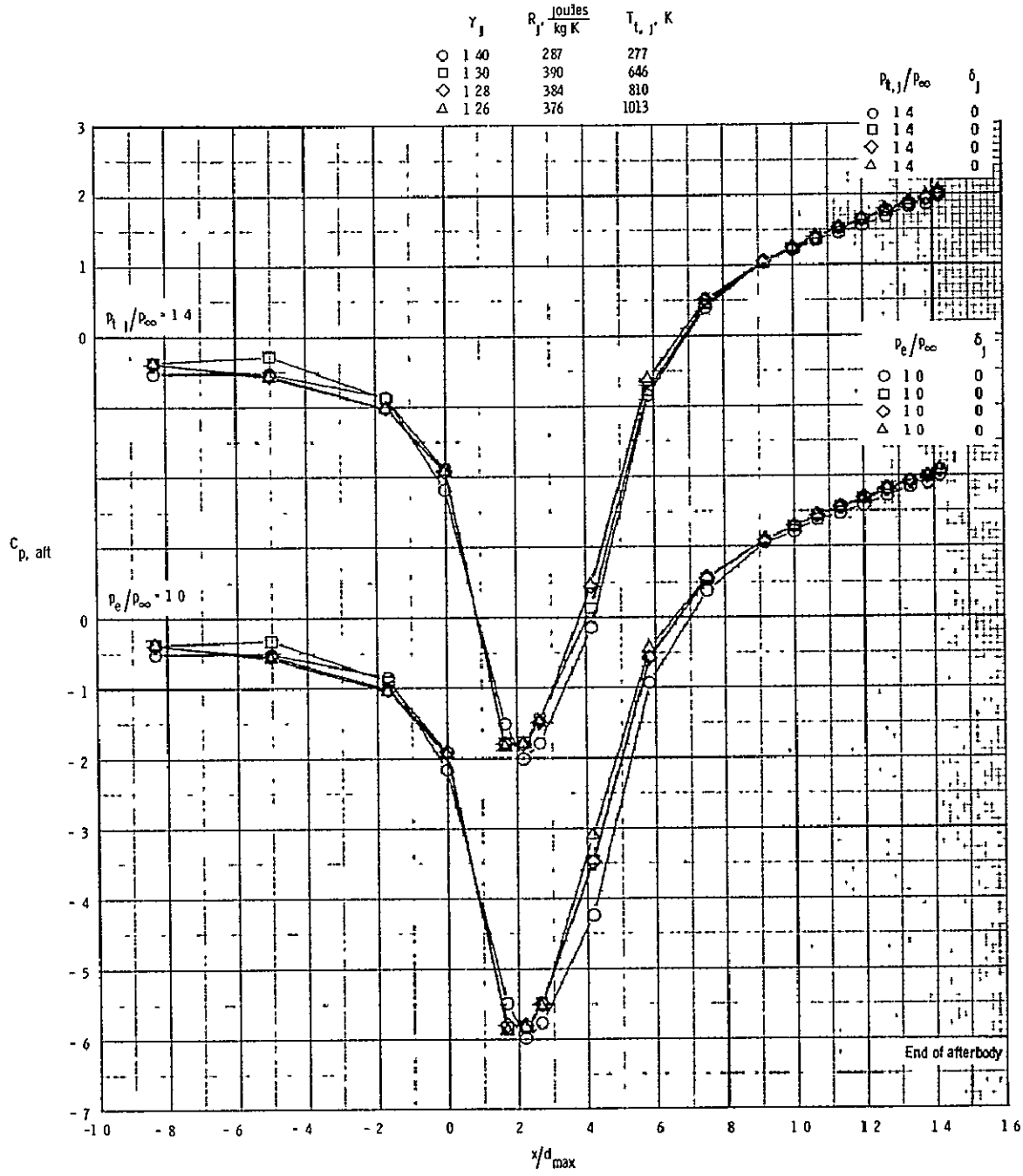

(c) $\beta = 10^\circ$, $\ell/d_{max} = 1.5$, $p_{t,j}/p_\infty = 1.4$ and $p_e/p_\infty = 1.0$.

Figure 16 - Continued.

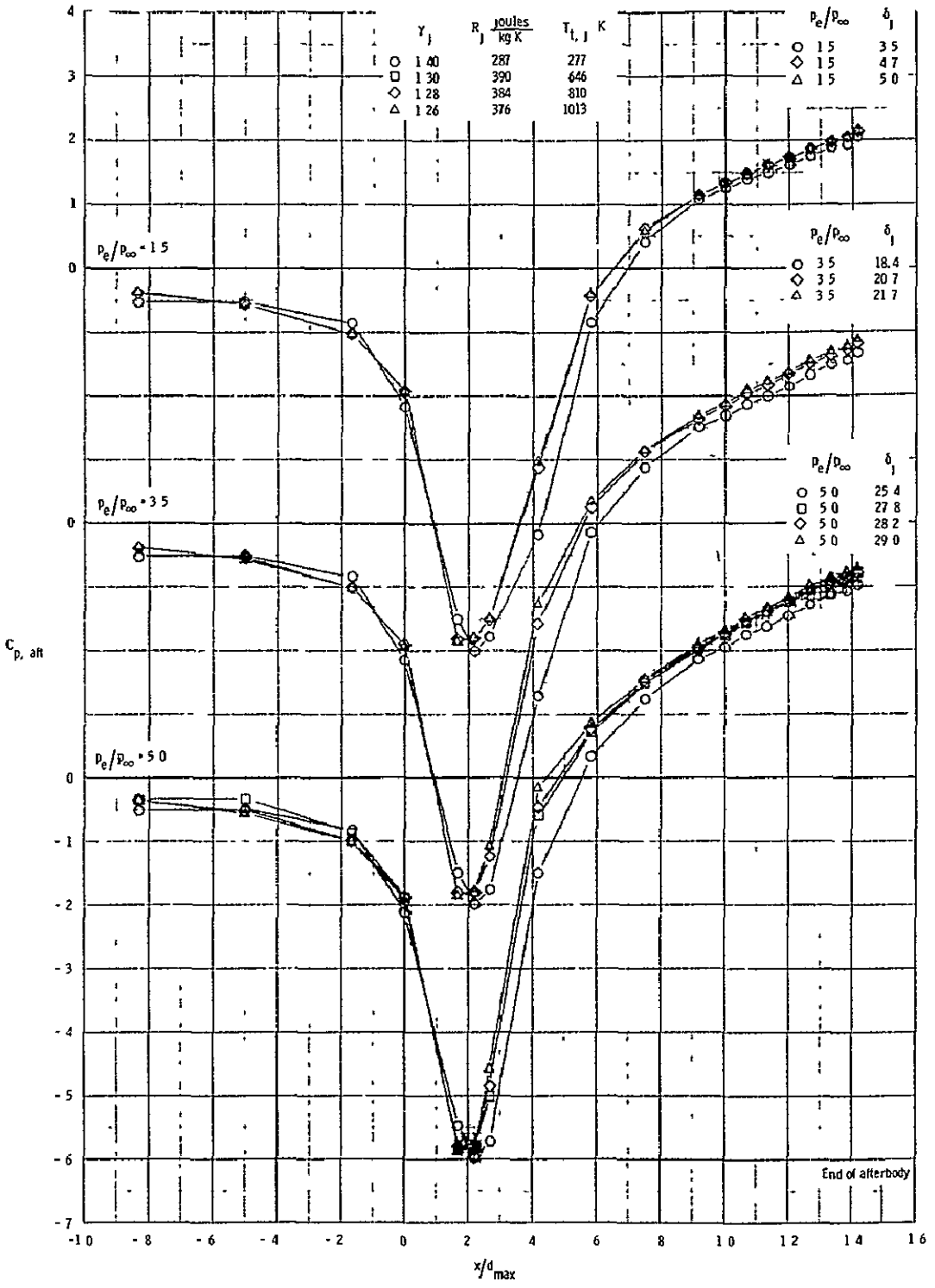

(d) $\beta = 10^\circ$, $\ell/d_{max} = 1.5$, $p_e/p_\infty = 1.5$ through 5.0.

Figure 16. - Concluded.

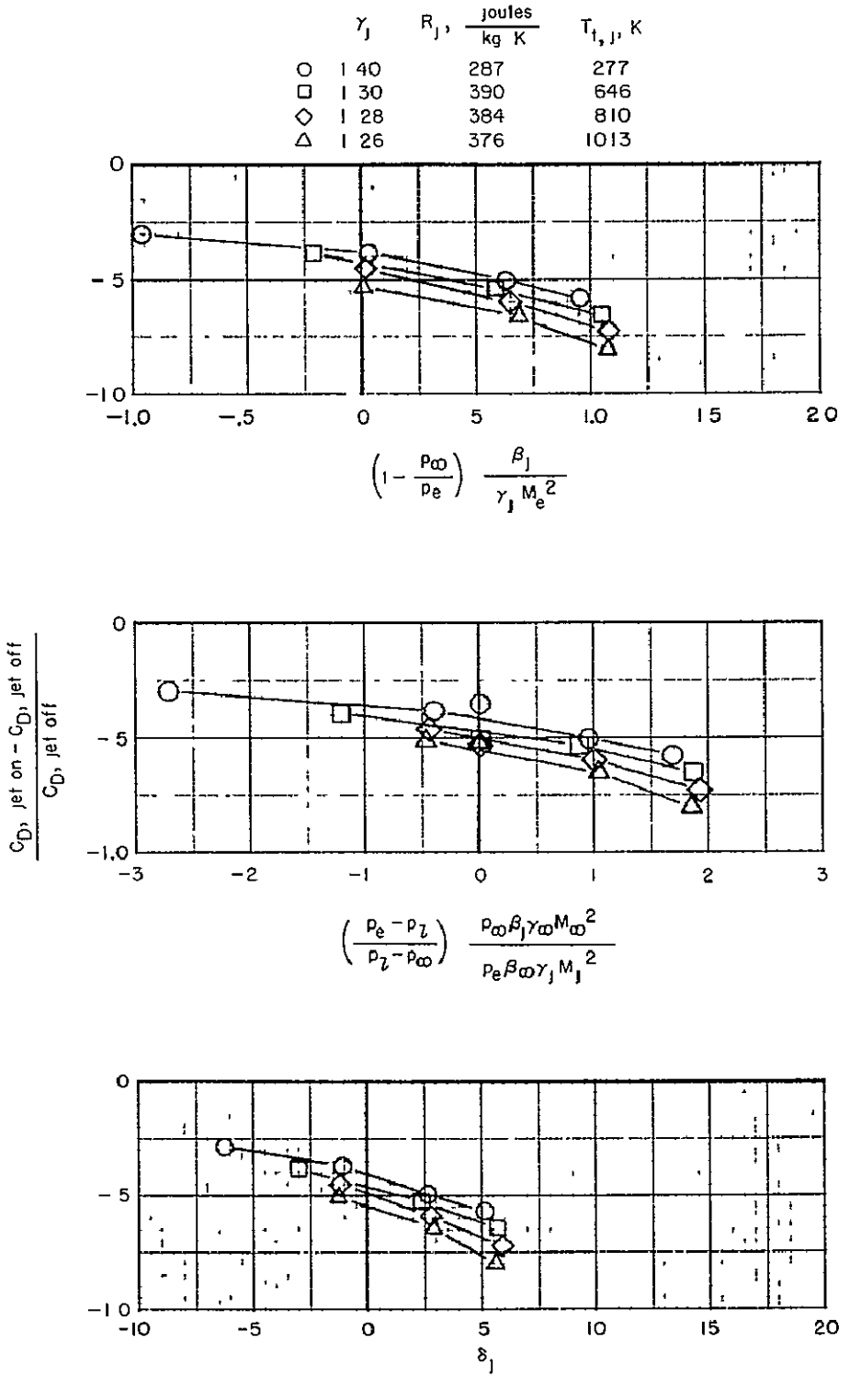

Figure 17.- Comparison of jet boundary simulation parameters ($\beta = 20^\circ$, $\ell/d_{max} = 1.0$, $M_e = 2$, $M_\infty = 0.90$).

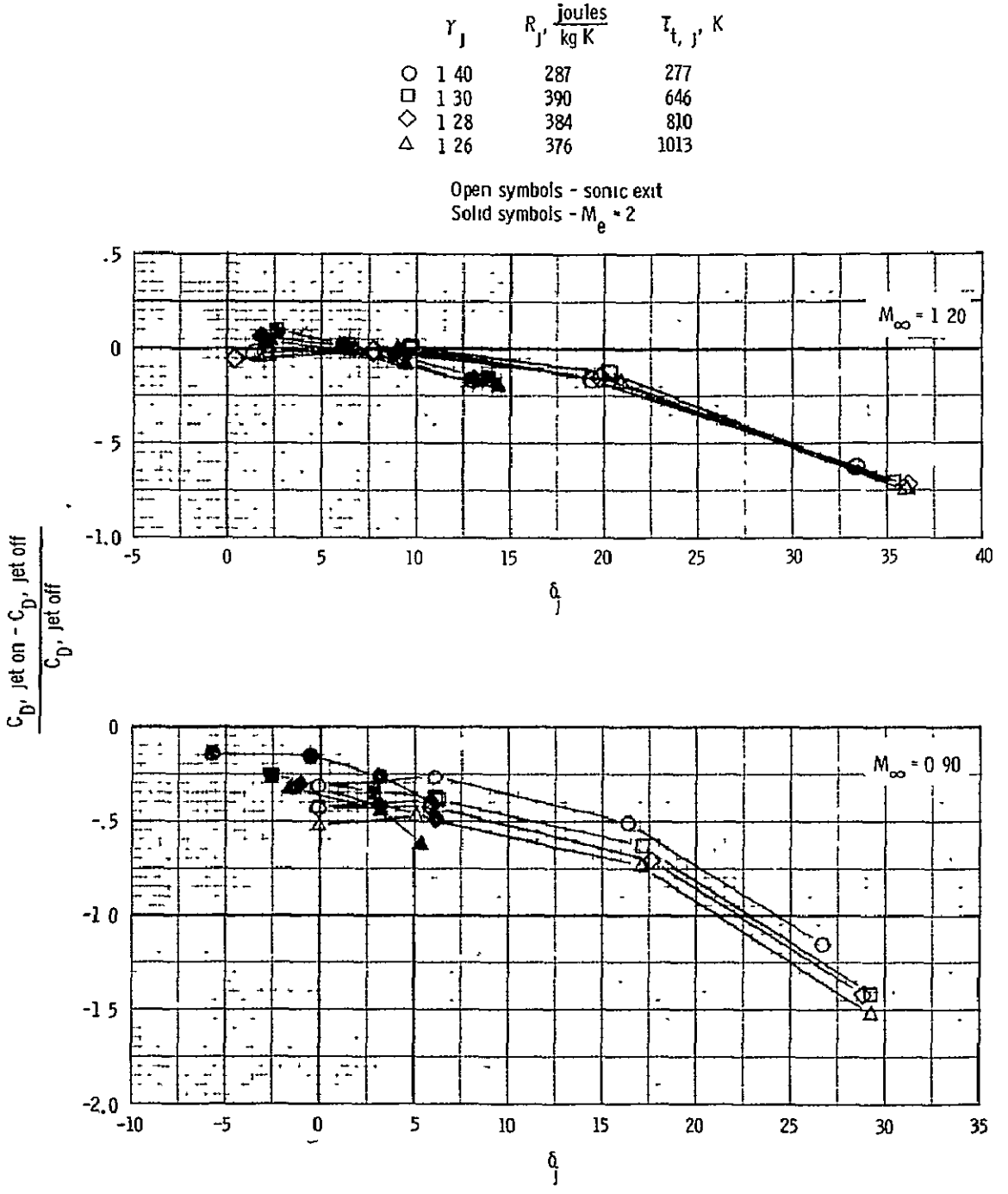

(a) $\beta = 20^\circ$, $\ell/d_{max} = 1.0$

Figure 18.- Comparison of jet interference versus the initial inclination angle of the jet plume for a sonic jet exit and a Mach 2 jet exit.

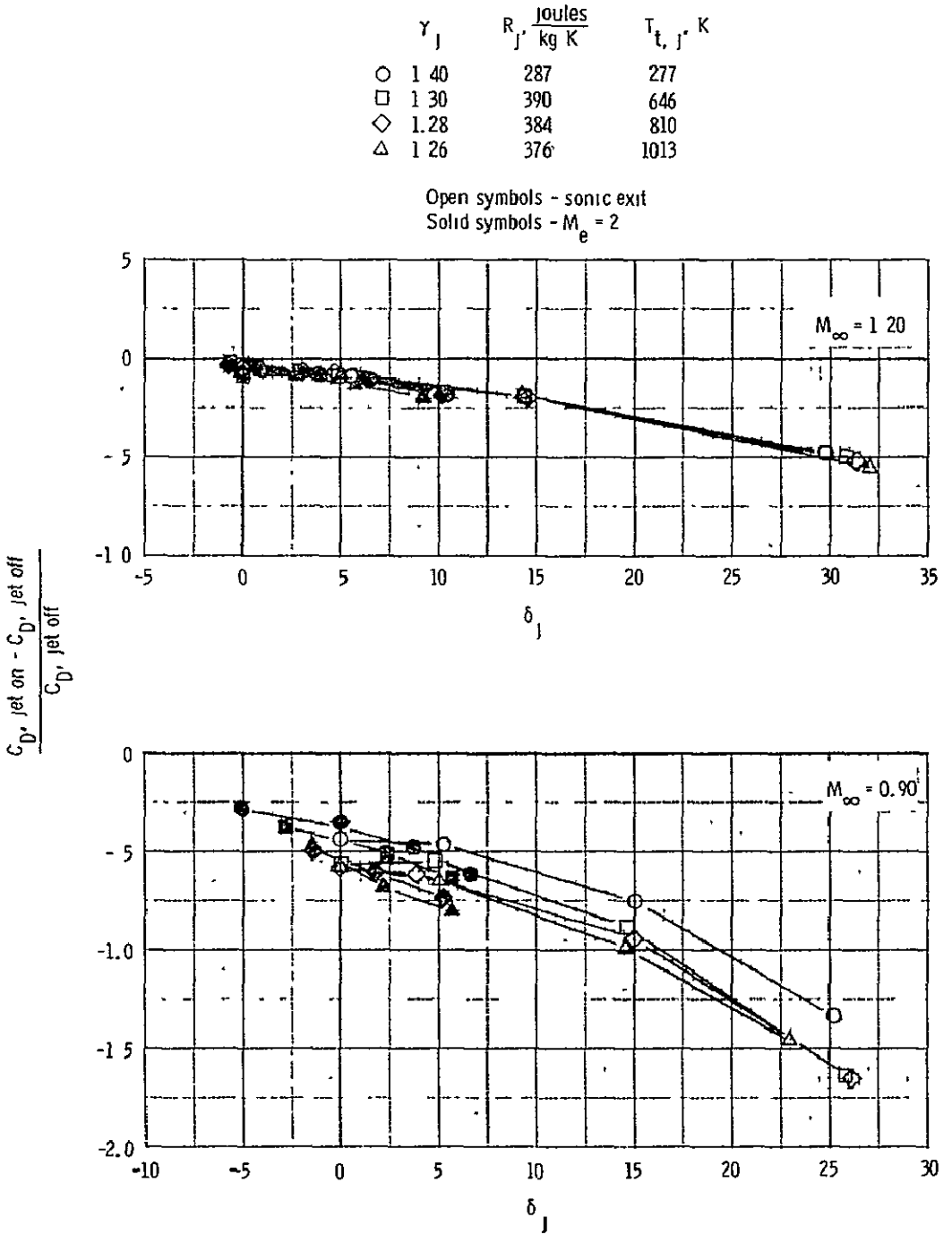

(b) $\beta = 10^{\circ}$, $\ell/d_{max} = 1.5$.

Figure 18. - Concluded.

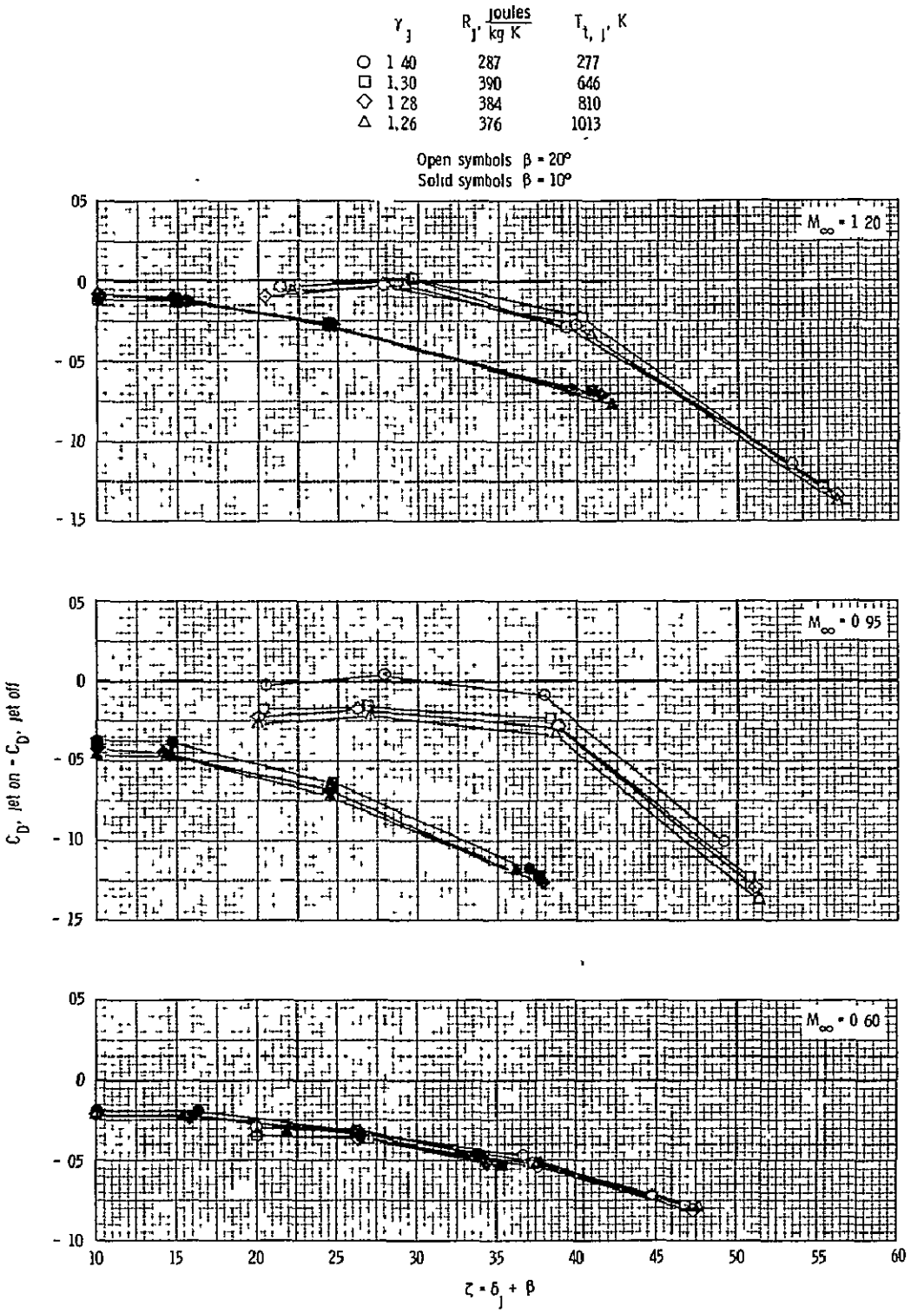

Figure 19.- Comparison of jet interference as a function of hypothetical trailing edge flow turning angle. (Sonic exit).

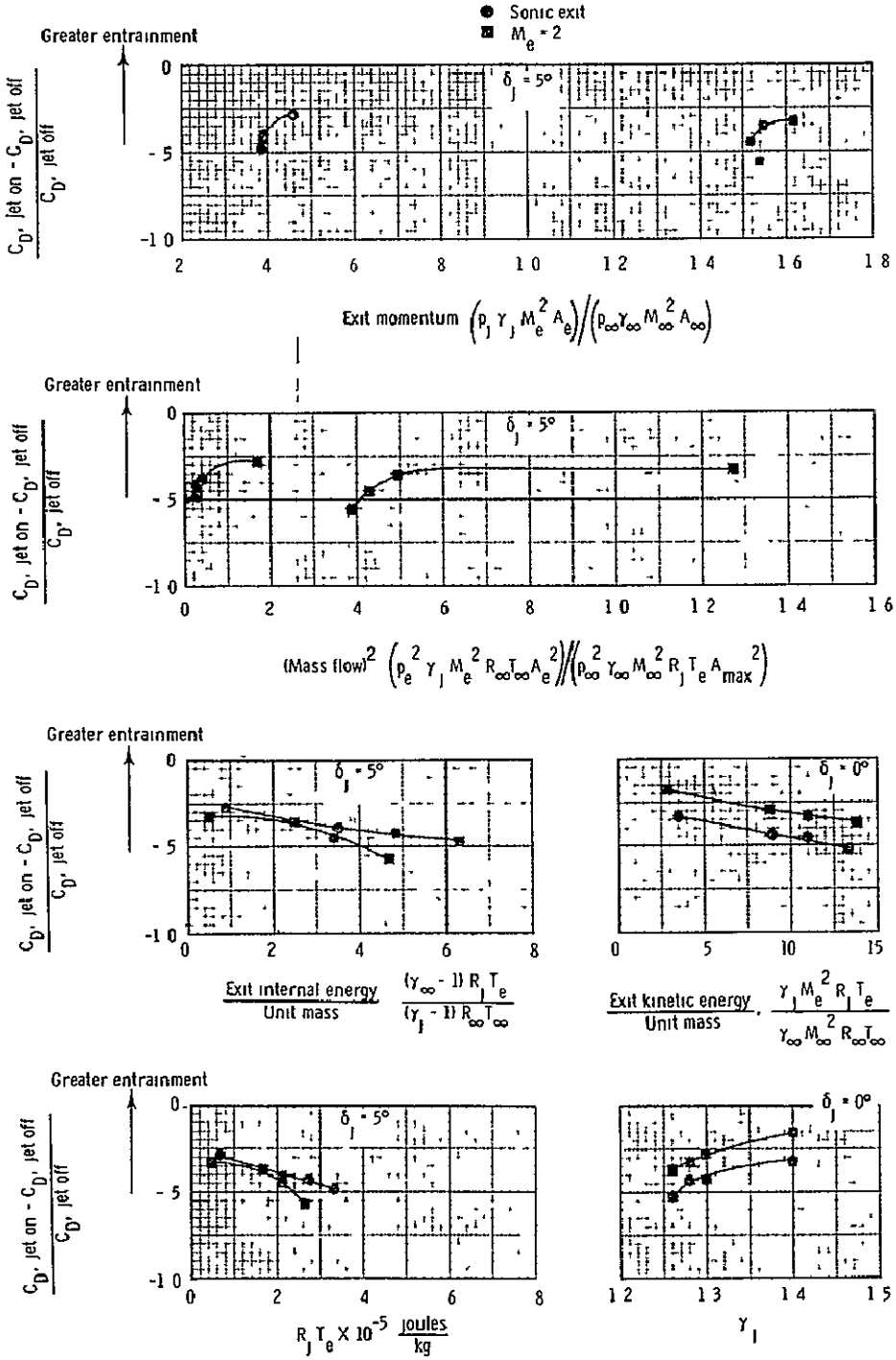

Figure 20 .- Comparison of entrainment correlation parameters computed for jet exit conditions. ($\beta = 20^\circ$, $\ell/d_{max} = 1.0$, $M_\infty = 0.90$. Small solid symbols indicate cross plotted values).

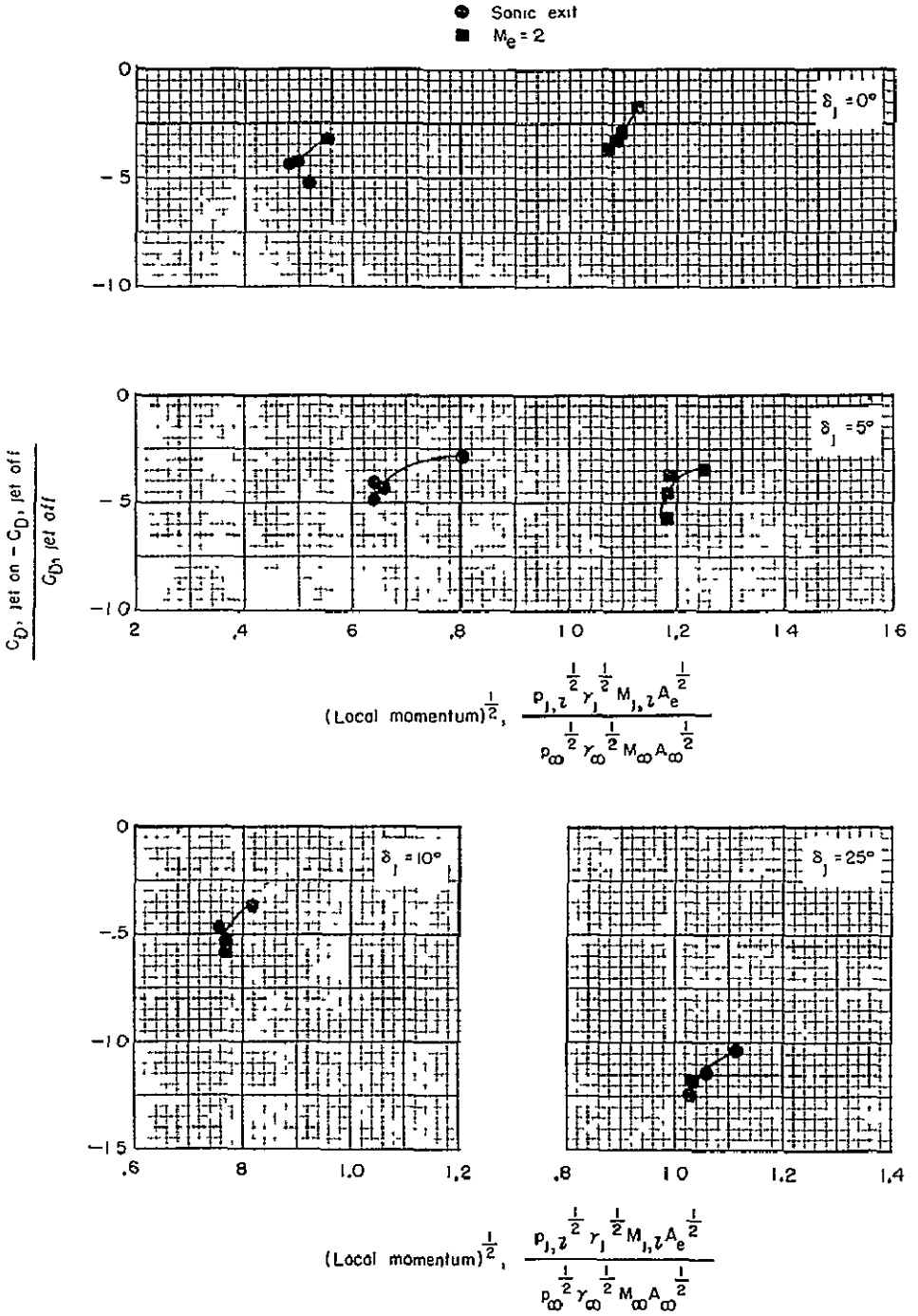

Figure 21.- Incremental afterbody drag coefficient versus momentum entrainment parameter computed for local jet exhaust conditions. ($\beta = 20^o$, $\ell/d_{max} = 1.0$, $M_\infty = 0.90$. Small solid symbols indicate cross-plotted values).

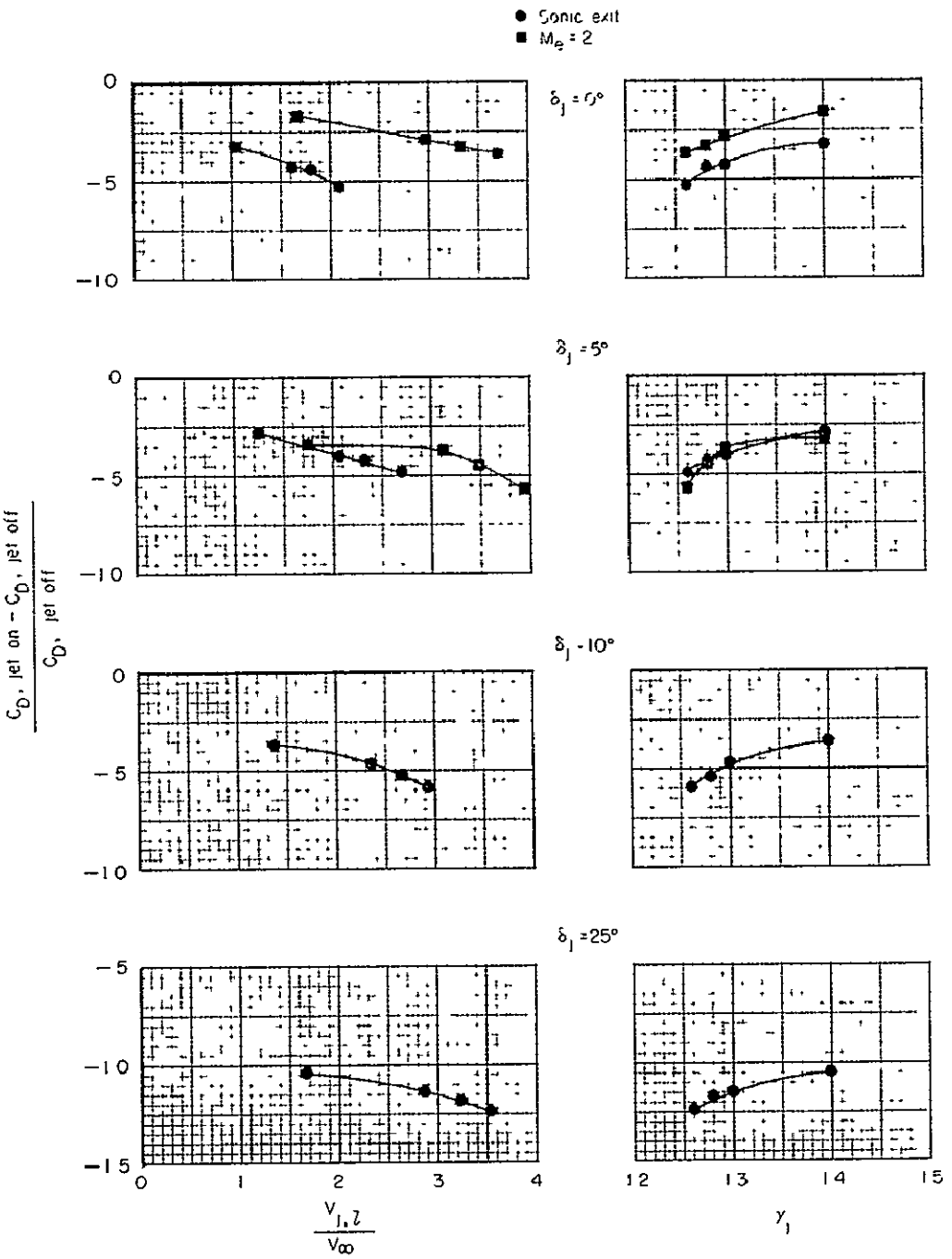

Figure 22.- Incremental afterbody drag coefficient versus $V_{j,\ell}/V_\infty$ and γ_j. ($\beta = 20^\circ$, $\ell/d_{max} = 1.0$, $M_\infty = 0.90$. Small solid symbols indicate cross-plotted values).

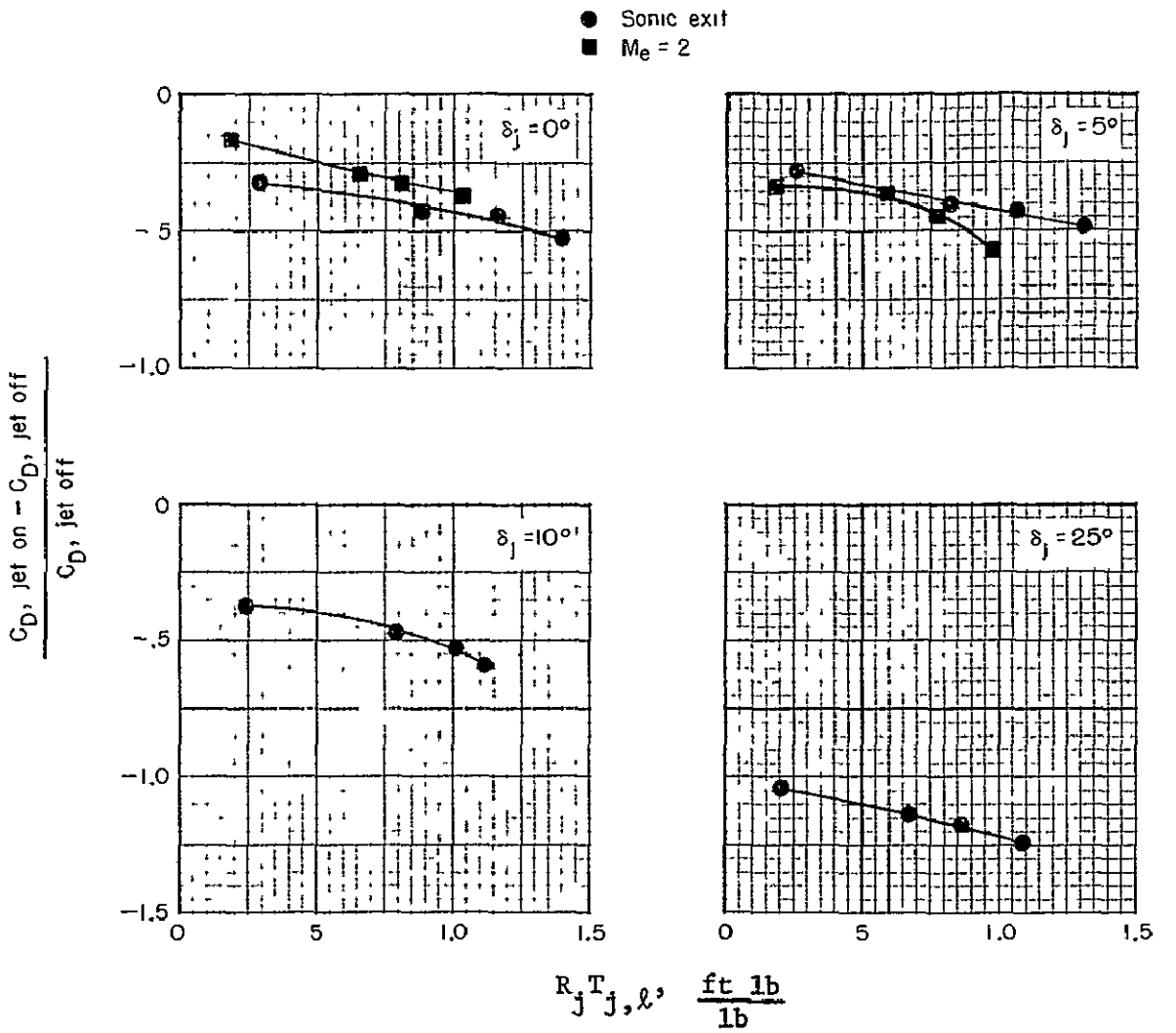

Figure 23.- Incremental afterbody drag coefficient versus $R_j T_j, \ell'/R_\infty T_\infty$. ($\beta = 20^\circ$, $\ell/d_{max} = 1.0$, $M_\infty = 0.90$. Small solid symbols indicate cross-plotted values).

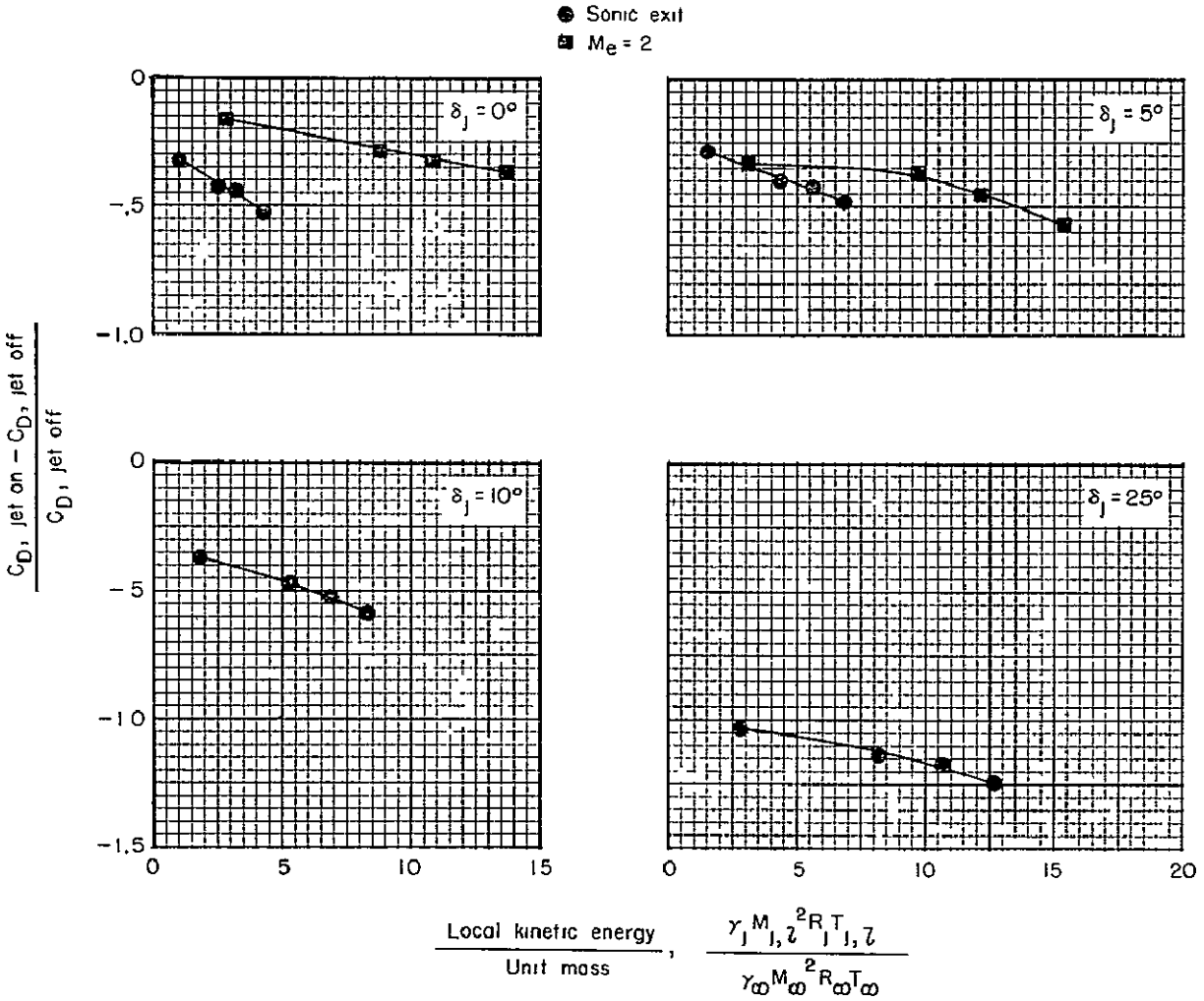

Figure 24.- Incremental afterbody drag coefficient versus local kinetic energy per unit mass ratio. ($\beta = 20^\circ$, $\ell/d_{max} = 1.0$, $M_\infty = 0.90$. Small solid symbols indicate cross-plotted values).

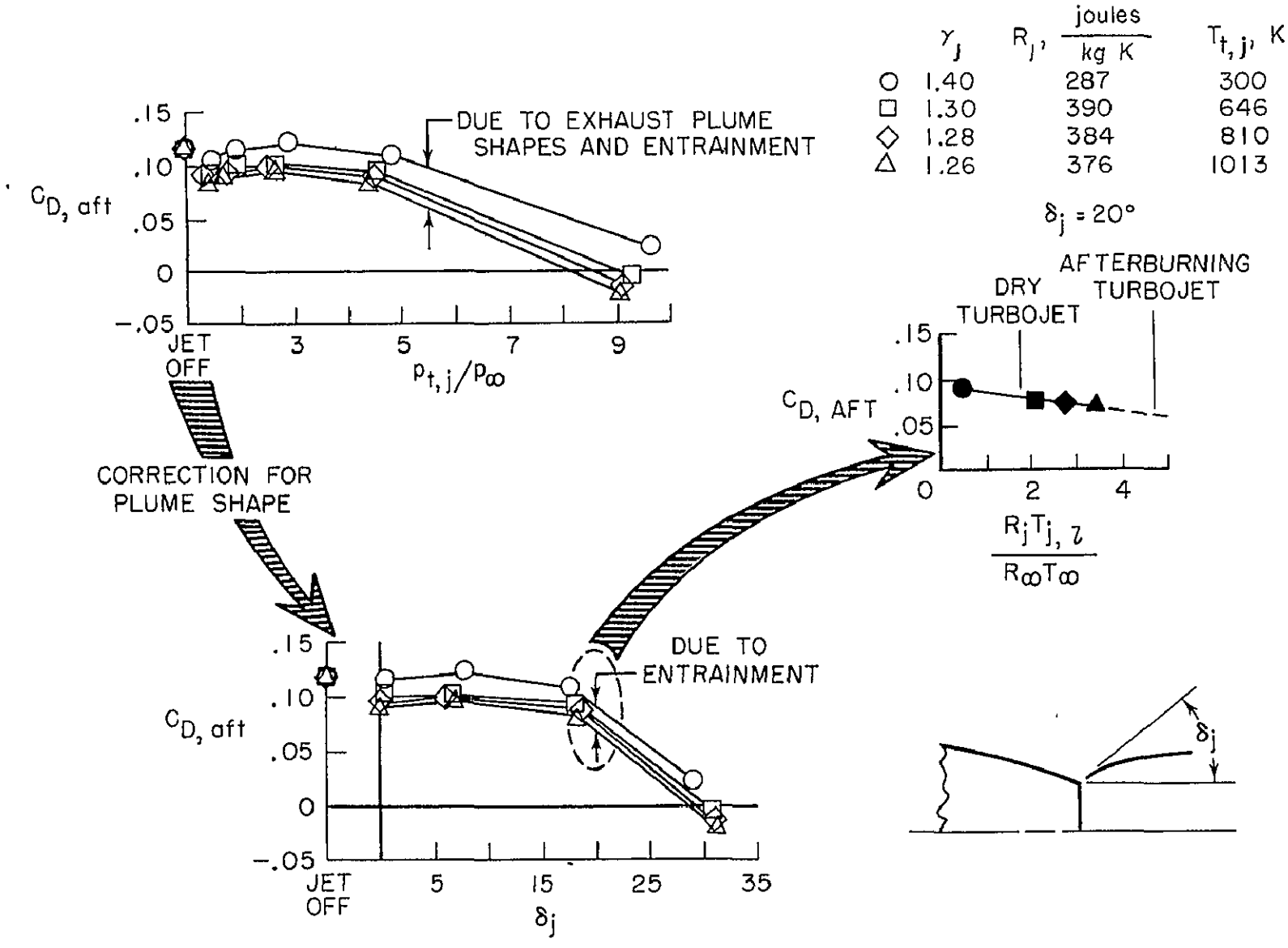

Figure 25.- Application of jet simulation parameters. $M_\infty = 0.95$, $\beta = 20°$, sonic exit.

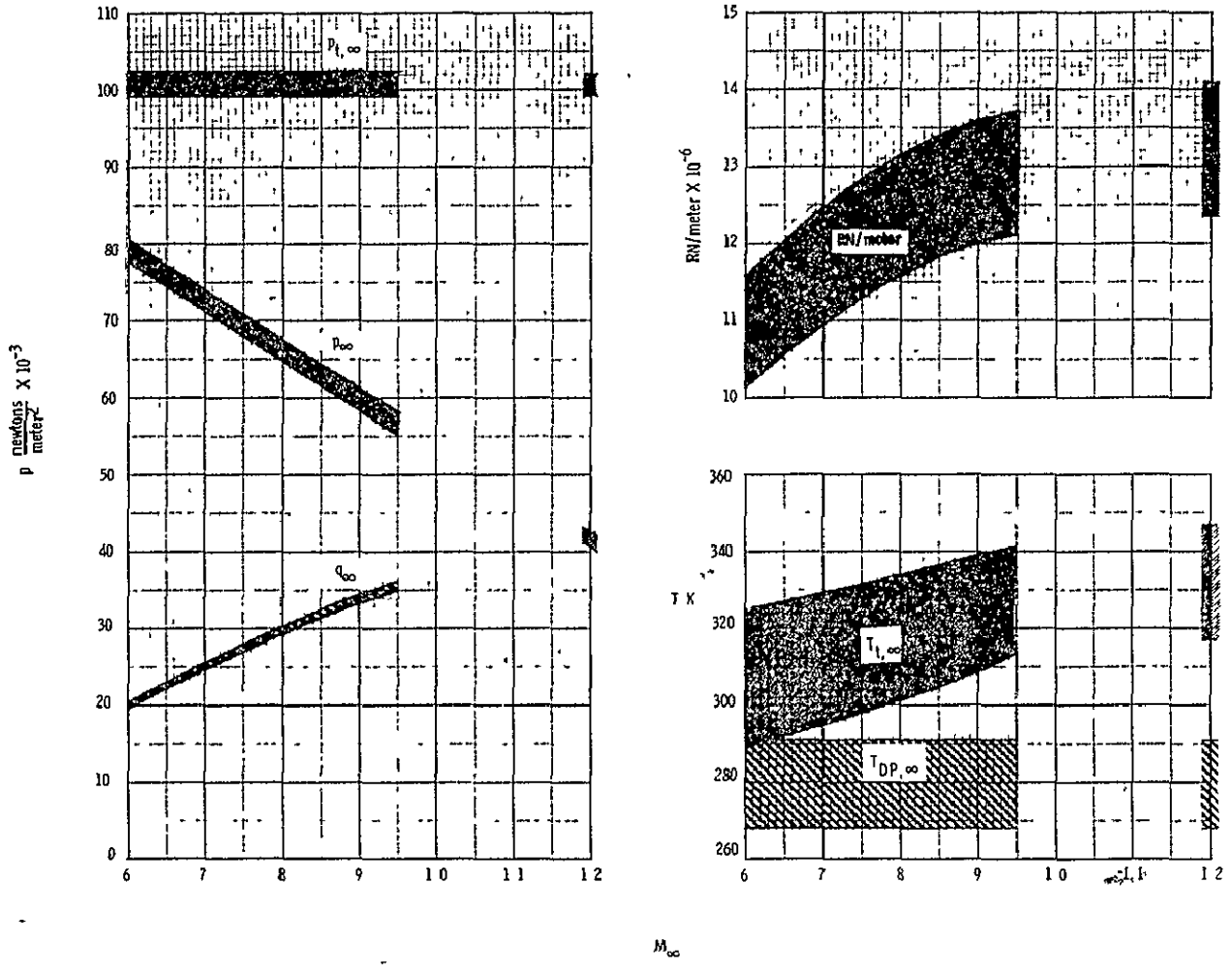

Figure 26.- Band of free-stream parameters versus Mach number.

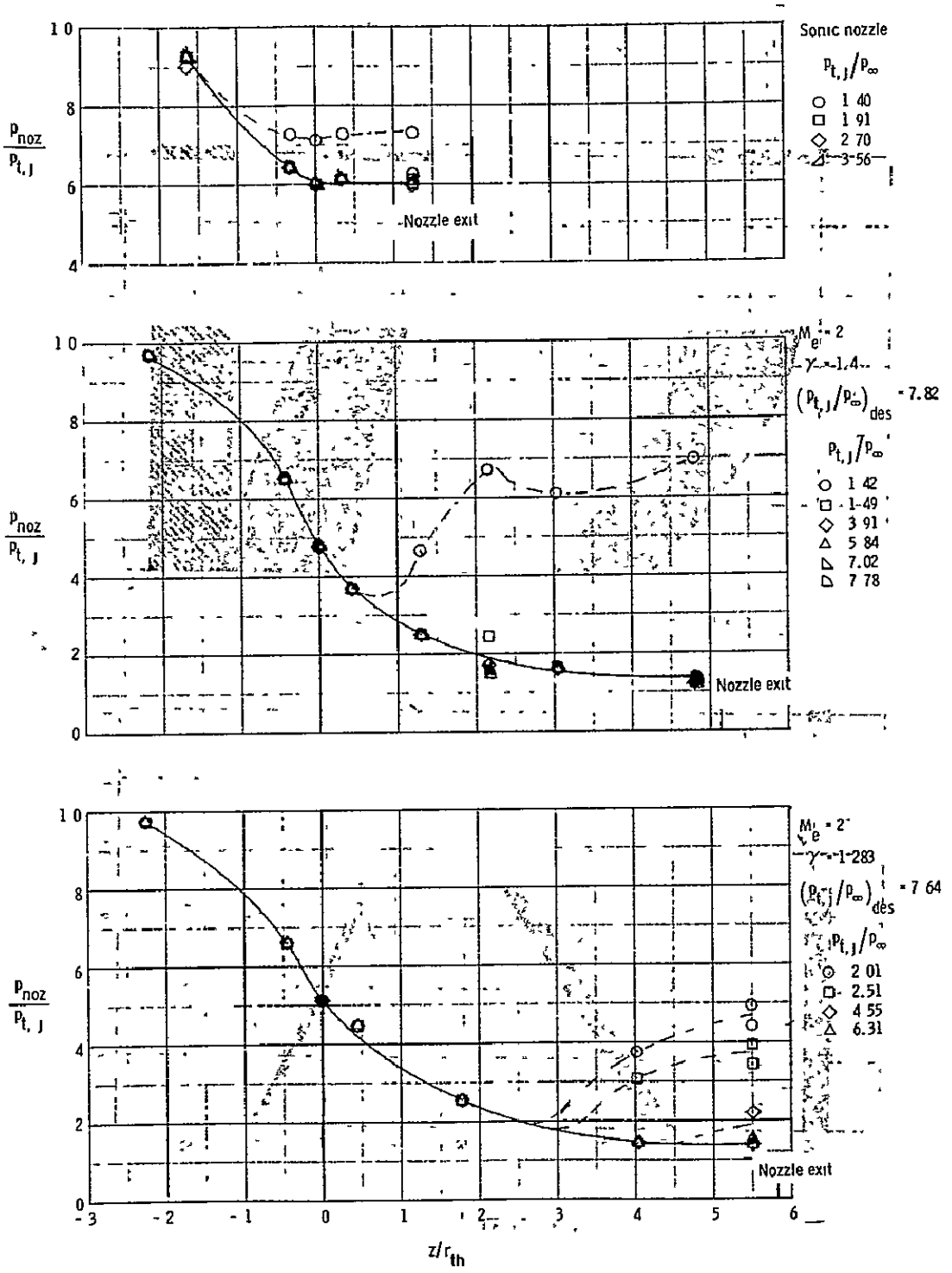

Figure 27.- Nozzle internal pressure distributions.

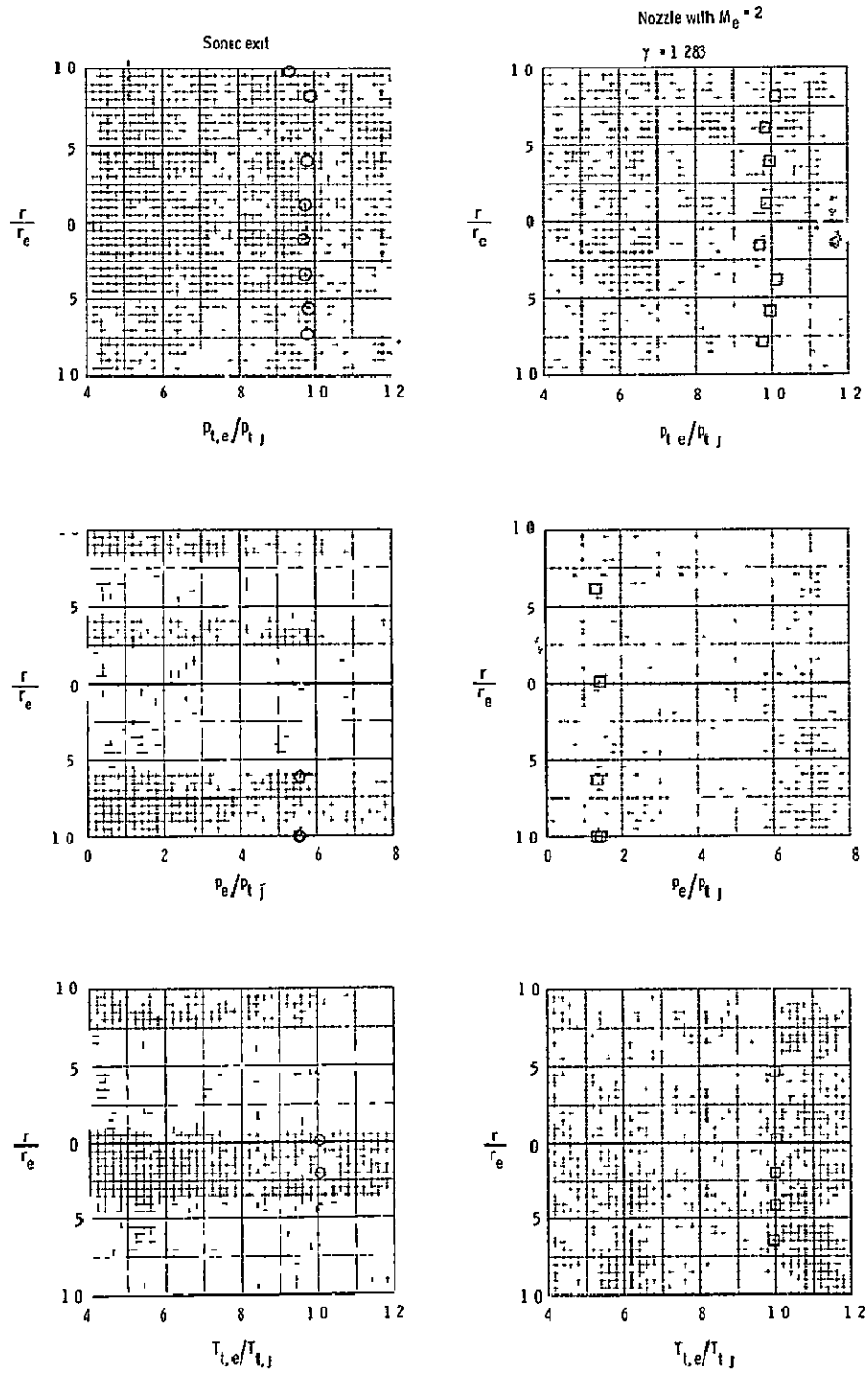

Figure 28.- Typical nozzle exit pressure and temperature profiles ($p_e/p_\infty \approx 1.0$, $\gamma_j = 1.283$).

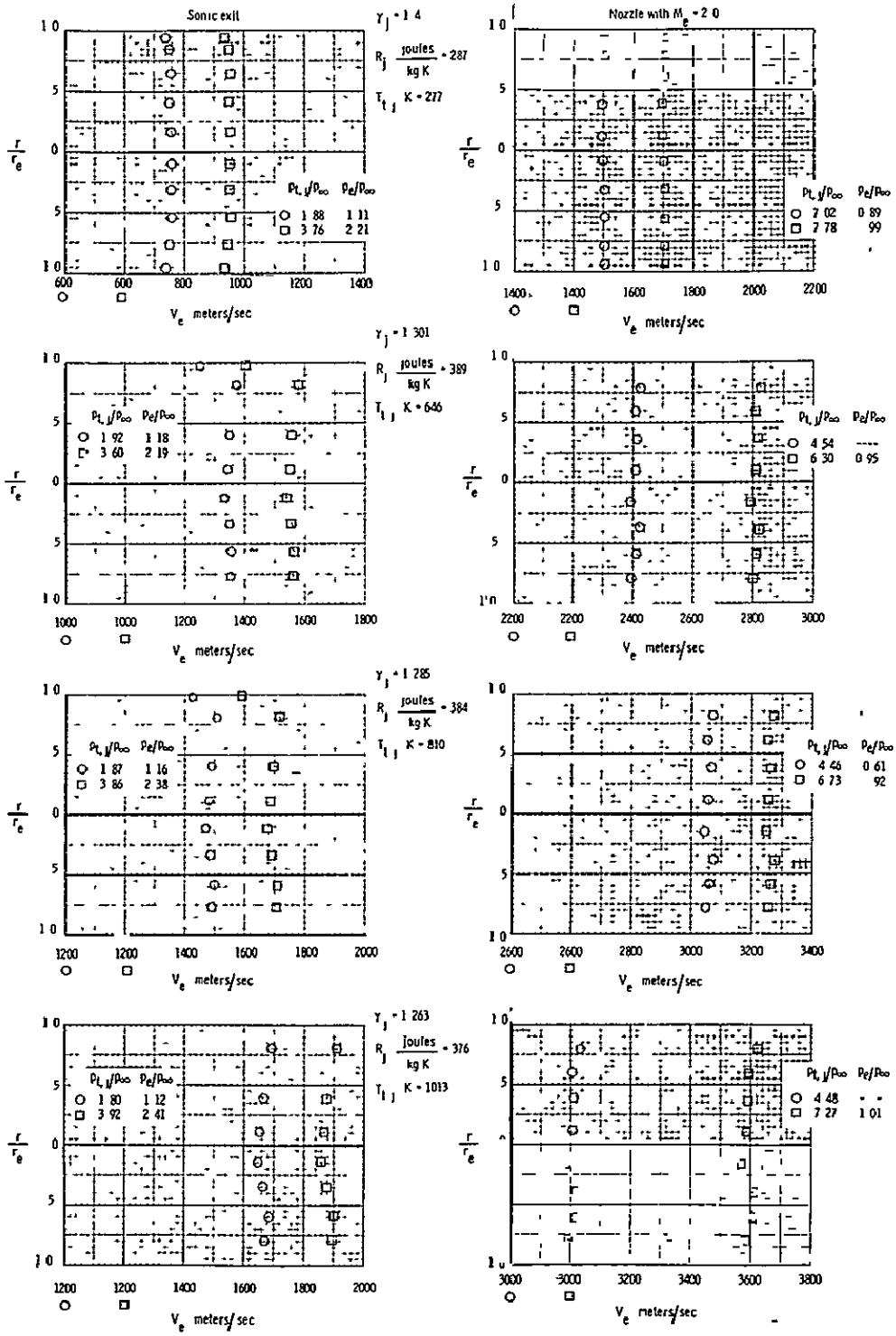

Figure 29.- Typical exit velocity profiles for the sonic and Mach 2 jet exits.

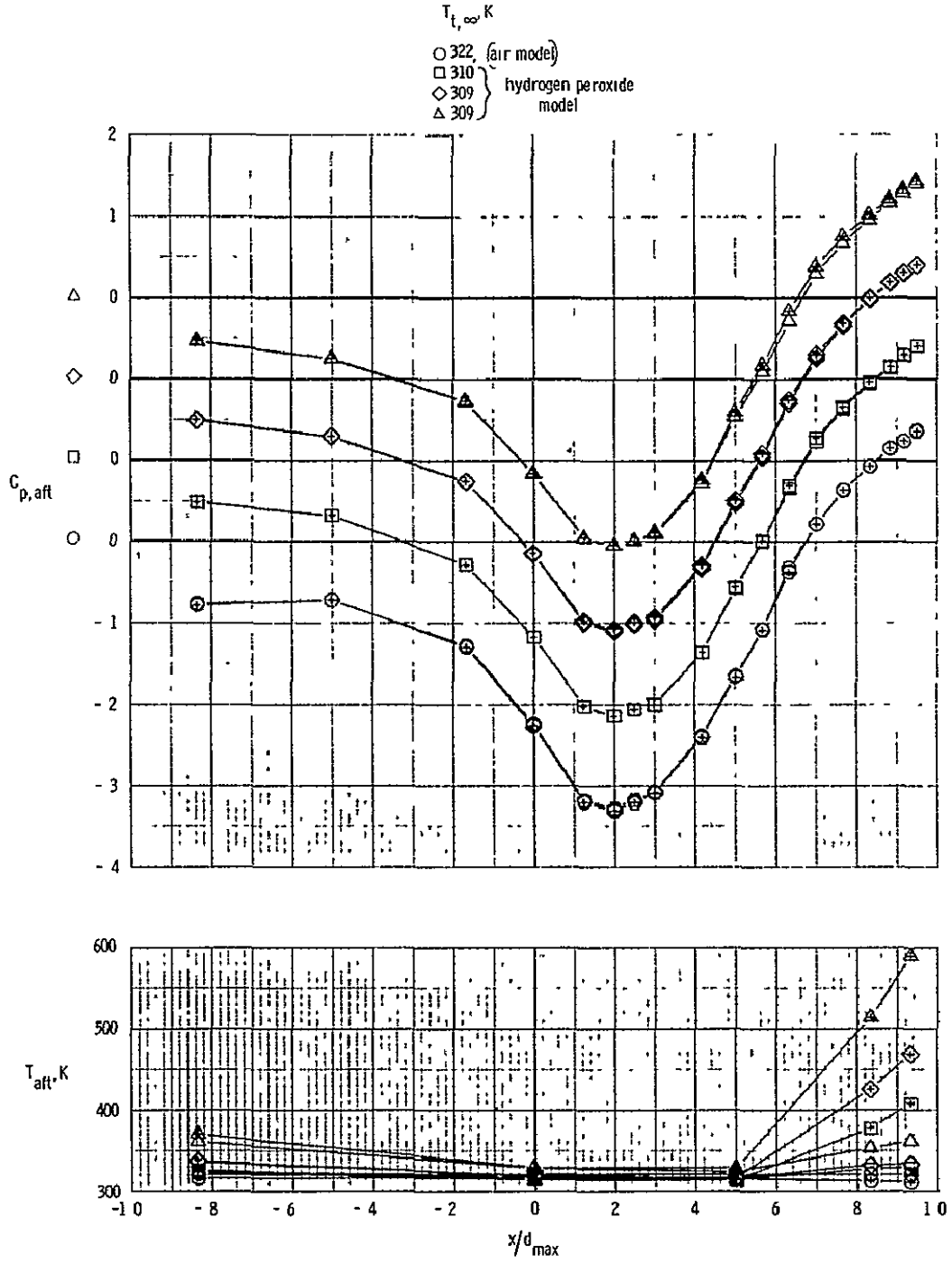

(a) Pressure coefficient and temperature distributions, $M_\infty = 0.60$.

Figure 30.- Jet off pressure coefficient and temperature distributions and boundary layer profiles for configuration 1. ($\beta = 20^\circ$; $\ell/d_{max} = 1.0$ Symbols with plus signs indicate data taken immediately after a jet pressure ratio sweep).

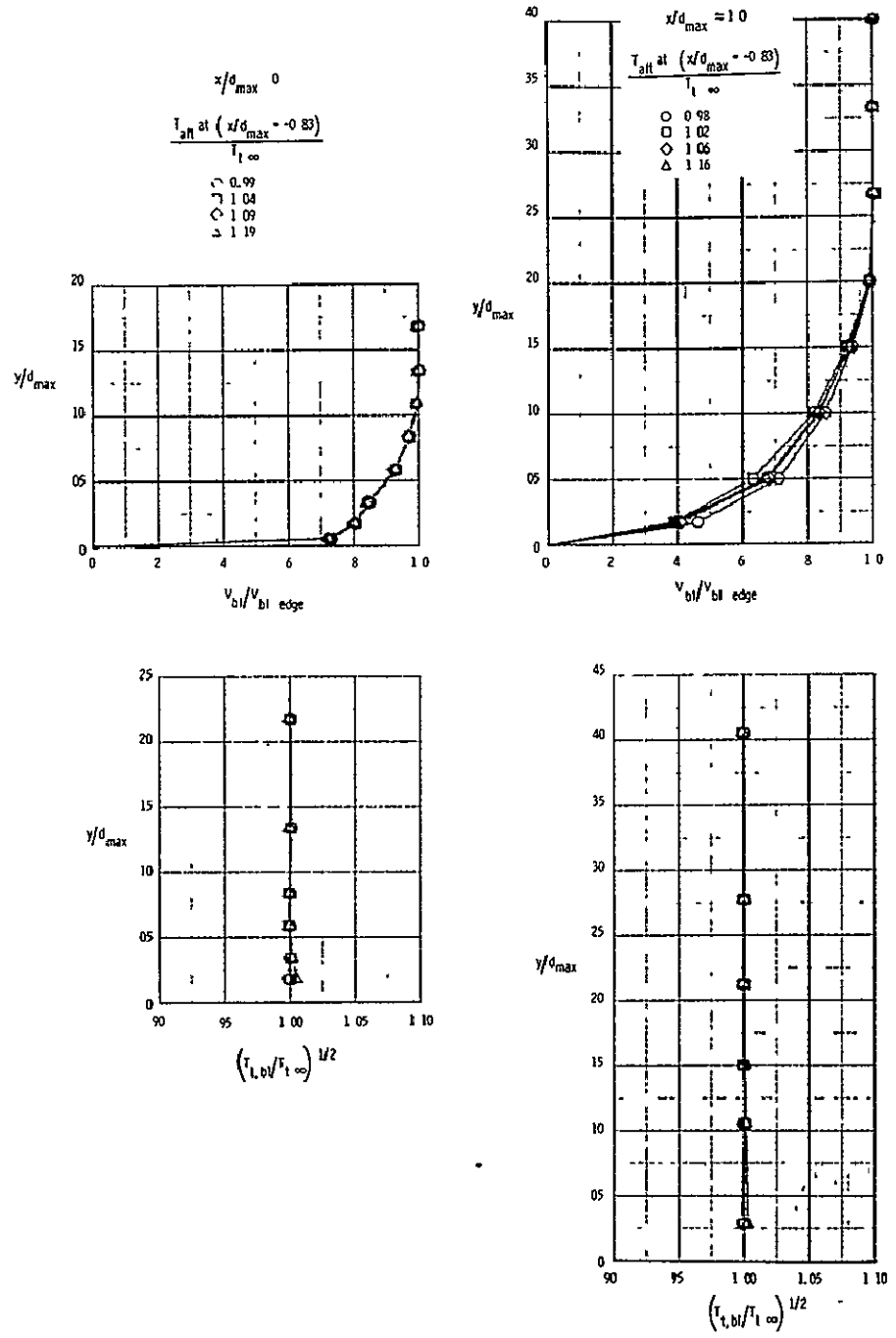

(b) Boundary layer profiles, $M_\infty = 0.60$.

Figure 30.-Continued.

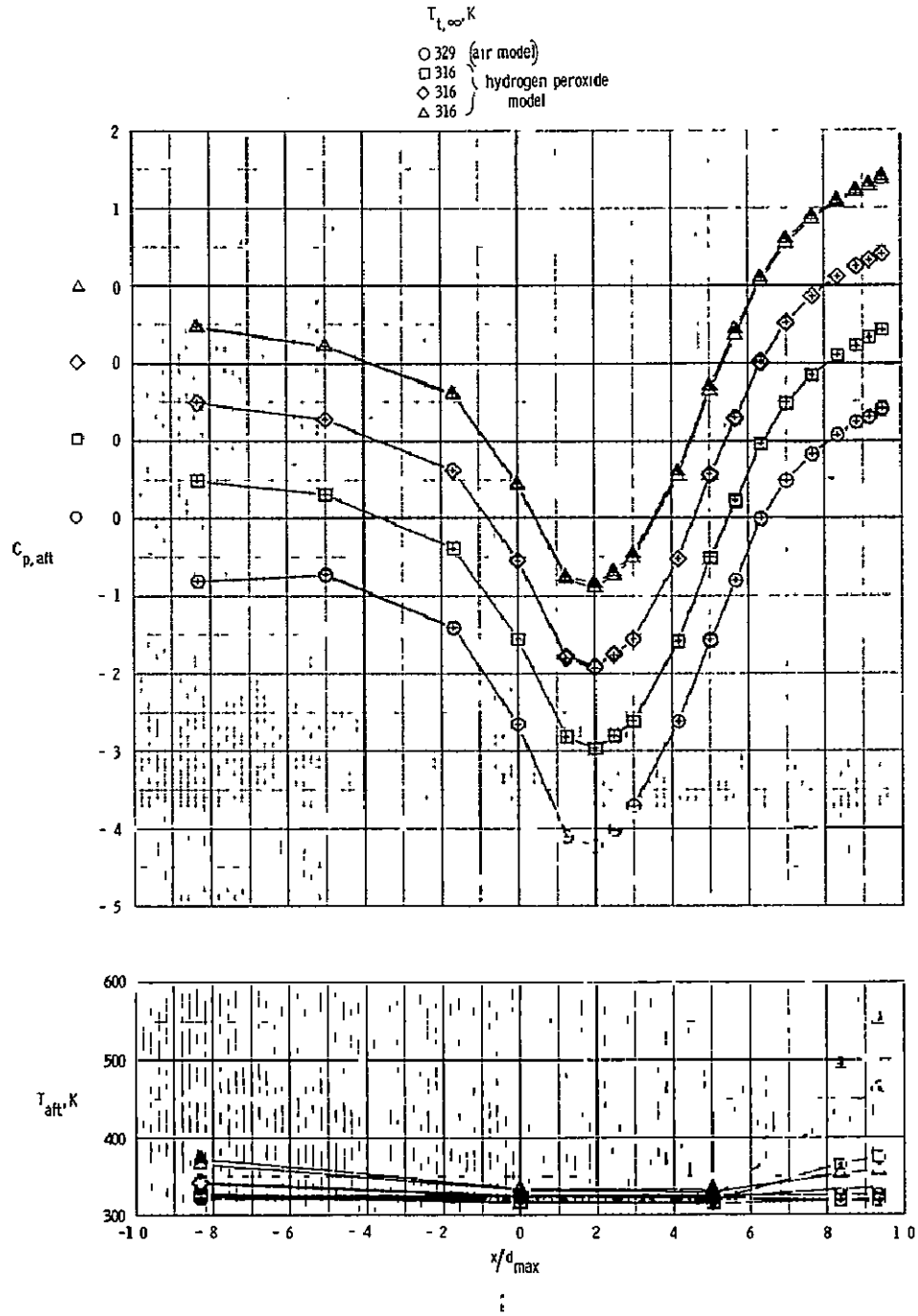

(c) Pressure coefficient and temperature distributions, $M_\infty = 0.80$.

Figure 30.—Continued.

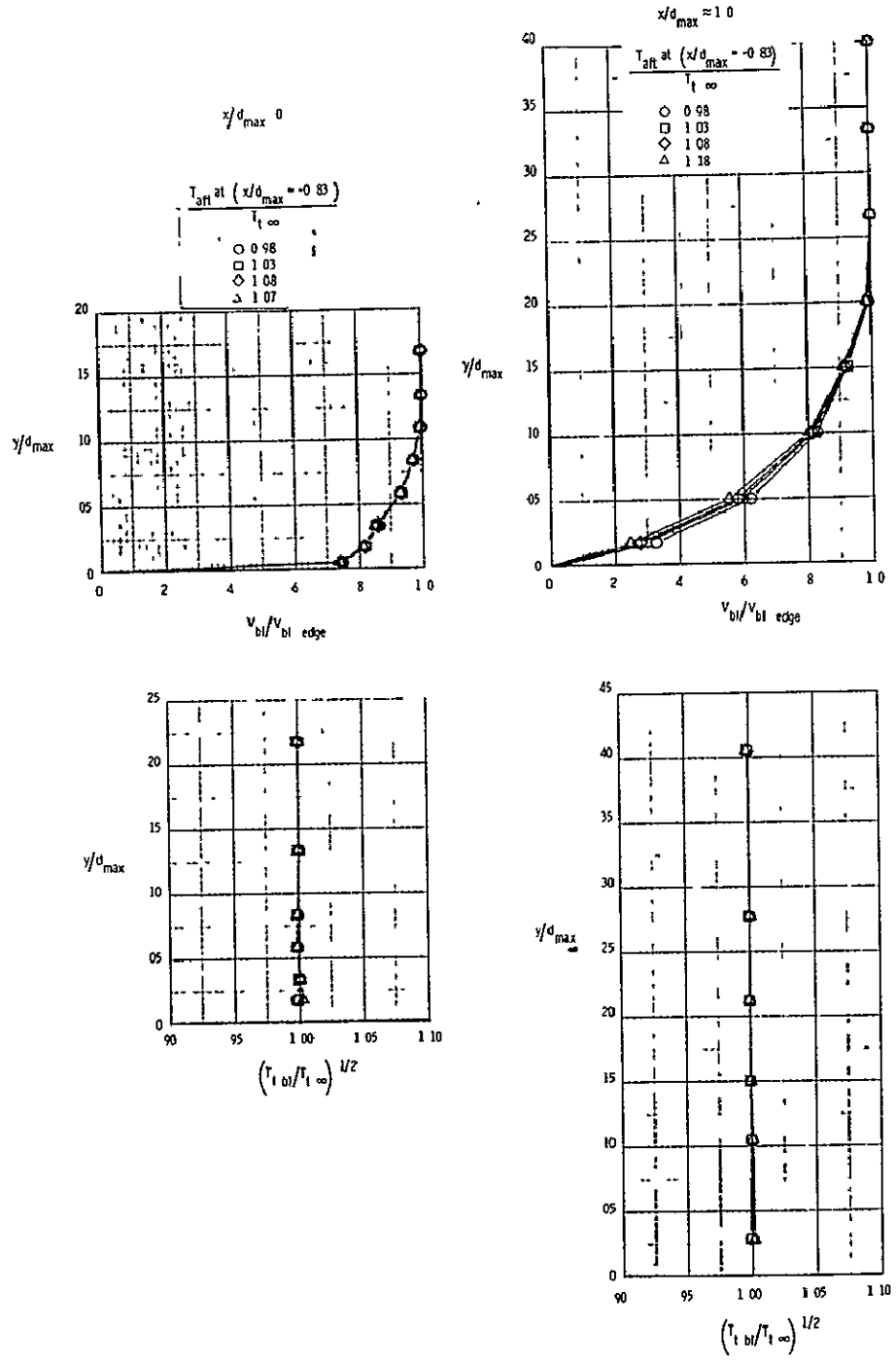

(d) Boundary layer profiles, $M_\infty = 0.80$.

Figure 30.- Continued.

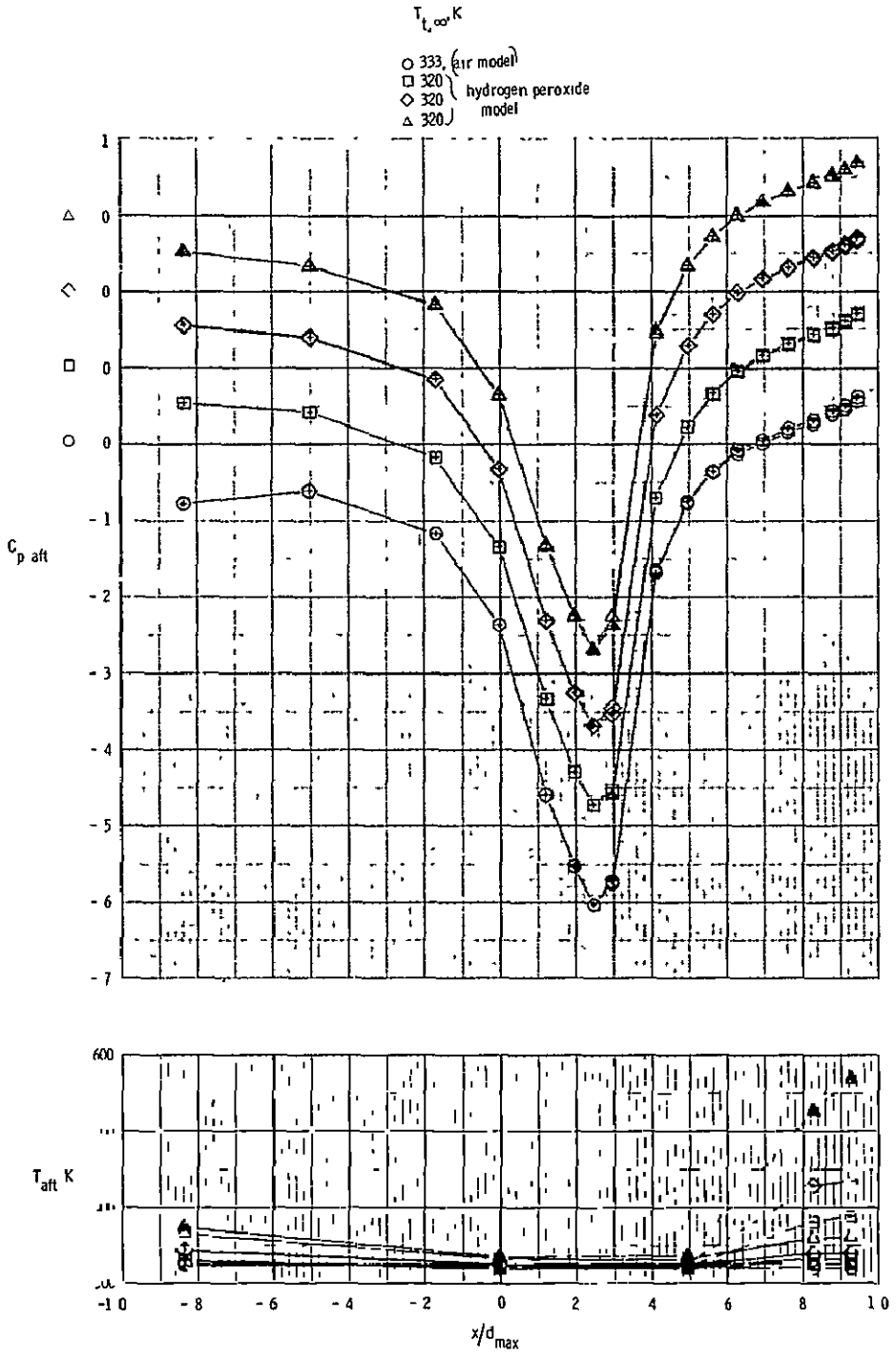

(e) Pressure coefficient and temperature distributions, $M_\infty = 0.90$.

Figure 30.- Continued.

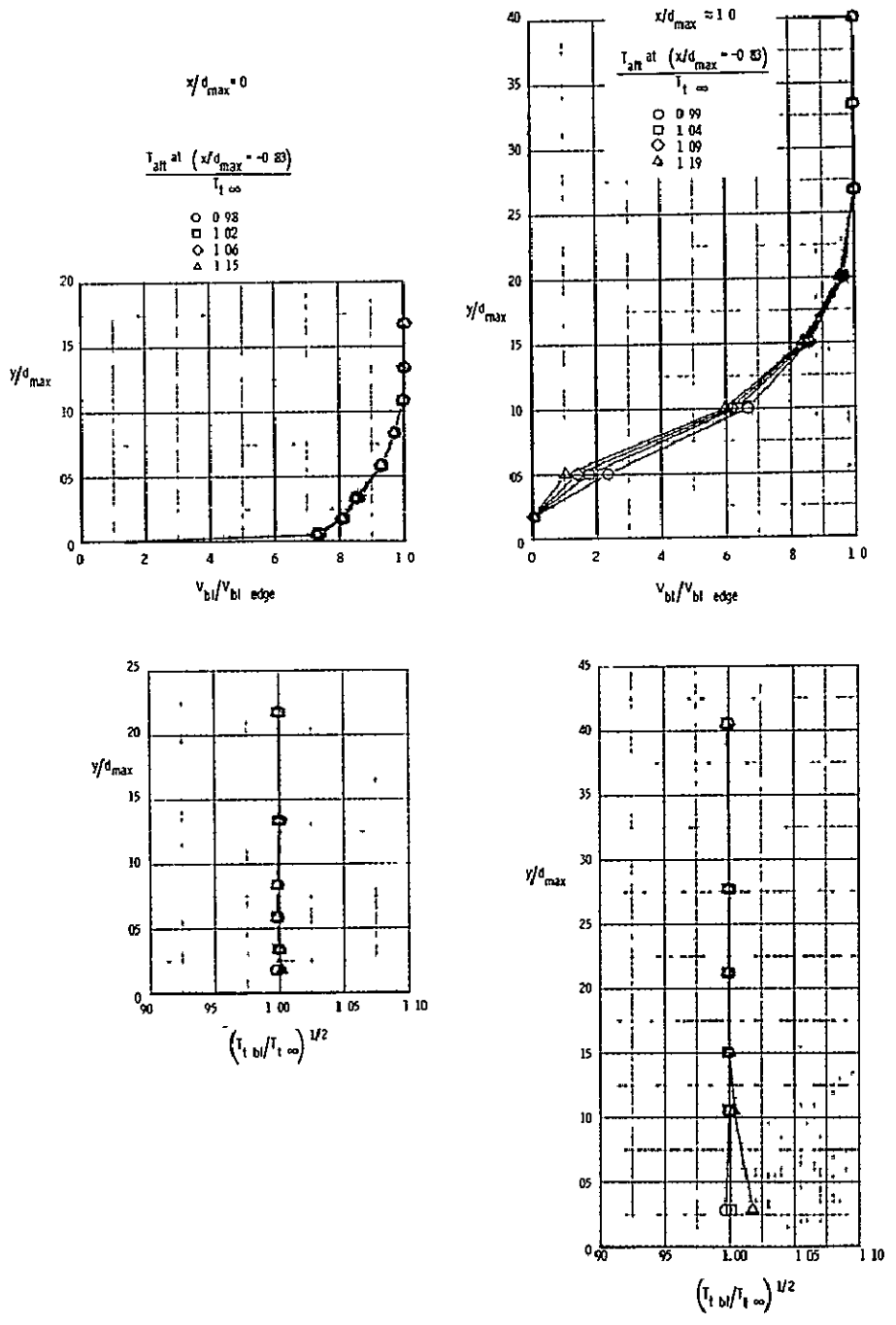

(f) Boundary layer profiles, $M_\infty = 0.90$.

Figure 30.- Continued.

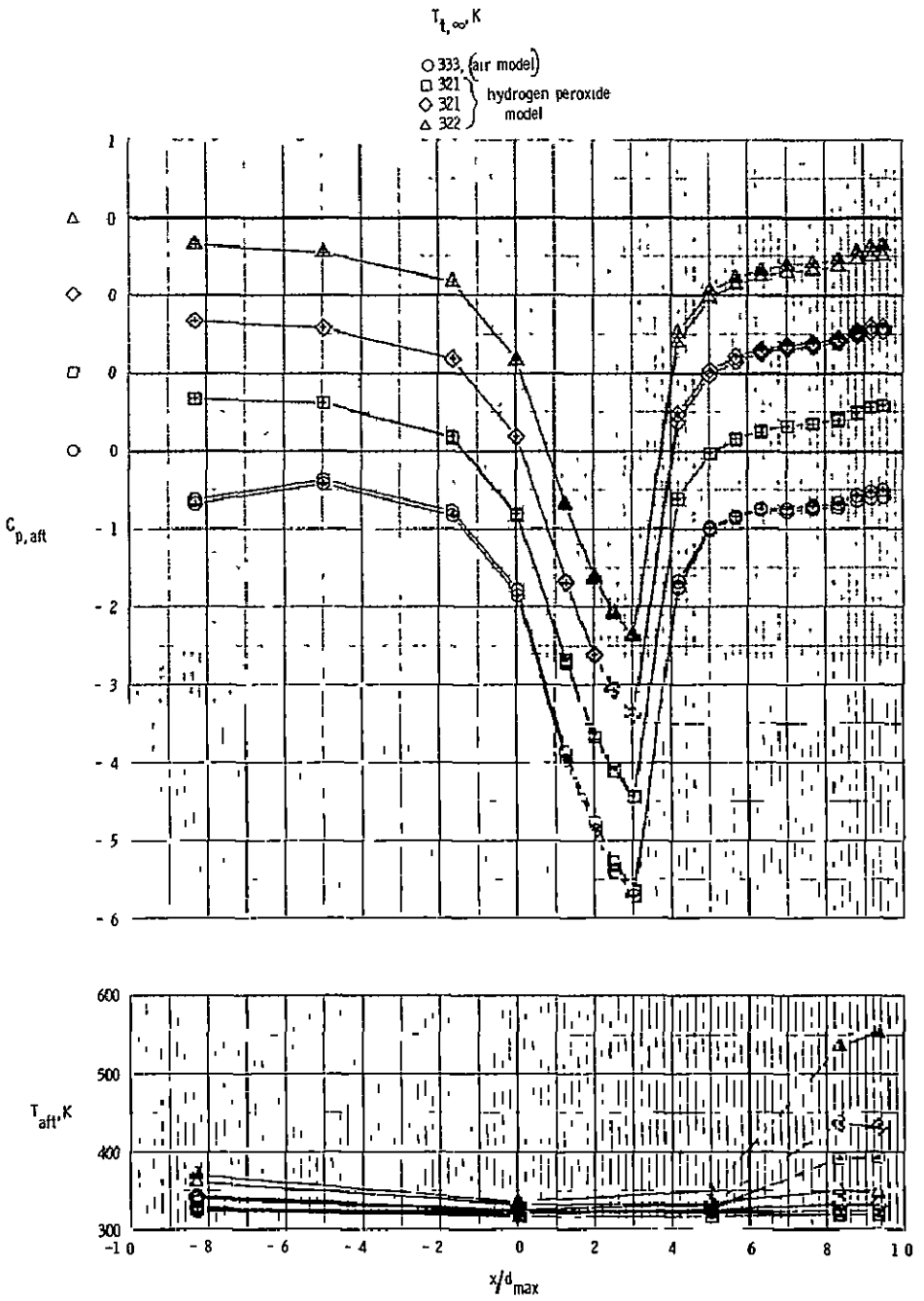

(g) Pressure coefficient and temperature distributions, $M_\infty = 0.95$.

Figure 30 .- Continued.

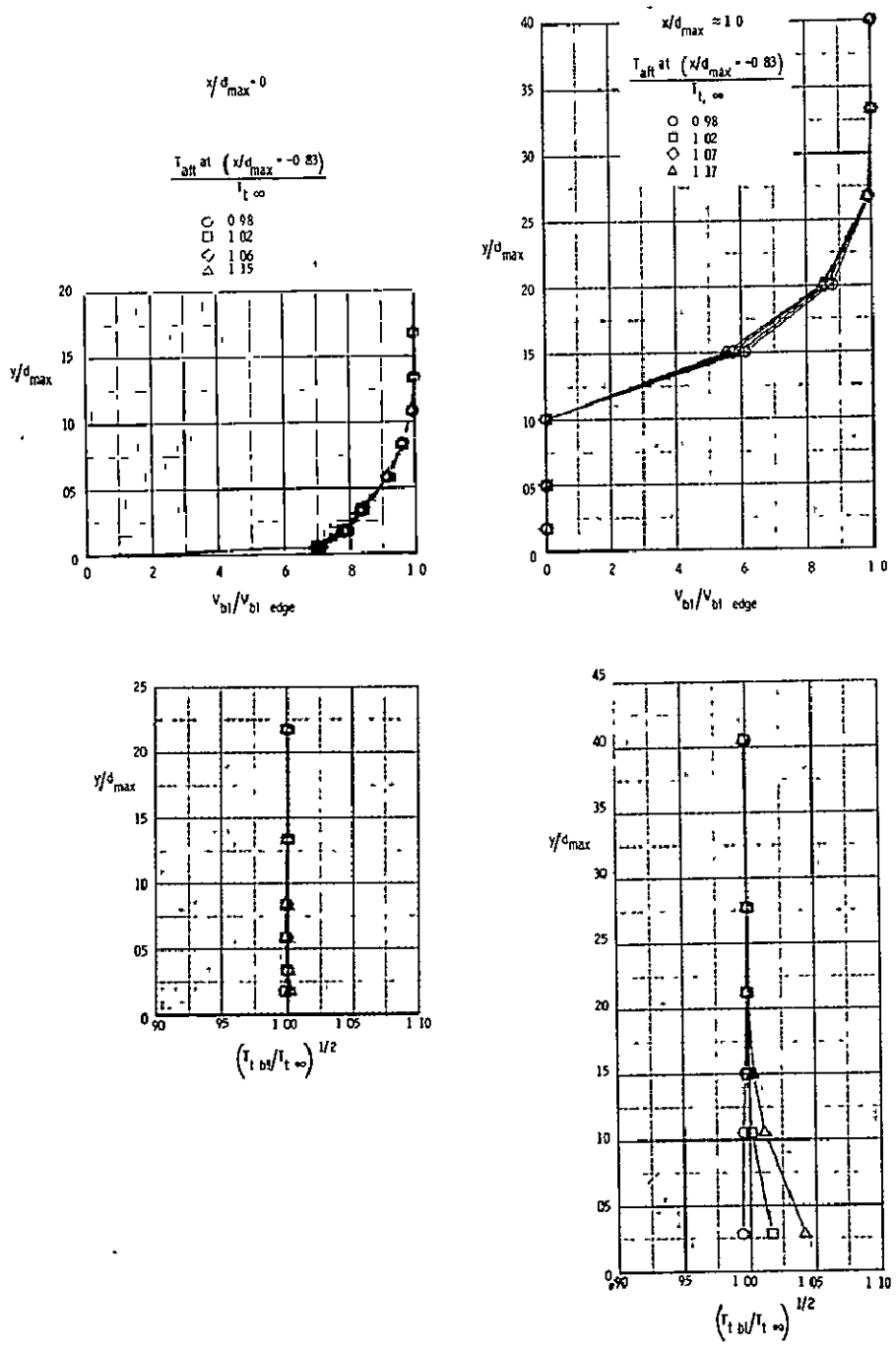

(h) Boundary layer profiles, M_∞ = 0.95.

Figure 30 .- Continued.

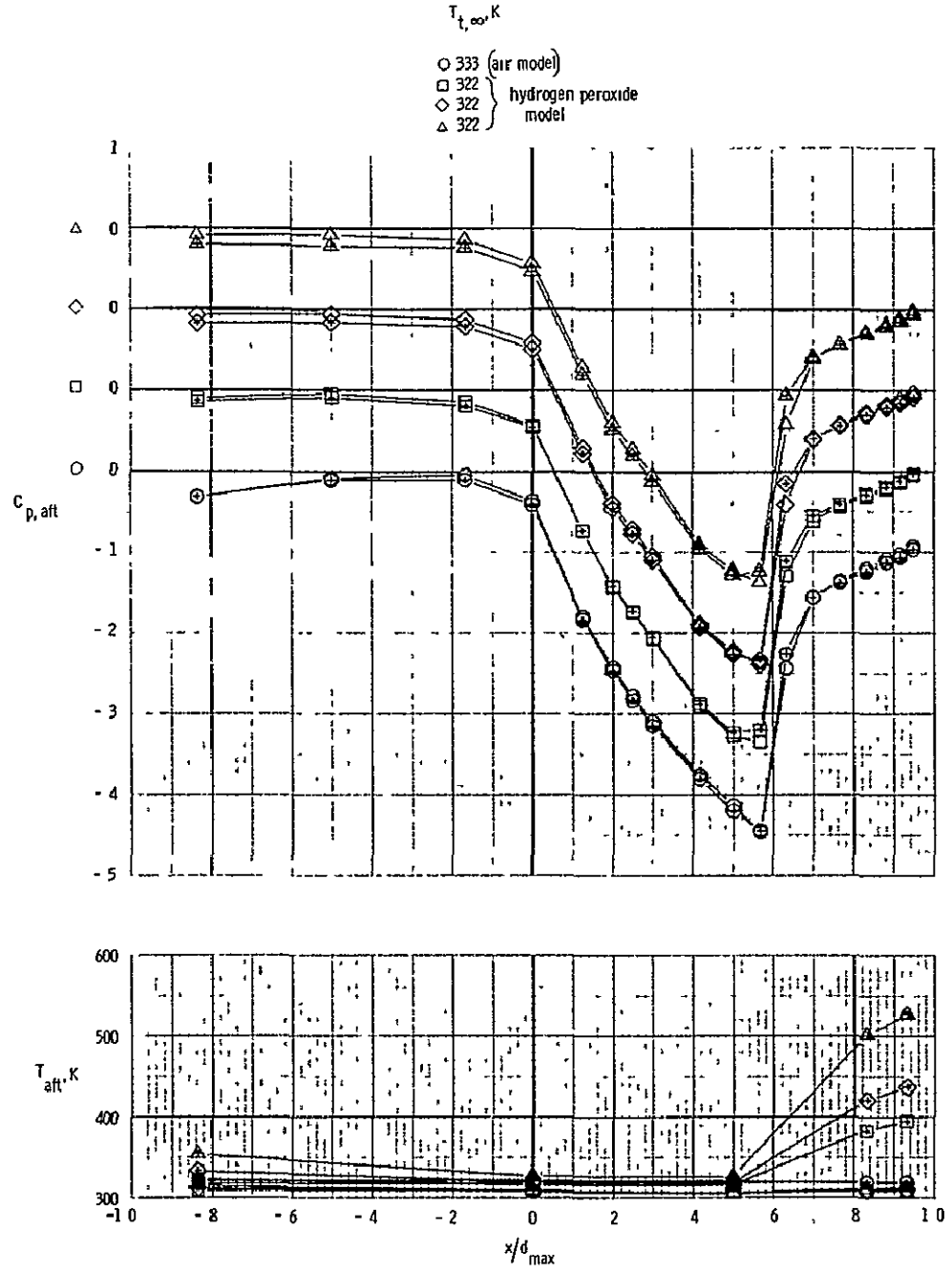

(i) Pressure coefficient and temperature distributions. $M_\infty = 1.20$.

Figure 30.- Continued.

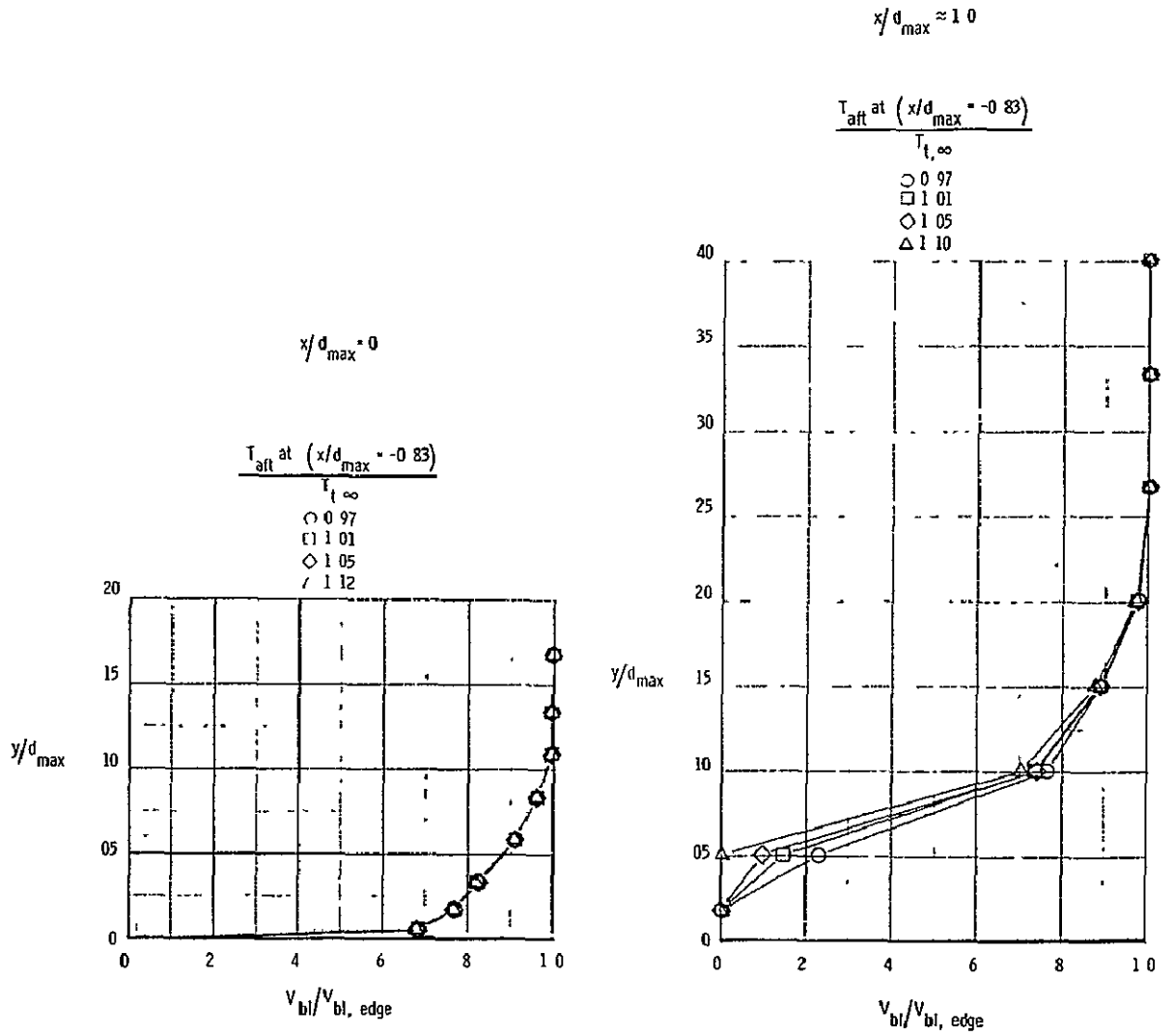

(j) Boundary layer profiles, $M_\infty = 1.20$.

Figure 30.- Concluded.

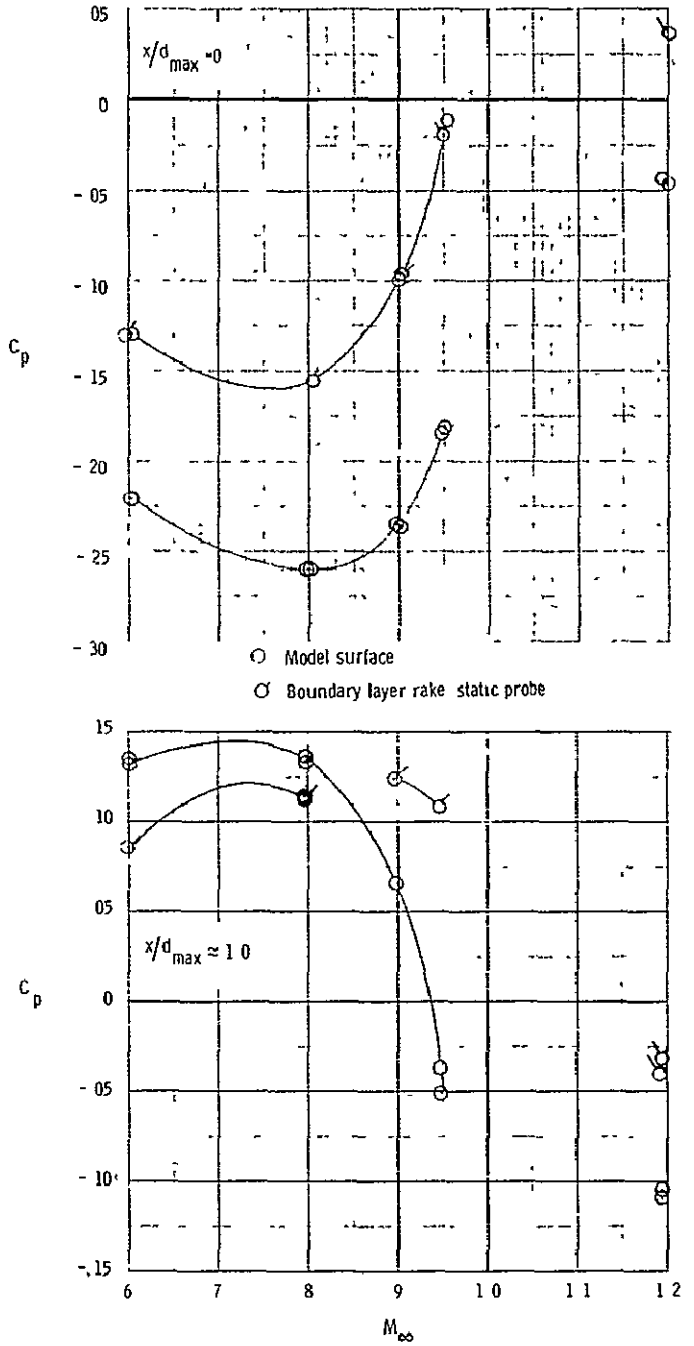

Figure 31.- Comparison of static pressure coefficients measured on the model surface with boundary layer rakes removed with those measured using the boundary layer rake static probes.

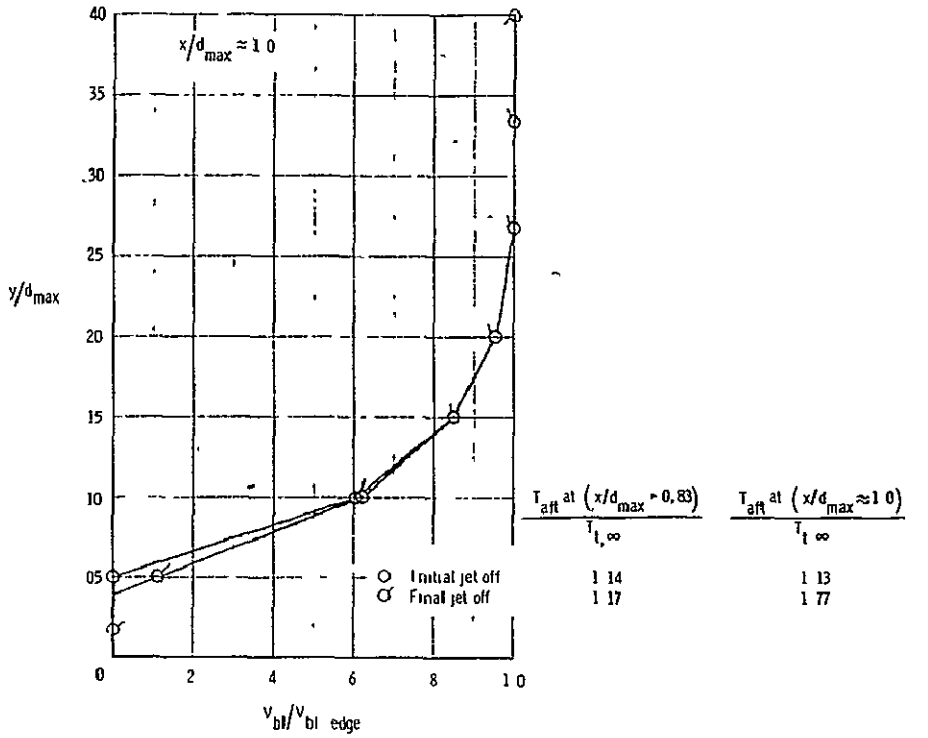

Figure 32.- Comparison of aft boundary layer profiles immediately before and after a jet pressure ratio sweep. (M_∞ = 0.90).

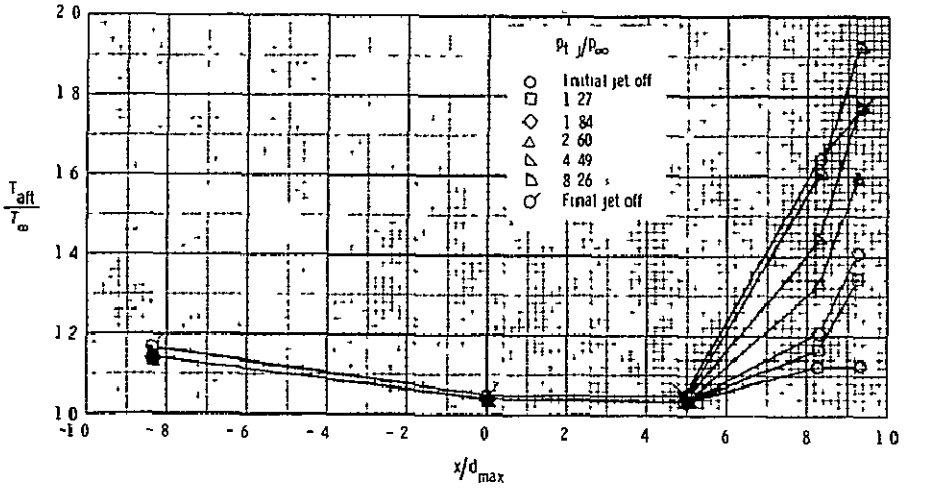

Figure 33.- Typical variation of afterbody skin temperatures during a jet pressure ratio sweep. ($\beta = 20^0$, ℓ/d_{max} = 1.0, $T_{t,j}$ = 1013K, M_∞ = 0.90).